Multifunctional colloidal-based nanoparticles for cancer treatment

Rita Falcão Baptista Ribeiro Mendes

Thesis to obtain the Master of Science Degree in

Bioengineering and Nanosystems

Supervisors: Doctor Marlene Susana Dionísio Lúcio

Doctor Susana Isabel Pinheiro Cardoso de Freitas

Examination Committee

Chairperson: Doctor Gabriel António Amaro Monteiro

Supervisor: Doctor Marlene Susana Dionísio Lúcio

Members of the Committee: Doctor Maria Elisabete Cunha Dias Real Oliveira

May 2017

Acknowledgments

First of all I would like to thank to the college institutions where I fortunately had the opportunity to learn, grow and enrich myself during all my academic life, Instituto Superior Técnico (IST) and Universidade do Minho (UM).

I would like to thank to Doctor Maria Elisabete Cunha Dias Real Oliveira the opportunity that gave me by accepting my request of working in the UM research team from the very first moment and all the concern and human support along the entire year. The present work would not be possible without all the availability, kindness and care that was always given to me during all the period of works.

Secondly, I have to write a special word to my supervisor Doctor Marlene Susana Dionísio Lúcio, which despite the amount of work within hands, always had a time to support me and teach me with the major patience and commitment. The contagious passion for the scientific world that was constantly present in every single explanation was one of the most crucial aspects for the success of this work and for making me grow as a scientist and as a human being. I would always have to thank all the incredible technical and human support that was given to me all the time.

I would also like to thank to Doctor Susana Isabel Pinheiro Cardoso de Freitas for the prompt availability on accepting to supervise my work and allowing this experience to be possible, as well as for technically supported me along the year. Besides, I want to give my thank you to my course Coordinators Doctor Luis Joaquim Pina da Fonseca and Doctor Gabriel António Amaro Monteiro, who allowed my year of studies at Universidade do Minho and gave me all the necessary support on what was needed.

All these years would not have been possible without the unconditional help and unforgettable moments lived with my friends, particularly Madalena Costa, Sofia Vaz, José Antunes and MEFT colleagues, Rita Santiago, Paula Libânio, Sofia Antunes, Sofia Alves, Ana Banha, Dulce Costa, Ana Andrade, Carolina Brum, Sara Galhoz, Rita Cardoso, Bárbara Rodrigues, Beatriz Portugal and all the other members of TFIST, José Cardoso and MBIONANO colleagues and finally to Vitor Marques and all my GASTagus' team. Most recent but also important, Telma Soares and Tiago Costa from UM. To all the non-referred friends that always helped me and supported me during my academic years, my very special thank you.

In this particular moment and year, a special thank you to my godmother Teresa Salgado and family Costa, to all the close and friendly support.

At last, but not the least, the major thank you to all my family for making me who I am every single day. To all my four grandparents for all the example of human being, respect and perseverance. To my brothers, for all the joint learning. And finally to my parents, that have always been there to share my achievements and support me in the most difficult times.

Resumo

O presente trabalho pretende desenvolver um sistema de libertação controlada de um dos fármacos mais utilizados no tratamento atual do cancro, a Doxorrubicina (DOX). O referido sistema consiste no uso de pontos quânticos de grafeno (GQD) como agentes fotossensíveis e transportadores da DOX que, consoante o pH a que estão expostos, adsorvem ou libertam o fármaco. Assim, os GQD permitirão a libertação controlada do fármaco pelo pH e a monitorização ótica do processo de libertação.

Foram sintetizados dois tipos de GQDs: por síntese química, pelo método de Hummer a partir de uma fonte de carbono (GQD-CB); e por uma via de nanofabricação de filmes finos, *Chemical Vapour Deposition* (GQD-CVD). O método de Hummer revelou-se simples mas conducente a uma população heterogénea de GQDs. Foi proposta uma separação dos GQD-CB por extrusão através de filtros de porosidade decrescente que demonstrou ser eficiente na diminuição gradual do tamanho dos GQDs, sem alteração da carga de superfície e das propriedades óticas. O método de obtenção de GQD-CVD poderá vir a ser mais promissor no controlo da constituição química dos GQDs e respetivos grupos funcionais, necessitando de grande otimização nesse sentido. De facto, por microscopia eletrónica e confocal Raman foi possível verificar uma grande distribuição de tamanhos e a existência de folhas de grafeno de alguns μm até partículas de tamanhos nanométricos. Um outro fator a otimizar será a forma de retirar os GQD-CVD do substrato de vidro onde são produzidos, tendo sido testado um método de ajuste de pH e sonicação que se revelou promissor.

Os GQD foram caracterizados quanto às suas propriedades químicas, óticas e elétricas por espectroscopia de fluorescência e de absorção UV-Vis; dispersão e eletroforese de luz dinâmica (DLS e ELS) para avaliação do diâmetro médio e do potencial zeta, permitindo inferir sobre a carga e a ionização dos grupos de superfície a diferentes valores de pH; microscopia confocal Raman e espetroscopia de infravermelhos (ATR-FTIR) para caracterização química. O mesmo tipo de caracterização foi aplicada à DOX e aos conjugados GQD-DOX, a vários valores de pH. Foram feitos estudos *in silico* para prever o valor do pH no qual a formação dos conjugados é favorecida (pH 4.5-8). A formação de conjugados ao valor de pH previsto foi confirmada pela observação de transferência de energia entre os GQD (dadores) e a DOX (aceitadora) e pela alteração espetral da absorção, onde ocorrem desvios hipsocrómicos e hipocrómicos indicadores de alterações intramoleculares estruturais.

Uma vez que os conjugados GQD-DOX são demasiado pequenos para poderem ser administrados sem ocorrer uma eliminação renal precoce, e tendo por objetivo futuro a encapsulação dos conjugados GQD-DOX em nanossistemas lipídicos, foi necessário perceber a incorporação dos GQD neste tipo de sistemas. Para tal foi estudada a incorporação dos GQD em lipossomas marcados com sondas fluorescentes capazes de reportar uma localização próxima dos grupos polares e uma localização mais profunda ao nível das cadeias acilo lipídicas. Em todos os casos foi possível detetar uma desativação de fluorescência das sondas indicativa de inserção dos GQD na membrana lipídica.

Palavras-chave: Pontos quânticos de grafeno (GQD), Doxorrubicina (DOX), Lipossomas, Nano libertação de fármacos, Tratamento de cancro

Abstract

Doxorubicin (DOX) is one of the most widely used anticancer drug nowadays. The main goal of this work is to develop a controlled release system that consists on the use of graphene quantum dots (GQDs) as photosensitive agents and DOX nanocarriers that adsorb or release the drug by pH-sensitivity. Therefore, GQD will allow the controlled release of DOX due to pH variations of external medium and also the monitorization of all the pathway process.

Two kinds of GQDs were produced: by chemical synthesis, using the Hummer's method with carbon black as the carbon source (GQD-CB); and by the thin film nanofabrication method Chemical Vapour Deposition (GQD-CVD). Hummer's method is a simple method but originates a wide heterogeneous population of GQDs. In response to that it was proposed a separation method of GQD-CB by extrusion through filters of decreasing porosities, which has shown to be efficient in the gradual decrease of GQDs size with no alteration of surface charge and optical properties. The CVD synthesis method is thought to be more promising due to higher control of the chemical composition of GQD-CVD and their functional groups, but needs to be optimized. In fact, SEM and confocal Raman analysis allowed to verify a wide distribution of sizes and the existence of graphene sheets from few µm to nanosized particles. Other important issue that needs to be optimized is the extraction of GQD-CVD from the glass substrate where they were transferred to during the synthesis process. A pH adjustment combined with sonication was tested and revealed to be a promising method to remove GQD-CVD from the substrate.

GQDs were optically, electrically and chemically characterized through fluorescence spectroscopy and UV-Vis absorption; dynamic and electrophoresis light scattering (DLS and ELS) to evaluate their average diameter and zeta potential, inferring the surface charge and ionization groups at different pH values; confocal Raman and infrared spectroscopy (ATR-FTIR) for chemical characterization. The same techniques were applied to DOX and GQD-DOX conjugates formed and evaluated at different pH values. *In silico* studies were made to theoretically predict the pH value where the conjugates formation is favoured (pH 4.5-8). That preference was confirmed by the observation of fluorescent energy transfer between GQD (donors) and the DOX (acceptor) and by changes on the absorption spectra of DOX, where hypsochromic and hypochromic shifts occurred and indicate intramolecular structural changes.

Since GQD-DOX conjugates are too small, they cannot be administrated without being rapidly eliminated by kidneys. Therefore, having the encapsulation of the GQD-DOX conjugates in lipid nanosystems as a future goal, it was necessary to understand the incorporation of GQD onto these kind of systems. To do that, it was studied the incorporation of GQD into liposomes labelled with two fluorescent probes which were capable of reporting a localization near to the polar head groups and other deeper localization at the acyl lipid chains level. In both cases it was possible to detect a quenching on the probes fluorescence, indicative of the insertion of the GQD into the lipid membrane.

Key Words: Graphene quantum dots (GQD), Doxorubicin (DOX), Liposomes, Nano drug delivery, Cancer treatment

List of contents

Index of Figures

Index of Tables

Acronyms

12AS	12-anthroyloxystearic acid
3AS	3-anthroyloxystearic acid
AFM	Atomic force microscopy
ATR-FTIR	Attenuated Total Reflectance – Fourier Transform Infrared Spectroscopy
BSE	Backscattered electrons
CDs	Carbon dots
CEE	Cross-link-enhanced emission
CNDs	Carbon nanodots
CNPs	Carbon nanoparticles
CNTs	Carbon nanotubes
CQDs	Carbon quantum dots
CTRs	Cathode ray tubes
CVD	Chemical Vapour Deposition
DLS	Dynamic light scattering
DMPC	Dimyristoylphosphatidylcholine
DOX	Doxorubicin hydrochloride
DPPC	Dipalmitoylphosphatidylcholine
ELS	Electrophoretic light scattering
FL	Fluorescence
GO	Graphene oxide
GQD	Graphene quantum dots
GQD-CB	Graphene quantum dots synthetized from carbon black
GQD-CB-DOX	Conjugates of graphene quantum dots from carbon black and doxorubicin
GQD-CBext	Extruded graphene quantum dots from carbon black
GQD-CVD	Graphene quantum dots synthetized by chemical vapour deposition
H_2SO_4	Sulfuric acid
HNO_3	Nitric acid
HOMO	Highest occupied molecular orbital
IR	Infrared light
LPCVD	Low pressure chemical vapour deposition
LUMO	Lowest unoccupied molecular orbital
LUVs	Large unilamellar vesicles
MLVs	Multilamellar vesicles
NaH_2SO_4	Sodium dihydrogen sulphate
NLC	Nanostructured lipid carrier
PAHs	Polycyclic aromatic hydrocarbons
PBS	Phosphate buffered saline

PC	Phosphatidylcholines
PCS	Photon Correlation Spectroscopy
PDMS	Polydimethylsiloxane
PDs	Polymeric dots
PEG	Polyethylene glycol
PL	Photoluminescence
PMMA	Polymethylmethacrylate
QCE	Quantum confinement effect
QY	Quantum yield
rGO	Reduced graphene oxide
RIE	Reactive ion etching
ROS	Reactive oxygen species
SE	Secondary electrons
SEM	Scanning Electron Microscopy
SUVs	Small unilamellar vesicles
TBAP	Tetrabutylammoniumperclorate
TEM	Transmission electron microscopy
UHVCVD	Ultra-high vacuum chemical vapour deposition
UV-Vis	Ultraviolet-visible light
VIS	Visible light
VIS-NIR	Visible-near infrared light

1 Introduction

1.1 Motivation and aims

Cancer is one of the most lethal pathology and nowadays chemotherapy has high levels of cytotoxicity and relatively low therapeutic efficiency [1]. Therefore, it becomes urgent to create new methods with higher efficient results and less secondary effects. Our main goal is to create multi-strategic nanostructured lipid carriers (NLC) that can simultaneously act as drug delivery systems and allow the pathway monitorization until reaching the target cells in a controlled way [2].

NLC are supposed to be totally biocompatible and not detectable by the immune system, and should release the drug in response to specific stimuli. We aim to develop multi conceptual NLC that hold these features together: therapy, by drug delivery; imaging, by the optical properties of nanocarriers (in our case graphene quantum dots (GQDs)); triggering, by using pH-sensitive GQDs-drug conjugates; targeting, with passive or active strategies; and stealth strategy through polymeric coverage of NLC. [2]

In sum, the ultimate goal is to achieve a hybrid nanosystem with several innovative features in the context of cancer treatment: (i) the encapsulation of anti-cancer drugs in nanocarriers that protect the healthy tissues from the anticancer drug cytotoxicity, (ii) NLC specific targeting so that they will have more specificity for cancer cells than for healthy tissues, (iii) stealth strategies to avoid recognition and opsonisation of the nanocarriers by the immune system, increasing the nanotherapeutic half-time, and finally (iv) triggering features that promote the controlled release of the drug from the nanocarriers into the cancer cells. [2]

Based on the motivation presented by the challenging cancer disease, and on the steps required to reach the envisioned hybrid nanosystem, the present work constitutes an important step in the broader picture of the formulation pursued. Since the most widely anticancer drug used is doxorubicin (DOX) [1] [3], we propose the use of GQDs with the following features: immobilization of DOX on their surface, associated to a fluorescence quenching effect; act as DOX carriers until the target cancer cells; release the DOX at cancer cells due to pH changes; and the re-establishment of GQDs initial fluorescence after DOX release, allowing the monitorization and optical control of drug delivery. To achieve these purpose several specific aims have been established for the current work [2]:

- Development, optimization and comparison of two different methods to produce GQD
- Chemical, optical and surface charge characterization of the GQD produced, by different techniques and at different pH values
- Characterization of DOX by different techniques and at different pH values
- Theoretical modelling of the drug and GQD probable major microspecies at relevant pH values
- Electrostatic binding of GQD and DOX and characterization of the resultant GQD-DOX conjugates
- Evaluation of the incorporation of GQD in lipid nanosystems.

1.2 Carbon dots

Carbon (C) is a chemical element that can form many different structures in the same physical state. These structures are known as carbon allotropes and the most studied ones since our ancient times were graphite and diamond, which are three-dimensional carbon forms. Recently, one-dimension and zero-dimension forms of carbon were discovered and studied, being them the carbon nanotubes (CNTs) and the fullerenes, respectively. Although it was not experimentally obtained until 2004, the two-dimensional form of carbon, graphene, was already well-studied and has supported all theoretical studies concerning carbon forms. When graphene was finally obtained, it caused a revolution in the scientific world, since it had promising properties and proved that it is possible to obtain stable two-dimensional crystals at environmental conditions. [4] [5] [6]

Graphene consists on a planar monolayer of carbon atoms in hexagonal honeycomb lattice and is derived from graphite that is more than one layer of graphene stacked on the top of each other. Graphene is a gapless semiconductor with unique optical, electronic and mechanical properties, which can be tunable depending on its synthetic strategy [4] [7] [5]. Pure graphene is considered to be the thinnest and lightest known material, with one atom thick and a weight of about 0.77 mg per square meter. It is also the strongest compound (≈ 100-300 times stronger then steel, with a tensile stiffness of $1.5x10^8$ psi) and the best conductor of heat at room temperature (≈ $4.84 \pm 0.44 \times 10^3$ to $5.30 \pm 0.48 \times 10^3$ $Wm^{-1}K^{-1}$) and electricity with an electric mobility of more than 1.5×10^4 $cm^2V^{-1}s^{-1}$ (≈100 times more conductor then copper). It also absorbs 2.3% of white light and these features all together give graphene a huge scientific relevance. [8]

The ability of generating all its allotropes is given by the carbon chemical characteristics. Carbon is a tetravalent element from the fourteenth group of the periodic table with an atomic number 6. It has four electrons on its valence level and thus need to stablish four covalent bonds to achieve chemical stability. When carbon atoms bind covalently to other atoms, they hybridize their valence orbitals s and p and create new hybrid orbitals (sp3, sp2 and sp). Depending on the kind of hybridization they suffer, they will be able to stablish simple, double or triple bonds, through a different number of π and σ bonds. Carbon atoms may bind to other carbon atoms or to other elements such as hydrogen (H), oxygen (O), nitrogen (N), sulphur (S) or halogens. [8] [6]

Since carbon is the second most abundant element within human body and the fourth most abundant element in the universe (by mass) it is the chemical basis of all known life on earth and became an eco-friendly, low toxic and biocompatible, low cost and sustainable source for new biotechnology approaches [8] [7]. Many carbon-based fluorescent materials like carbon nanodots (CNDs), carbon nanotubes (CNTs), graphene oxide (GO), graphene quantum dots (GQDs), polymer dots (PDs) and nanodiamonds have been created and all of them have sp2/sp3 hybridized carbon structures, oxygen- and nitrogen-based groups and post modified chemical groups [9] [10] [11] [6]. These features confer them the unique and necessary optical properties to achieve a wide variety of applications such as the generation of

semiconductor nanomaterials, transparent electrodes, high performance compounds, effective treatment of cancer through hydrophobic drug delivery systems, among others [12] [10] [13] [5].

Within the carbon-based materials we will focus on the carbon colloidal-based nanoparticles, the carbon dots (CDs). Carbon dots is a designation for a variety of carbon-based nanoscale materials, which can be divided into three main categories, GQDs, CNDs and PDs. Although they are different from each other in their intrinsic compositions and superficial chemical groups, CDs have quite similar photoluminescent (PL) properties [5]. [14]

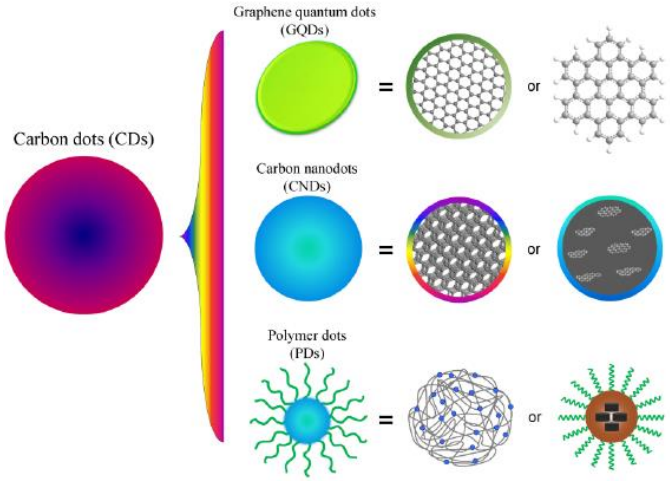

Figure 1 - Carbon dots' subdivision into Graphene quantum dots (GQDs), Carbon nanodots (CNDs) and Polymer dots (PDs.) [14]

GQDs have a carbon core with some crystallinity with an average lattice parameter of 0.142 nm that corresponds to the distance (100) between two atoms on the sp2 bonded plane of graphene. They are anisotropic with lateral dimensions superior to their height. GQDs have one or a few layers of graphene and are connected to superficial chemical groups on the edges. They can be derived from pure graphene, graphene oxide (GO) or even reduced graphene oxide (rGO) [9]. [8] [11]

CNDs are always spherical-shaped and can be divided into carbon nanoparticles (CNPs) and carbon quantum dots (CQDs). The first do not have a crystalline lattice whereas the latter have. The spacing (002) between crystalline layers on CQDs is 0.335 nm, corresponding to the value of crystalline graphite. [14]

PDs are aggregated or cross-linked polymers that have a carbon core self-assembled with the polymer chains and are obtained from linear non-conjugated polymers or monomers. [14]

All the CDs have attached or modified chemical groups on their surfaces like oxygen- or amino-based groups or polymer chains. Since they are not pure carbon, their photoluminescence is directly related to the hybridization and coefficient between the carbon core and the surrounding chemical groups. [15] [14] [5]

1.2.1 Methods of preparation

Carbon dots may be obtained through a wide range of methods and from a variety of carbon sources [9] [14] [16]. Herein it is presented a brief summary of the main chemical routes and carbon sources used as well as some examples of the resultant types of dots produced and their optical properties (Table 1). The chemical vapour deposition (CVD) method will also be described as it is nowadays considered to be one of the most efficient methods to achieve almost pure graphene sheets and there are some attempts to achieve graphene quantum dots through it [8] [17].

Table 1 - Synthesis of top-down, bottom-up and CVD methods of carbon dots production.

Methods	Subclassification	Source	Size (nm)	Height (nm)	Color	QY (%)	Ref.
Top-down	Amino-hydrothermal	GO	2.5	1.13	Blue to Yellow	-	[18]
	Microwave	GO	2-7	0.5-2	Green, Blue	8	[19]
	Microwave-hydrothermal	GO	3	<0.7	Blue	-	[20]
	Hydrothermal	Carbon Black	3-4.5	-	Blue	4.13	[21]
		rGO	2-5	-	Blue	-	[22]
	Solvothermal	GO	5.3	1.2	Green	1.6	[23]
	Acidic oxidation	Carbon Black	15	0.5	Green	44.5	[24]
	Ultrasonic chemistry	Graphene	3-5		Blue	-	[25]
	Electrochemistry	Graphite rods	5-10	<0.5	Yellow	-	[26]
	Physical reduction	Carbon Black	1.68-2.39	-	Blue	19.01	[27]
	Photo-Fenton Reaction	GO	40	1.2	Blue	45	[28]
Bottom-up	Catalysed cage-opening	C60	2.7-10	-	-	15-30	[29]
	Stepwise solution chemistry	Organic precursors	2.5-5	-	Red	-	[30]
	Precursor Pyrolysis	Citric acid	15	0.5-2	Blue	-	[31]
	Pyrolysis and exfoliation	Unsubstituted HBC	60	2-3	Blue	-	[32]
CVD	monolayer graphene grown on 25 mm thick copper foils	H2, CH4	<8nm	-	Blue	-	[17]
	monolayer graphene grown on 25 mm thick copper foils	H2, CH4 (low concentration)	300-400	-	-	-	[33]
		H2, CH4 (high concentration)	20-80	-	-	-	

1.2.1.1 Chemical synthesis

Top-down

The top-down approaches used to obtain CDs include the nano-cutting of carbon sources like rGO, GO, CNTs, fullerenes, graphite electrodes and graphite powder or flakes, graphene, carbon rods and carbon black, among others (Figure 2) [9]. The methods go from acidic oxidation [9] processes to other nano-cutting strategies as electrochemistry [26], hydrothermal/solvothermal/special oxidation [22] [23] or even other strong physical [16] or chemical routes [34]. Among the physical ones, arc discharge [35], laser

ablation [36] or nanolithography by reactive ion etching (RIE) [37] are the most used and within the chemical ones we should also mention the microwave- and sonication-assisted methods. [5]

Acidic oxidation may be handled in a one- or two-step method. In the one-step method, the bulk carbon materials are cut into small pieces under the action of concentrated oxidizing acids (HNO_3, H_2SO_4 or a mix of both), becoming their surfaces modified by oxygen-based groups. The small pieces are already CNDs, CQDs or GQDs. To achieve GQDs concretely, the two-step method is required. In this case, a first step is used to convert graphite-based materials into GO sheets using the Hummer's method or a modification of it [24] and the second step is the nano-cutting of GO sheets into GQDs. Acidic oxidation methods are the most widely used do produce CDs. [24] [5]

Electrochemistry approaches consist on the assisted electrochemical exfoliation of carbon-based electrodes. Carbon electrodes are broken up by electrochemical cutting and originate CQDs or GQDs. The applied electric field pulls the carbon particles from electrodes through graphite layer intercalation and radical reaction. The electrolytes that mediate this processes contain solutions of ethanol, ionic liquid, NaH_2PO_4, tetrabutylammoniumperclorate (TBAP) or other solvents as phosphate buffered saline (PBS)/water. [26] [14]

On the hydrothermal/solvothermal oxidations defect-based carbon materials as GO and CNTs are cut under high temperature and pressure due to the action of strong alkaline medium [21] [22] [23]. Some special Photo-Fenton reactions may also break up GO to form GQDs [28].

Finally, in physical methods, RIE is considered to be one of the most efficient to control CDs size and chemical surface, being also favourable to study some photoluminescent mechanisms. [14] [37]

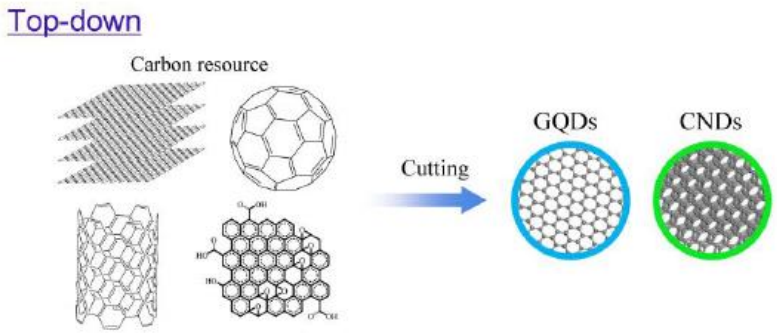

Figure 2 - Top-down mechanism of producing carbon dots. [14]

Bottom-up

Bottom-up methods are based on dehydration and carbonization of carbohydrates and organic synthesis of CNDs and PDs from small molecules and polymers. The mentioned sources have chemical groups like –OH, -COOH, -C=O and $-NH_2$ that can dehydrate at high temperatures. [21] [32] [30]

Dehydration and carbonization processes may occur by pyrolysis in concentrated acid, carbonization in a microreactor, by catalysed cage-opening or solution chemistry methods. These processes are difficult

to control and the generated CDs have polydispersity. To overcome this problem and achieve accurately GQDs with the desired size and weight, intramolecular oxidative polycyclic aromatic hydrocarbons (PAHs) are widely used on bottom-up techniques. [31] [32] [30] [29]

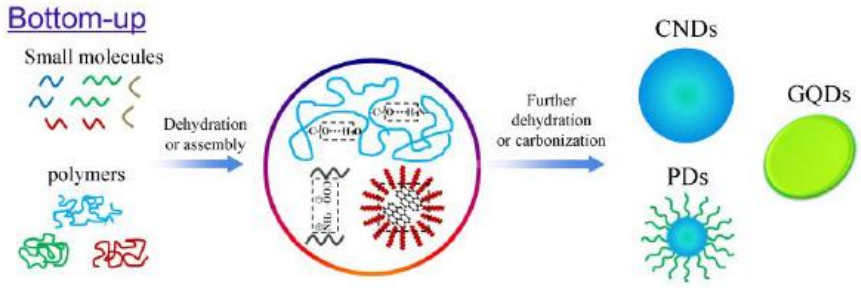

Figure 3 - Bottom-up mechanism of producing carbon dots. [14]

1.2.1.2 Chemical Vapour Deposition (CVD)

CVD is a nanotechnological process that enables the production of thin films of a desired material onto a chosen substrate. It allows the low cost large scale production of high quality materials, being them impervious and fine grained with high purity and increased hardness over other coating methods. The main disadvantages are the great toxicity of the by-product of the chemical reactions and the fine choice of precursors that have to be enough volatile to react with the substrate but not too much that turn it difficult to put them into the reaction chamber. [8]

Gaseous sources and volatile precursors which act as their carriers are injected into a reaction chamber where the chemical reactions occur allowing the deposition of a single atomic layer on the substrate. After the deposition and diffusion of the desired material on the substrate, the by-products dissociate from it and are pumped out of the chamber. The pressure within the reaction chamber is controlled by the gaseous flow and is a determinant factor on CVD operating modes. Low pressure CVD (LPCVD) prevent unwanted reactions and produce more uniform thickness layers and occur at sub-atmospheric pressures, whereas ultra-high vacuum CVD (UHVCVD) acts at extremely low atmospheric pressures of about 10^{-6} Pa. The substrate temperature and the temperature of the reaction chamber are also crucial parameters that define the fate of the wanted thin film material, as well as the gas composition and volume and the time duration of the process. The chemical reactions take place at the substrate surface and the energy is given thermally, by photons or by glow discharges. The reaction time rate can be controlled by the addition of catalysts or adjusting the mentioned parameters. [38] [8]

Graphene sheets production by CVD occur mainly in two steps. A first step where a precursor suffers pyrolysis to obtain dissociated carbon atoms. This stage has to happen upon the substrate surface to avoid carbon clusters precipitation during the gaseous phase and require high temperatures levels. The second step is the formation of graphene structures using the dissociated carbon atoms that also requires high temperatures. [8] [39]

There are some problems yet to solve on the production of graphene monolayers. [17] The dissociation or exfoliation of graphene from the substrate is a hard task to handle without damaging graphene structure. To overcome this problem, a new strategy uses a copper (Cu) substrate that also acts as catalyst. Cu has very low carbon solubility and acts like self-limiting substrate for graphene growth. Usually, an oxide copper layer is put in between Cu and graphene since it promotes weaker mechanical and electrostatic interactions between these layers, allowing an easier way to remove graphene. The graphene transfer process is currently done with intermediate polymers like polymethylmethacrylate (PMMA) [33] or polydimethylsiloxane (PDMS) [40], being PMMA the most efficient and the one that cause less damages to graphene. PMMA acts as a temporary transfer substrate in between the etching of the first one and the deposition on the final one. [8] [33] [11]

Another problem is the incapacity to generate a completely uniform layer of graphene on the substrate due to the dynamic kinetics of gases that occur by convection and diffusion and are always changing inside the reaction chamber. *Hassanien* [11] took advantage of the impurities and imperfections of graphene monolayers production by CVD and obtained GQDs from it by sonication processes and suspension and dilution of them in organic solvents. They also studied their optical and intrinsic features, revealing them as highly promising devices for bioimaging and optoelectronic applications. [33] [17] [11]

Since graphene has such great features, among all the CDs described above, GQDs are the preferential to be used on biomedical applications. When optimised, their CVD production may become the best way to enhance the large scale production of one of the most pure GQDs. [17]

1.2.2 Optical Properties

Although the optical properties of CDs are dependent on a number of factors, there are some common aspects that must be referred.

CDs all absorb in the UV region (230-320 nm) and have a shoulder extension to the VIS wavelengths. In UV range, they usually have a carbon peak at 230 nm due to the π-π* transition of aromatic C=C bonds. The shoulder in the VIS region at about 300 nm is related with the n-π* transition of the C=O bonds or with the contribution of connected groups. Different values or shifts relatively to them may correspond to different hybridizations or compositions. [13] [15] [5] [14] [41]

The mechanisms of photoluminescence (PL) or fluorescence of the carbon dots are actually being hardly studied nowadays since they are not well-known or understood. However, there are four consensual mechanisms and features that are believed to be behind their PL properties: the quantum confinement effect (QCE), the surface state, molecule state and the cross-link-enhanced emission (CEE) effect. [14] [15] [5]

The QCE or conjugated π-domains is related to the carbon core. The surface state is determined by hybridization of the carbon backbone and the connected chemical groups, whereas the molecule state is determined by fluorescent molecules connected on the interior or on the surface of CDs. [14] [5] [13]

The fluorescent emission spectra of CDs are roughly symmetric and show broad and excitation wavelength-dependent peaks. They usually suffer redshifts when the excitation wavelengths (λ_{ex}) increase from 300-470 nm, having a maximum emission for λ_{ex} = 360 nm [13]. This Stokes shifts are higher than the ones suffered by organic emission dyes. PL wavelength dependency may result from a wide distribution of sizes within the dots suspensions, from different chemical surfaces or emissive traps or even from unknown PL mechanisms. [41] [5] [15] [14]

The emissive PL intensity and wavelength are directly related to the energy gap that exists between the highest occupied molecular orbital (HOMO) and the lowest unoccupied molecular orbital (LUMO). As it was mentioned above, they are dependent on some factors like CDs size and thickness, where single layer nanoparticles show different PL from bi-layer or multilayer ones. Besides, the pH of the solution also counts, being the PL emission stronger for alkaline solutions then for acidic ones. The colour on which CDs emit is also tunable due to its dependency on the superficial groups more than on the particles size [41] [9]. Although the majority of the CDs have blue-green emissions, there are others that may emit in yellow [26] or higher wavelengths [9]. Table 1 shows some different examples of these different PL behaviours. [5] [15] [14]

Two other important optical parameters are: the quantum yield (QY), which is defined as the ratio of the number of photons emitted to the number of photons absorbed; and the photostability, that measures how the PL is affected from the time of exposure to excitation [13]. The QY of CDs depends on the synthetic pathway used and on their superficial chemistry. The first values were very low, of about 1%, which means that per 100 photons absorbed just one was emitted. Due to chemical manipulations of CDs surfaces that give them strong superficial PL centres and increase the synergy between carbon core and chemical groups, their QYs were highly increased as it is possible to confirm in Table 1 [9]. The majority of the CDs have high photostability due to the PL carbon-based core. There are no significant reductions or blinking after continuous exposure [13], unless in CDs with molecule-state emission. For these CDs, the PL intensity decreases strongly after UV high-power exposure. [41] [9] [5] [15] [14]

1.2.3 Therapeutic applications

CDs were already used for several applications in electronics, energy-related uses and biomedicine [41] [13] [15] [14]. Regarding CDs' therapeutic applications, the most relevant are their bioimaging and biosensing applications, as well as their use as drug delivery systems [41] [13] [42] [43] [44].

As an example of the use of CDs as drug delivery systems the work of *Liu et al.* [45] with nano-graphene should be highlighted. The team attached SN38, an insoluble aromatic drug, onto PEGylated nano-graphene. The complexes they created have shown about 1000-fold more potent cell killing effect in vitro than free SN38 dissolved in DMSO. They also found that doxorubicin could be loaded by physisorption onto nano-graphene functionalized with antibodies to selectively kill cancer cells.

Fan et al. [41] produced boron-doped GQD as highly fluorescent bright biomarkers for cellular imaging and chemosensors for detecting Al_3^+. Carbon dots were also used as DNA cleavage systems [46].

Due to the bright PL and their low cytotoxicity, *J. Peng* [47] successfully applied GQDs in high contrast bioimaging in human breast cell lines T47D. Moreover, due to the excitation-dependent PL behaviour, the authors could give rise to numerous visible results, as also did *Zhu et al.* [48] with MG-63 cells. *Dong et al.* [24] labelled human breast cancer MCF-7 and other groups as *Zhou et al.* [43] also incubated HeLa cells with green luminescent GQDs. GQDs were thus confirmed to be able to label cell cytoplasm, membrane and nucleus at the same time.

1.3 Doxorubicin

1.3.1 Chemical Properties

The hydrochloride salt of doxorubicin (DOX) belongs to the anthracyclines family, a group of anti-carcinogenic drugs. The antineoplastic antibiotic is obtained from *Streptomyces peucetius* and is a derivative of Daunorubicin. [3] [49] [1] [50]

DOX is a red crystalline solid at 25 ºC and its melting point is 230 ºC. [50] The chemical structure is shown in Figure 4 and is characterized by the planarity of the tetracyclic ring [3] [50].

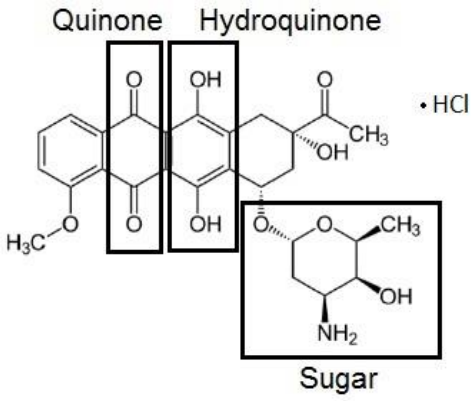

Figure 4- Doxorubicin chemical structure. Tetracyclic ring (anthracyclinone) bonded to daunosamine sugar.

As shown in Figure 4 the molecular formula of DOX is $C_{27}H_{29}NO_{11}$ [50]. HCl with the correspondent molecular weight of 579.983 g/mol [50]. Doxorubicin is composed by a quinone and hydroquinone tetracyclic ring (anthracyclinone) bonded to a daunosamine sugar. The presence of quinone and hydroquinone moieties on adjacent rings enhance the loss and gain of electrons and consequently the propensity of the molecule to react with iron to form free radicals. These radicals form reactive intermediates that disrupt nucleic acid bases, being this mechanism responsible for the antineoplastic

activity and high toxicity [50] [3]. Further description of DOX mechanism of action will be given on the next section.

DOX has a water solubility of 2%, being soluble in aqueous alcohols, moderately soluble in anhydrous methanol and insoluble in apolar organic solvents [50] [3]. The dissociation constants of DOX are pK_1=8.15, pK_2=10.16 and pK_3=13.2, with an isoelectric point of pI=8.40 [51].

It is also important to mention the DOX dimerization that may occur for concentrations as low as 1 µM [52]. Dimerization is the process of self-aggregation that the drug suffer where the monomers aggregate to each other forming oligomers. It may occur at low and high concentrations. For low concentrations, dimerization occurs due to the stacking of the planar aromatic rings of the anthracycline, resulting from the interaction between their π electrons. This self-aggregation is enhanced by increasing ionic strength and happens for all doxorubicin salts. The aggregates' size increases with the increase of DOX concentration. The massive precipitation that can be seen by naked eyes occurs at much higher DOX concentrations. This specific event depends on the counter-ion of the medium, varying the concentration of DOX from >100mM for glucoronate to 2mM for sulphate. [52] [53] [54]

1.3.2 Mechanism of action and therapeutic applications

Doxorubicin's antineoplastic effect is mainly due to three cytotoxic mechanisms of action: (i) inhibition of topoisomerase II enzyme; (ii) interleaving in DNA sequence or (iii) formation of reactive oxygen species (ROS). All of these processes have a harmful effect on DNA synthesis. [50] [3] [1]

Topoisomerase II inhibition induces the break of single and double strands of the DNA helix. The interleaving of the DOX in DNA sequences inhibits the action of DNA and RNA polymerases, compromising the recognition and specificity of the nucleotides. Finally, DOX may induce ROS formation like $HO^{\bullet}$ radical, which are strongly reactive and may cause DNA demerger, enhancing mutagenesis and chromosomic aberrations. [1] [49]

As a result of the mentioned cytotoxic mechanism, DOX has the ability to damage tumour cells, compromising their development and proliferation. Therefore, DOX is the "first line" drug used to fight most of the cancer types, from lymphatic cancers to hard or soft tissues' ones. DOX is also applied in nerve tissue or kidney cancers. [49] [1] [3] [50]

The specificity of DOX toxicity towards cancer cell tissues is related solely to cell division process. Therefore, normal tissues that possess proliferative cells, such as the bone marrow, gonads and all the tissues from gastrointestinal tract are the most affected normal tissues when DOX interact with them. [49] [1] [50]

Besides presenting lack of selectivity for cancer tissues and serious toxicity in health tissue cells, DOX therapeutic administration faces another problem that may compromise its efficiency: the development of resistance in cellular cancer tissues. To circumvent this problem it is possible to combine DOX with

other drugs (e.g. verapamil) to inhibit cellular resistant mechanisms of drug excretion and to promote the cellular uptake of DOX. However, this therapeutic strategy also causes huge toxic effects. [50] [1]

Another aspect that may compromise the therapeutic efficacy of DOX is the dimerization effect. The impact of oligomerization is not yet clear, but based on geometric considerations non-monomeric DOX cannot interact with DNA in the same way as monomeric. Besides, the exact location between DNA strands should differ. This means that the drug therapeutic efficacy will depend on the form at which the DOX is when internalized by the tumour cells, being the oligomers considered to be less efficacious. [52]

Regarding DOX clinical administration, it can be administrated alone or combined with other anti-tumour drugs, always under medical supervision. The administration routes are intravenous or bladder perfusion. Given that DOX provokes numerous and serious toxic effects on patients. Adult human beings can support a maximum cumulative dose of 450-550 mg/m^2 of DOX, whereas children can only achieve 300 mg/m^2. [1] [50]

For all the pointed reasons it is clear that despite DOX being a potent and first class drug in cancer therapies, there is still much room for improvement in new formulation strategies.

1.3 3 Optical Properties

The optical properties of the anthracyclines result from a complex interplay of several factors as the environment at which they are and the interactions with lipids, surfactants or membranes. However, their self-association into dimers above a critical concentration is one of the most relevant factors to take into account in optical analysis. [53] [54] [52]

The UV-VIS absorption spectrum of DOX has a broad main band with its centre at 490 nm and a shoulder at 360 nm [55] [56]. This shape is related with the π-π* transition ($^1A \rightarrow {}^1L_b$) polarized along the long axis and to the partially forbidden by electric dipole n- π* transition ($^1A \rightarrow {}^1L_a$) of the three C=O groups, respectively [53] [57]. The DOX absorption is strongly affected by the protonation state of the dihydroxyanthraquinone and almost unaffected by the protonation of the sugar that is not conjugated with the aromatic ring. The self-aggregation of DOX also affects its absorption [57]. There is a broadening of the peak with a hypochromism between 451-540 nm and a hyperchromism above 540 nm. [53] [55] [54]

Fluorescent behaviour of DOX is a much more complex mechanism. DOX fluorescence is wavelength dependent and the emission peaks alter in different ways with the type of solvent where DOX is solubilized, the pH of the solution and the concentration of DOX [52] [51] [58]. In general, the DOX fluorescent peaks are associated with the vibrational progress of the symmetric modes of C=O bending, the OH bending motions of the dihydroxyanthraquinone and with the skeleton stretching [57]. The two main characteristic peaks appear at 560 nm (I_1) and 590 nm (I_2), being possible to occur a third peak at 630 nm (I_3) [57]. The intensity of the maximum wavelength and the ratio between the intensities of the

two characteristic peaks are good indicatives of interactions between DOX and DNA or macromolecules and also enable the localization of DOX within lipid bilayers and liposomal delivery systems. Increasing and quenching of fluorescence may occur and mean different biological situations. [57] [59]

In terms of solvent dependency, for all solvents there are always the two characteristic peaks at 560 nm and 590 nm. For solvents with lower dielectric constants, a shoulder at 630 nm appears. The ratio between I_1 and I_2 vary in a parabolic way with the dielectric constant of the medium, being their intensity dependent on the excitation wavelength with some spectral shape variation. Besides, I_1 and I_2 also suffer a blue shift of about 5 nm with the increase of the dielectric parameter. [59] [57]

In aqueous solutions, considering DOX concentrations of 5 µM and an excitation wavelength of 479 nm, fluorescent intensity decreases without shifts with the decrease of pH in the range of pH=5.52 and pH=10.40. There is also an increase of the I_1/I_2 ratio for alkaline solutions. [59] [57]

For an excitation of 479 nm of variable concentration solutions, the DOX fluorescence quenches due to the self-association of DOX monomers into dimers at concentrations above 10 µM. At that concentration, 47% of the drug is dimerised and there is a significant decrease on the fluorescent intensity, since the monomers have 1ns lifetime and the dimers have 2 ps. The QY and the I_1/I_2 ratio also decreases with the increase of DOX concentration and the spectrum has a redshift of about 25 nm. [59] [57]

1.4 Liposomes

Drug delivery systems have suffered a huge development in last decades. Nowadays' systems are more focused on selective delivery, with less secondary effects for patients and lower amount of drugs needed. To achieve this, the use of drug nanocarriers increased significantly. One important category of these nanocarriers is the lipid nanocarriers. [60] [61] [62] [63] [64]

Lipids are mainly composed by carbon, hydrogen and oxygen and are generally defined as substances of biological origin that are soluble in organic or nonpolar solvents. Chemically, lipids can be broadly defined as hydrophobic or amphipathic. According to this classification, hydrophobic lipids are insoluble in water. On the other hand, amphipathic or amphiphilic lipids have a polar headgroup and a non-polar tail, being able to self-assemble in water forming different aggregates such as vesicles or micelles (Figure 5). [65] [66]

The self-assembling process of amphiphilic lipids in water is driven by the so called hydrophobic effect. When amphiphilic lipids are put in water, they spontaneously rearrange themselves into monolayers or lipid bilayers due to hydrophobic interactions. This happens in order to maximize the interactions between water and polar heads, which are energetically favourable, and to minimize the contact between hydrophobic tails and water, that is energetically unfavourable. [65] [66]

Hydrophobic interactions may induce the formation of monolayers at the air-water interface and after reaching a critical lipid concentration, micelles are formed by self-assembling of the amphiphilic lipids

that position their hydrophilic "head" regions in contact with surrounding solvent, sequestering the hydrophobic single-tail regions in the micelle centre. Hydrophobic interactions may also induce the formation of lipid bilayers that self-assemble in a vesicle shape, where the hydrophobic tails of the amphiphilic lipids go to the inner part of the bilayer and the hydrophilic headgroups are in contact with the aqueous solvent. The aqueous solvent is present both externally to the vesicle and also at its inner core as shown in Figure 5. Artificial lipid vesicles that are mainly composed by phospholipids are also designated by liposomes. [65] [66] [67]

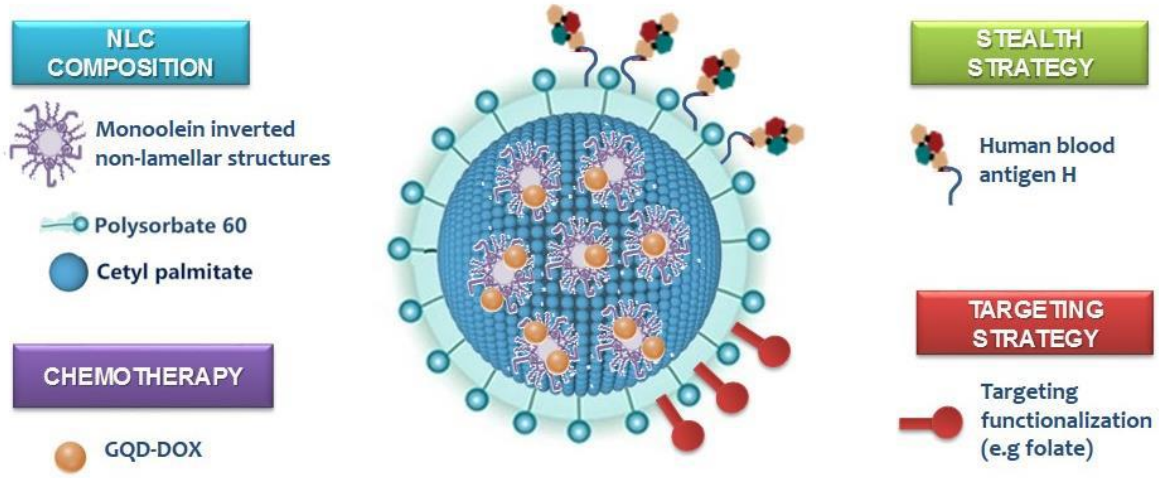

Figure 5 – NLC composition: Monoolein inverted non—lamellar structures, polysorbate 60, cetyl palmitate. Chemotherapy: GQD-DOX. Stealth strategy: Human blood antigen H. Targeting strategy: targeting functionalization (e.g folate). [2]

Within the numerous colloidal self-assembling systems, liposomes have a preferential emphasis since they mimic the natural lipid environment of biological membranes. They were firstly studied as membrane models, being rapidly recognized as potential drug delivery nanocarriers due to their significant strengths. Liposomes have high biocompatibility and biodegradability and are easy to functionalize in order to improve their selectivity. Their structure is versatile and can be modified to encapsulate different cargos. The size of these lipid nanocarriers may also be controllable and adjustable depending on the biological application that they are designed for. We can even produce liposomes small enough so that they can pass through biological barriers. Moreover, their amphiphilic character also allows them to carry therapeutic agents of different lipophilicity, from the hydrophilic to lipophilic or amphiphilic ones. [62] [65] [68]

Phospholipids, the main component of liposomes, are amphiphilic molecules containing a polar hydrophilic headgroup and two fatty acid non-polar tails. Phospholipids possess lyotropic polymorphism and can assemble in different phases as a function of both temperature and concentration of the phospholipids in a solvent (typically water) as well as other factors such as the geometry of the phospholipid molecule. The most common lipid phases in water are the micellar (M), hexagonal (H), cubic (Q) and lamellar (L). [66] [69] [70]

In physiological conditions the most common lipid phase is the lamellar liquid-crystalline phase also designated as fluid phase (L_α). L_α is the phase where the lipids motion is assured by the movement of fatty acid chains and the rotation of C-C links of the hydrophobic tails [71]. From polar headgroups to fatty acid tails there is a gradient of motion freedom. Hence, in a lipid bilayer, the polar headgroup is the most ordered region while at the hydrophobic tails extremity there is the higher motion freedom and thus the less ordered regions. The L_α phase can be obtained by increasing the temperature as it promotes an increase of molecular motion. Contrastingly, at lower temperatures the lipid molecules are more confined and possess less freedom to move forming a lipid phase designated as the lamellar solid-crystalline phase or gel phase (L_β). The temperature at which the lipid phase changes from L_β to L_α is the main phase transition temperature (T_m) above which liposomes become fluid (Figure 6). For liposomes to be efficient as nanocarriers they have to have enough superficial fluidity to allow the passage of cargos through the lipid membrane. Therefore, when producing liposomes as delivery systems, care should be taken with the temperature which should be always above T_m [71]. [65] [66] [69] [70]

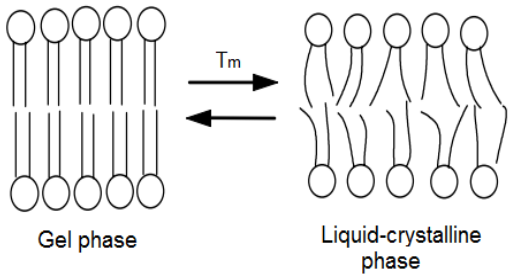

Figure 6 - Phase transition of lipid membranes due to temperature variation. The transition from gel phase to fluid phase occurs above the main phase transition temperature, T_m. (adapted from [72])

The type of phospholipids used to produce liposomes is chosen depending on the liposomes final application. In order to mimic a typical cellular membrane we have to take into account the main component of eukaryotic biological membranes, the phosphatidylcholines (PC) [66]. Considering the requirement of mimicking the membranes' lipid phase it is possible to produce PC liposomes that differ in the fatty acid composition of the phospholipids, e.g. DMPC (dimyristoylphosphatidylcholine) [73] [74] or DPPC (dipalmitoylphosphatidylcholine) [75] [76]. Therefore, with the goal of mimicking the main fluid lipid environment found in cellular membranes we have opted to produce liposomes composed of DMPC as it originates fluid membranes at physiological temperature (T_m =23 º C) (Figure 7). [77] [65] [67]

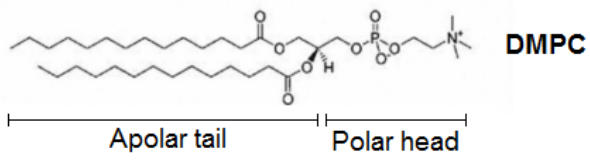

Figure 7 - DMPC structure with evidence of non-polar tail and polar headgroup. (Adapted from [67])

Depending on liposomes' size and structure they may be divided into three main groups shown in Figure 8. Multilamellar vesicles (MLVs) are larger than 0.5 µm and are composed by "onion-like" multiple concentric lipid bilayers and aqueous chambers. Given their high number of lipid bilayers, MLVs are preferred for carrying lipophilic cargos. MLVs may be processed to smaller sizes into Large unilamellar vesicles (LUVs) or Small unilamellar vesicles (SUVs). LUVs are vesicles of only one phospholipidic bilayer with dimensions between 100 and 1000 nm. SUVs are about 20 -100 nm in diameter and have limited encapsulation ability. SUVs are thermodynamically unstable and tend to aggregate but present higher biological half-time than LUVs. [66] [62]

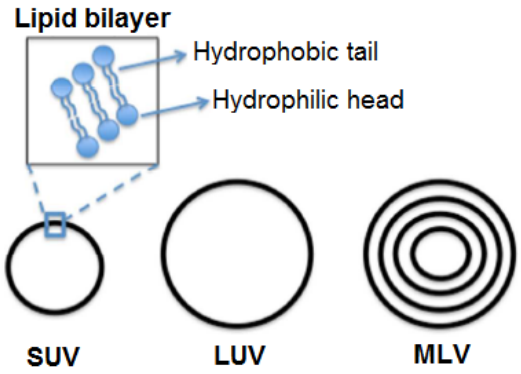

Figure 8 - Different types of liposomal vesicles: SUV (Small Unilamellar Vesicle), LUV (Large Unilamellar Vesicle) and MLV (Multilamellar Vesicle). Each circle represents a lipid bilayer. (Adapted from [66])

Conventional liposomes are the simplest liposomal conformation, composed by simple phospholipids. Technological advances allowed the appearance of more complex liposomes bearing different delivery strategies. Innocuous liposomes are the ones coated with hydrophilic polymers that cover the outer lipid leaflet. This new generation of smart delivery systems are liposomes functionalized at their surface with polymers, e.g. polyethylene glycol (PEG) that increases liposomes' shelf stability and prolongs liposomes' body circulation time (stealth liposomes). Other liposomal group belongs to the directed liposomes, which are the ones functionalized with polymers bearing ligands for different cellular targets (target liposomes). Finally we may consider the biosensible liposomes that have a modified lipid composition that react to different body stimuli releasing their cargo whenever these stimuli (pH, temperature, ROS, etc) are present (triggered release liposomes). It is also possible to produce liposomes for the co-delivery of different cargos, e.g. nucleic acids in combination with drugs [78]. [66]

In sum, liposomes have acquired a crescent relevance as nanodelivery systems by their numerous advantages: (i) liposomes allow a sustained release of drug (ii) liposomes are specific due to the targeting strategies that direct the drug delivery to the target tissue; (iii) liposomes may increase drugs' bioavailability and cellular absorption; (iv) liposomes possess a good encapsulation efficiency being able to deliver greater amounts of drugs. Furthermore, liposomes are versatile working tools since we can modify their size, morphology and surface charge, being used not only as a delivery system but also as a mimetic system to study membrane biophysical properties. [60] [61] [62] [63] [64]

1.5 Methods of characterization

1.5.1 Absorbance of UV-Vis light

Spectrophotometry is widely used to study biochemical reactions. One of the main applications of this technique is to calculate the concentration of a solute in solution through the measurement of its absorbance. [79] [80]

Beer-Lambert law (Eq. 1) relates those two parameters with the molar absorptivity (or the molar extinction coefficient) (ε) and allows us to calculate the desired concentration *C* (M) of a solute. *A* is the absorbance and *l* is the path length or distance the light travels through the sample. [80] [79]

$$A = \varepsilon . C . l \tag{1}$$

Absorbance or optical density is dimensionless and is also given by (Eq. 2) that establishes the relation between incident intensity of light (I_0) and the transmitted (I) one, where *log* is the logarithm of base 10. [79] [80]

$$A = log \frac{I_0}{I} \tag{2}$$

Molar absorptivity is expressed in $L.mol^{-1}.cm^{-1}$ and depends on the incident wavelength, being higher for the wavelength where the absorption is greater. After determining the ε of a solute we can calculate (within a concentration interval where the Beer-Lambert is applied) any solute concentration only by measuring its absorbance (Eq. 3) [80] [79]

$$C = \frac{A}{\varepsilon . l} \tag{3}$$

1.5.2 Fluorescence (FL) emission and fluorescence quenching

Fluorescence is an emitting process based on atomic or molecular excitation by UV-VIS light [79]. The incident beam carries photons with enough energy to excite electrons from a fundamental singlet state (S_0) to a superior singlet energy level (S_1, S_2, etc.). All the energy levels have several excited vibrational states that may be occupied during the electron transitions (Figure 9).

The decay of the excited electrons back to the fundamental state may occur by different pathways: internal conversion (IC); intersystem crossing (ISC); fluorescent or phosphorescent emission or by a simple vibrational relaxation, and the probability of each of these pathways is defined by the molecule chemical structure and the environment.

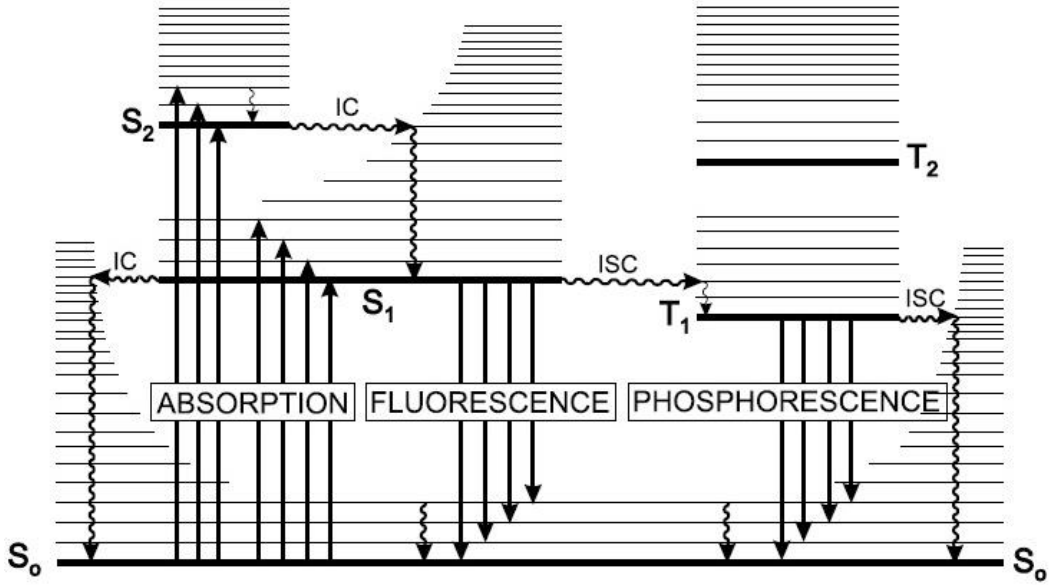

Figure 9- Perrin–Jablonski diagram. [7]

In the case of IC, the electrons transit from the lowest singlet state of a superior energy level (S_2) to a similar energetic vibrational state of an inferior level (S_1). By ISC, electrons transit from the lowest singlet state of a certain energy level (S_1) to a triplet state of the energy level (T_1), losing energy by changing their spin. When electrons are in excited vibrational states they achieve the lowest state of that energy level through vibrational relaxation.

Fluorescent and phosphorescent emissions are radiative decays, where a photon is released. Fluorescence occurs from the transition of electrons from the singlet Lowest Unoccupied Molecular Orbital (LUMO) (S_1) to the singlet Highest Occupied Molecular Orbital (HOMO) (S_0), whereas phosphorescence corresponds to the decay from the lowest triplet state (T_1) to the fundamental state (S_0).

Since the relaxation from the excited state to the ground state implies energy loss, the wavelength of fluorescent emission is not the same as the absorbed. There is a Stokes shift due to the decrease on the energy gap between HOMO and LUMO.

The relative incidence of these competitive events will lead to different energy losses and will define the Quantum Yield (QY) of the fluorescent molecules. The number of absorbed photons reemitted by fluorescence (QY) depend on the amount of energy lost through all the other pathways.

Fluorescent emission is a property of materials and it is a characterization technique widely used in nanotechnology experiments. [79] [81] [82]. It allows to compare samples of the same compound in different conditions or to study the influence of a medium or of other molecular species.

To analyse the fluorescent profile of an analyte in a sample we usually take the emission and the excitation spectra [81]. The emission spectrum is obtained by exciting the sample in an UV-VIS wavelength and collecting its emission in the VIS-NIR range. On the other hand, the excitation spectrum

is obtained at the wavelength where the analyte has the maximum emission and provides a confirmation of the wavelengths where the excitation is maximum. [79] [82]

Intermolecular interactions

The interaction of two molecules also affects the fluorescence properties of the intervenient species through fluorescence quenching and Förster resonance energy transfer (FRET) processes.

Förster resonance energy transfer (FRET)

FRET occurs when there is an energy transfer from a donor to the acceptor, the photons that would be emitted from the donor are absorbed by the acceptor, which will in turn emit fluorescence. For this to happen, the species have to be in a distance below the Förster radius (R0), which corresponds to a FRET efficiency of 50% (**Erro! A origem da referência não foi encontrada.**).

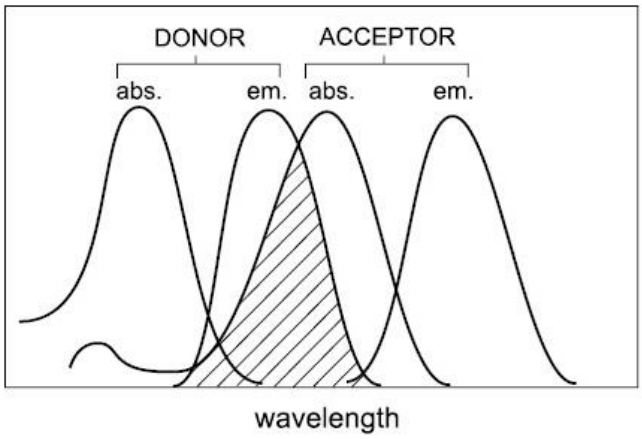

Figure 10 – FRET Energy level scheme of donor and acceptor molecules showing the overlap between the emission spectrum of the donor and the absorption of the acceptor.

Therefore, FRET is entirely dependent on the distance between the molecules (r_{DA}) and the transfer efficiency (E) which is the fraction of photons absorbed by the donor that are transferred to the acceptor, given by:

$$E = \frac{{R_0}^6}{{R_0}^6 + {r_{DA}}^6} \tag{4}$$

E is typically measured using the relative fluorescence intensity of the donor, in the absence (ID) and presence of the acceptor (IDA):

$$E = 1 - \frac{I_{DA}}{I_D} \tag{5}$$

From Eq. 6 it is possible to calculate the distance between donor and acceptor:

$$R_0 = 0.211(k^2 n^{-4} Q_D J(\lambda))^{1/6} \tag{6}$$

where k^2 is a factor describing the relative orientation in space between the transition dipoles of the donor and acceptor, n is the refractive index of the medium, Q_D is the quantum yield of the donor in the absence of acceptor, and J(λ) is the overlap integral in the region of the donor emission and acceptor absorbance spectra (with the wavelength expressed in nanometers).

Fluorescence Quenching

Fluorescence quenching processes correspond to the decrease of fluorescence of a molecule caused by molecular interactions between its fluorophore and a quencher. There are two kinds of mechanisms responsible for fluorescence quenching: [83] [84]

i) Static quenching: in static quenching a non-fluorescent complex is formed between the fluorophore and the quencher. When this complex absorbs light it immediately returns to the ground state without emission of any photon; [83] [84]

ii) Dynamic or collisional quenching: in the case of collisional quenching, the quencher must diffuse to the fluorophore during the lifetime of the excited state. Upon contact, the fluorophore returns to the ground state, with emission of a photon. In general, this quenching process occurs without any permanent change in the molecules, that is, without chemical reaction. [83] [84]

Static and dynamic quenching can be distinguished by their differing dependence on temperature, viscosity and lifetime measurements [85]. In the case of dynamic quenching, higher temperatures result in faster diffusion and hence larger amounts of collisional quenching; while in the case of static quenching higher temperature will typically result in the dissociation of weakly bound complexes, and hence smaller amounts of static quenching. Nevertheless, the most effective way to distinguish the type of quenching is by lifetime measurements, and if the quenching process has a dynamic nature it will occur an equivalent decrease in fluorescence intensity and lifetime. [83] [84]

1.5.3 Dynamic Light Scattering (DLS) and Electrophoretic Light Scattering (ELS)

In colloidal suspensions, the particles present Brownian motion, which are random variations on their direction due to intermolecular collisions [86]. It may be caused by particles colliding with each other, with the molecules of the solvent or even with small microorganisms present in a sample. It may also be induced by external electric or magnetic fields. [87] [88]

Dynamic and electrophoretic light scattering take advantage of the Brownian motion of suspended particles, measuring their size and inferring their surface charge through the light scattered by them. [86]

1.5.3.1 DLS - size measurement

Dynamic Light Scattering, also known as Photon Correlation Spectroscopy (PCS), is a non-invasive technique that allows us to obtain the hydrodynamic radius (R_H) of colloidal particles and its distribution. A laser beam incident in a suspension is scattered according to the particles size. The experimental setup is shown on Figure 11. [86] [88]

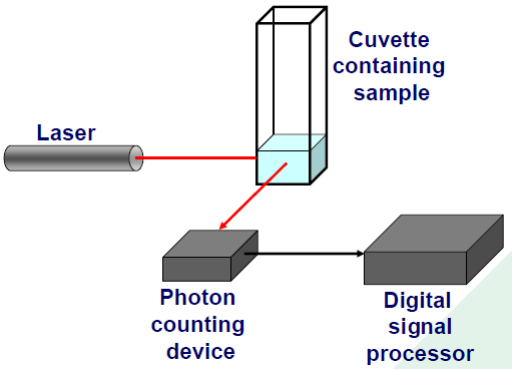

Figure 11 - DLS experimental setup. [88]

The intensity of scattered light fluctuates in time and is measured as a function of the transitional diffusion coefficient (*D*). *D* represents the velocity of the particles' Brownian motion and depends not only on the particles' size, but also on the medium's absolute temperature (*T*) and viscosity (η) during the measurement. The relationship between these parameters is given by Stokes-Einstein equation (Eq. 4), where *K* is the Boltzmann constant and R_H the hydrodynamic radius of spherical particles. [88] [86]

Although the particles in suspension may not be perfectly spherical, there is a mathematical approximation to a spherical model in order to calculate the average size of the particles' population. Actually, upon a DLS analysis of a suspension of particles, the value of R_H obtained corresponds to an average *D* and is estimated from the radius of a spherical particle that would have the same *D* value. R_H will depend not only on the particle size, but also on the existence of surface functionalization, surface adsorption or on the presence and concentration of ions in the solvent medium. [88] [86]

According to Eq. 4, R_H and *D* are inversely proportional, showing the evidence that the smallest the particle is, the higher its velocity becomes.

In fact, intermolecular interactions have more impact in smaller particles due to their lower resistance to motion. They change their positions more often and with higher velocity than the bigger ones. In the same way, the biggest the particle is, the lower its motion becomes. [88] [86]

$$D = \frac{K.T}{6.\eta.\pi.R_H} \tag{7}$$

As a result of the different Brownian motion, the scattered light behaviour will be different when it occurs due to small or large particles. Small particles will induce strong variations on light scattered directions. Therefore, the detector will capture different signal intensities in short periods of time (τ) due to constant deviations of scattered beam. Oppositely, big particles will deviate the scattered beams more slowly in the same τ, causing smaller fluctuations on received intensities. Figure 12 shows the difference in detected signals from small to large particles. [88]

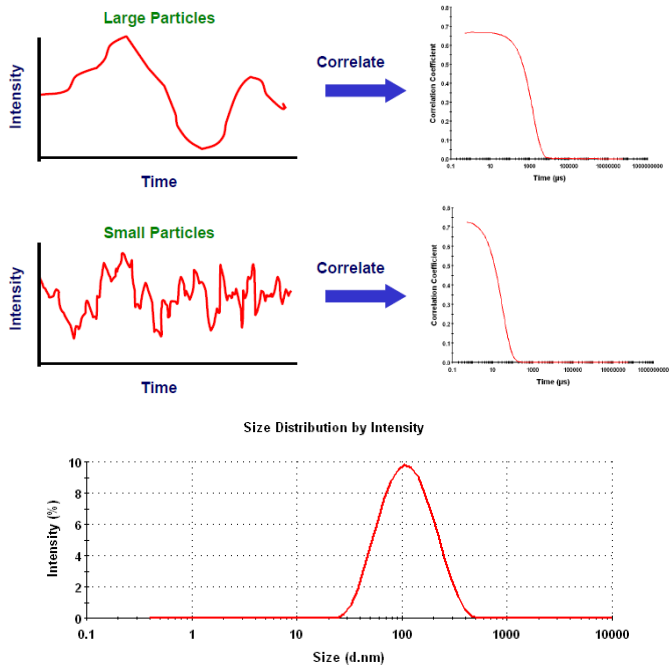

Figure 12 - Size-dependent fluctuations of the light scattered signal for large and small particles. Size final spectrum. [88]

To obtain a specific value for particles' size, DLS software uses a correlator that analyses the temporal variation of the detected intensity. The correlator constructs an auto-correlation function that characterizes mathematically that variation, taking into account the parameter D, among other factors. Figure 12 shows correlation functions, where the time at which decay starts indicates the mean size and the gradient indicates the polydispersity of the sample. This model suffers another conversion to a size distribution function, where we can finally obtain concrete numbers of R_H. [88] [86]

1.5.3.2 ELS – zeta potencial (ζ) measurement

Every colloidal particle acquires charge when it is put in suspension. It leads to an electrostatic attraction of counter-ions that will form a stable layer on the surface of the particle. This first layer is called Stern layer which in turn will attract other ions. A second dense layer is formed, this time with ions with both charges that balance each other dynamically. They create an ion cloud around the particle and are known as diffuse layer. Both layers together are known as the electrical double layer. [87] [89] [88]

Zeta potential is the Stern layer potential and it is extremely important to predict the stability of a colloidal suspension. The greater the zeta potential is, the more stable the suspension is likely to be [89]. When ζ values are significant, it means that particles strongly repel each other and thus the suspension is stable. Zeta potential is not a measure of the particle surface charge, but it is considered to be related with the particle surface charge and characterizes its hydrodynamic behaviour. Zeta potential is also crucial in electrokinetic phenomena like electrophoresis and electroosmosis. [88]

Electrophoresis is the movement of charged particles relatively to a stationary fluid where they are suspended. It occurs when an external electric field is applied. Eletroosmosis is the movement of a liquid relatively to stationary charged surface due to the presence of an electric field. [88]

Electrophoretic Light Scattering (ELS) allows the determination of zeta potential of the particles according to their electrophoretic mobility (μ_e). The relation between both is defined by the Henry equation (Eq. 5), where ε is the fluid dielectric constant, η its viscosity and $F(ka)$ the Henry's function. F is dependent on the particle radius a and on the electrical double layer thickness K, known as Debye length. [88]

$$\mu_e = \frac{2\varepsilon F(Ka)\zeta}{3\eta} \tag{8}$$

To obtain zeta potential through electrophorectic mobility, ELS software measures the light variation by Doppler shift. Instead of measuring directly the time rate of intensity variation, the software calculates a frequency shift on scattered light caused by particles in motion. [88]

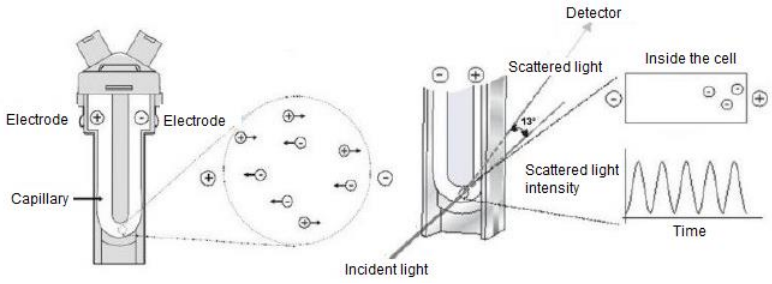

Figure 13 - ELS measuring cell and process. [88]

The colloidal suspension is put into a cell that contains two electrodes as demonstrated in Figure 13. When electrical current is applied to the cell, there is an induced electric field generated within the sample. This will promote the particles' motion according to their charge. During this electrophoretic motion a laser beam is incident in the sample to promote a Doppler Effect. [88]

Laser Doppler Electrophoresis is done by using an optical interferometer technique (Figure 14). A single laser source originates a pair of mutually coherent laser beams. One of them passes through the sample and will be scattered and frequency shifted, and the other is routed around the sample, being the

reference one. At the end, both beams are put together and originate a modulated signal with intensity variations and a wavelength equal to the difference of both separate beam frequencies. [88]

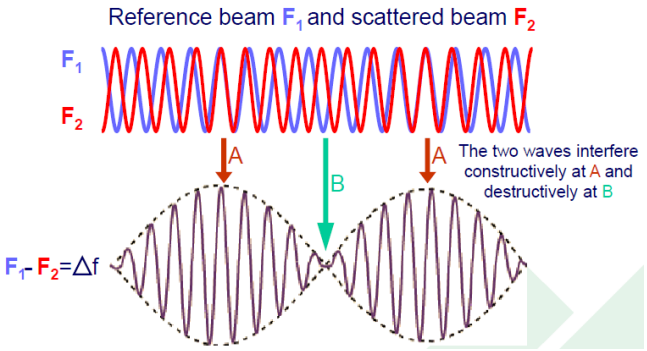

Figure 14 – Laser Doppler effect in ELS. [89]

Different particles with different velocities will create different modulated signals. This happens since a different velocity will create a different frequency shift on scattered beam. Therefore, comparing the frequency of modulated signal with the frequency of the reference beam it is possible to know the mobility of the particles and thus the zeta potential. [88]

1.5.4 Raman Spectroscopy

When light interacts with matter, it can be either reflected, absorbed, transmitted or scattered. In Raman spectroscopy only the scattered photons are taken into account. Scattering occurs when a photon collides with matter and it is later reemitted in a random direction. In between, it may induce a transition on matter's state passing through a virtual level of excitation. Scattering processes can be elastic (Rayleigh) or inelastic (Raman) (Figure 15). [90] [91] [92]

Rayleigh scattering is based on elastic collisions, where the incident photon is equal to the emitted one [91]. There is no energy transfer between photons and matter and there is no wavelength shift. This is the most common scattering phenomenon. [90] [92]

Raman scattering occurs due to inelastic collisions between light and matter, changing the photons' wavelength. This change is known as Raman effect and can be either to red (Stokes) or blue (anti-Stokes) direction if the photon loses or gains energy, respectively. [93] [92]

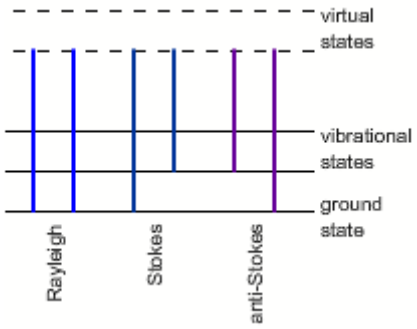

Figure 15- Light scattering. In Rayleigh elastic scattering there is no wavelength change. In Raman inelastic scattering a wavelength shift occurs: Stokes shift (red shift) and anti-Stokes shift (blue shift). [92]

Stokes' shift is the most common. Photons interact with the electronic cloud of the functional groups bonds and excite electrons to a virtual state. Electrons then relax to an excited vibrational state. In this process the initial photons lose energy and are emitted with a higher wavelength (red shift). Detectors capture them as Stokes Raman scattering and their energy loss is equal to the final vibrational state energy of matter (Figure 15). [93] [91] [92]

Anti-Stokes shift is less common since it occurs when the matter is already in an excited vibrational state. The photon collides with excited matter, transferring it to a virtual state of higher energy. The electrons then relax, but this time to the fundamental state. Emitted photons have more energy than initial ones and it corresponds to a blue shift. There is a decrease in the wavelength and photons are detected as anti-Stokes Raman scattering (Figure 15). [93] [92]

In both cases the wavelength shift of the photon is directly associated with the energy of the excited vibrational or rotational states that matter has at the beginning (anti-Stokes) or reaches at the end (Stokes). These states are dependent on the molecular structure of compounds analysed and their functional groups, as well as on the type of atoms that compose the molecule and its environment. [91] [93] [92]

Therefore, a Raman spectrum is considered a molecular fingerprinting, giving all the shifts suffered by the incident UV or VIS monochromatic light due to inelastic collision with matter. The information is given in a range of wavenumbers' shift. What is seen is not the absolute wavenumber but the shift in that unit. Each peak corresponds to a certain binding that causes that specific shift on photons' wavelengths. The intensity of the peaks is proportional to the number of molecular bonds that cause them. Comparing with tabled values it is possible to know which molecular bonds are present in a sample. [90] [93] [92]

Confocal Raman

Confocal Raman microspectroscopy technique conjugates a confocal microscopy with the mentioned Raman spectroscopy. It gives more detailed information about a sample, with higher spatial resolution

and clear image quality. There is no need of sample preparation, enabling great chemical differentiation and 3D mapping of bulk samples. [90]

This technique is complementary to ATR-FTIR (1.5.5) on searching for molecular bindings and constitution through vibrational properties. Raman spectroscopy implies a change of molecular polarization through scattering processes, whereas ATR-FTIR is based on the variation of electrical dipolar moment by IR light absorption. [90] [91] [92]

1.5.5 Attenuated Total Reflectance – Fourier Transform Infrared Spectroscopy (ATR-FTIR)

Fourier Transform Infrared Spectroscopy (FTIR) is a characterization technique based on the interaction between infrared (IR) radiation and samples. IR spectrum goes from frequencies (f) of 10^{13} Hz to 10^{14} Hz with correspondent wavelengths (λ) of 2500-25000 nm and wavenumbers (ν) from 333 cm^{-1} to 3333 cm^{-1}, respectively. [94] [95] [96]

In ATR-FTIR mode (Figure 16), an attenuated total reflection accessory measures the attenuation of an IR beam. Initially, the beam comes onto an optically dense crystal, which refraction index is much higher than the one of the samples. [95] [97]

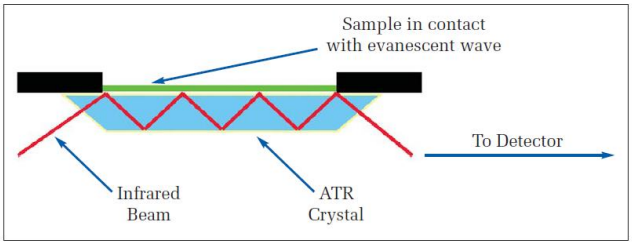

Figure 16- ATR-FTIR mode. High refractive index crystals in direct contact with the sample. Internal total reflection of IR beam and appearance of an evanescent wave. Attenuation by absortion of some wavenumbers from IR beam. [97]

The crystal is in direct contact with the sample and by choosing the correct angle of incidence the internal total reflection occurs. An evanescent wave is created on the interface of the crystal and the sample, and softly penetrates the last in approximately 0.5 to 5 µm. There will be an attenuation in IR regions where the sample absorbs. At the end, after a concrete number of reflections, the beam is collected by a detector and the system will create an infrared spectrum. Applying the Fourier Transform, the detected signal is converted into a final one, where it is possible to analyse the intensity of the beam at different wavenumbers after reflection and absorption phenomena. It is possible to generate either an absorbance or a transmittance spectrum, each of them giving useful and unique information about samples' composition. [95] [97]

Each molecular link has its own fundamental state of vibration and has the possibility to transit to higher states of energy, the excitation states of vibration [94] [96]. When using UV-VIS light the range of energies is about 40-160 kcal/mol, equivalent to bond strength energies. IR radiation has energies between 1-10 kcal/mol, which are comparable to different conformations. Whereas UV-VIS promote high energy level transitions and can break molecular bindings, IR light allows the transition of vibrational modes. [95]

An interatomic bond has a harmonic oscillator behaviour with two movable masses. IR radiation induces vibrational modes by changing the length of bond (stretching) or the angle formed by two adjacent bonds (deformation) (Figure 17). Stretching and deformation energies are unique for each binding and depend on the type of bonds, interatomic distance and the effective mass of involved atoms. [94] [95] [97]

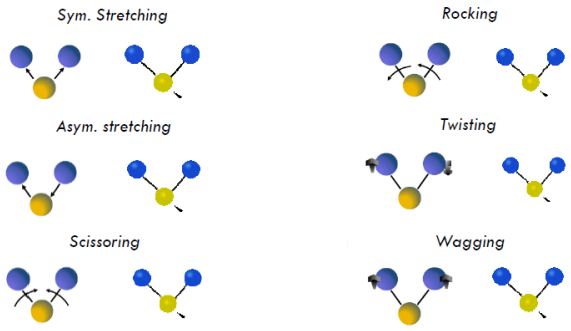

Figure 17-Vibrational modes resultant from IR radiation. [95]

FTIR spectroscopy is only possible when IR radiation excites interatomic bonds from their fundamental states to excited states of vibration, changing their electrical dipolar moment during the process. This is the main principle behind this technique. When there are no dipolar moment change, there is no signal detected and those molecules are considered inactive in IR. [94] [95] [96]

When using ATR-FTIR, IR beam will carry the range of energies necessary to excite each bond present on the sample. Each wavenumber corresponds to a specific energy that will promote the excitation of a certain interatomic binding. In the final spectra, the peaks will correspond to wavenumbers where the sample was excited and absorbed energy, attenuating the initial beam. Comparing the obtained spectra with tabled energies for known bonds it is possible to infer about samples' composition. [95] [96] [97]

ATR-FTIR can be used to characterize liquid, gaseous and solid samples, providing relevant chemical information. This technique is used essentially to confirm or discover specific molecular bindings, chemical composition and functional groups. It is highly reproducible and allows fast sampling, which turns it reliable to analyse samples of unknown compounds. [95] [97]

1.5.6 Scanning Electron Microscopy (SEM)

Scanning Electron Microscopy allows the user to observe and characterize organic and inorganic heterogeneous microvolumes and surfaces at a local scale. The materials which we want to analyse are irradiated with a finely focused electron beam that may be swept along the sample's surface or be sent statically. Electron beams are highly energetic (1-50 KeV) and have a de Broglie well-defined wavelength. As a result, they promote strong interactions with matter and higher sample's penetration comparing to the optical microscopy, generating high resolution images at the nanoscale. [98] [99] [100]

The incidence of this highly energetic beam induces several emission events, being the main of them represented on Figure 18. According to their distance from the beam's incidence region, different volumes of the sample will have different emission behaviours. [100] [99] [98]

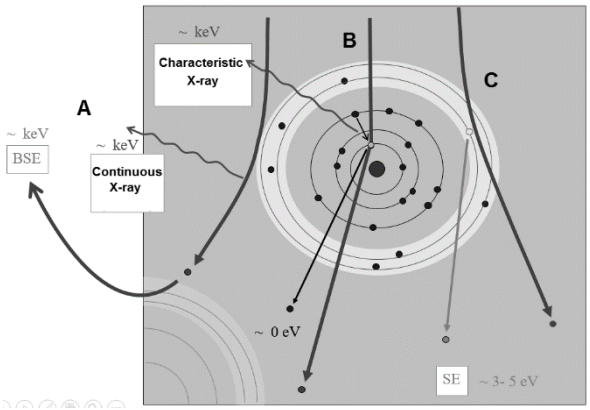

Figure 18 - SEM emission processes. A-Backscattered electrons with continuous X-ray photon emission. B-Characteristic X-ray emission. C- Secondary Electrons emission. [100]

First of all, Auger electrons will be emitted from the volume which is closest to the beam incident area. Secondly, electron beam may interact inelastically in two different situations. Electrons may ionize the external electronic layers of the atoms, emitting secondary electrons (SE), or they can ionize internal electronic layers, promoting the emission of a characteristic X-ray photon (Xr). Finally, beam electrons may also be backscattered (BSE) elastically or inelastically. In the first case there is no loss of energy whereas in the second case electrons suffer a decrease on their velocity and emit a continuous X-ray photon. [98] [100] [99]

All of these emission events may occur and be collected to analyse different properties of a specimen. SE have high topography contrast and together with BSE vary accordingly with the sample's topography when SEM beam is swept along its surface. SE allow the generation of grey images with high magnification and resolution. Bulk objects can be seen with resolutions of about 2-5 nm and in three dimensions due to the deep focus of the incident electron beam. BSE promote lower resolution images than SE due to their lower wavelength but give us higher atomic composition (Z) contrast. Conjugating BSE with characteristic X-ray emissions it is possible to make elementary analysis and find the chemical composition of the samples. In addition to the chemical and topographic characteristics, SEM can also

be used to analyse other samples' properties such as magnetic and electrical behaviour or even their crystallography. [99] [98] [100]

A scanning electron microscope is composed by a set of complex devices. SEM components include an electron gun, a lens and a vacuum system, electron collectors or detectors, visual and recording cathode ray tubes (CTRs) and all the associated electronics. [98] [100] [99]

Electron gun produces and controls the flux of electron beams and may function by thermionic effect through a tungsten (W) filament or by field effect. Field effect allows better resolutions then W filaments since it generates electrons with lower wavelengths. Typically, the λ obtained by electron microscopes are in the order of 10 pm with correspondent image resolutions of about 50 nm [79]. Lens system is constituted by the objective and magnetic capacitors that focus the beam that will lately interact with the sample in a vacuum chamber. Usually there are three different electron collectors for the different emission processes and at the end the CTRs project the detected signals on a TV or computer screen. [98] [100] [99]

2 Experimental Procedures

2.1 Materials

GQD-CB were prepared from Vulcan CX-72 carbon black (Cabot Corporation). Dimyristoylphosphatidylcholine (DMPC) was obtained from Tokyo Chemical Industry Co. (Toshima, Japan). Ethanol were purchased from Merk (Darmstadt, Germany). All other chemicals were acquired to Sigma-Aldrich and were used with no further purification. The fluorescent probes (±)-n-(9-anthroyloxy) stearic acid (n=3, and 12, named as n-AS probes) were purchased from Invitrogen-Molecular Probes (Paisley, UK) and all were used as supplied. Stock solutions of DMPC and of the fluorescent probes were prepared in ethanol. All the solutions were prepared with ultrapure Milli-Q water. All chemical reagents and solvents were of analytic grade or above.

2.2 Methods and instruments

2.2.1 Preparation of buffer solutions

Universal buffer solution was prepared according to the protocol described in [101] that allows to attain solutions ranging from pH 2 to 12. The recipe of universal buffer is as follows: dissolve in 1 L of ultrapure water - 21.01 g of citric acid (0.1 M), 13.61 g of potassium phosphate (0.1 M), 19.07 g sodium tetraborate (0.1 M), 12.1 g of Tris (0.1 M), 7.46 g of potassium chloride (0.1 M). 11 different buffer solutions were obtained from 3 previously prepared universal buffer solutions with pH=3.03, pH=7.76 and pH=8.25. Buffer solutions were filtered with 0.45 µm porosity filters, diluted and pH values were adjusted with the addition of NaOH (1 M) and HCl (1 M) until the following pH values were reached: 1.3, 3.0, 4.1, 5.2, 6.0, 7.0, 8.0, 9.0, 10.0, 10.8 and 11.5. The pH value was measured with an electrode system (glass electrode and Ag/AgCl reference electrode) calibrated by the Gran method, with a strong acid/strong base titration.

2.2.2 GQD-CB

2.2.2.1 Synthesis of GQD-CB

GQD-CB were prepared from carbon black by chemical oxidation according to a previously reported method [24]. Briefly, 0.4 g of Vulcan CX-72 carbon black (Cabot Corporation) was refluxed in 200 mL of HNO_3 (6 M) for 24 h. The suspension was left to cool to room temperature followed by a rest period of

at least 10 h to obtain a supernatant and a sediment. The supernatant was collected and heated at 120 ° C to evaporate the water and the nitric acid, which resulted in a reddish-brown solid.

2.2.2.2 Preparation GQD-CB suspensions at different pH values

To evaluate the effect of pH in the emissive properties of GQD-CB, different suspensions of GQD-CB at different pH values were prepared. In order to do that, an aliquot of GQD-CB was dissolved on 1.5 mL of each of the 11 buffer solutions prepared as previously described.

2.2.2.3 Size separation of GQD-CB by extrusion

GQD-CB aqueous suspension was prepared as described above. An aliquot of 1.5 mL of this GQD-CB aqueous suspension containing a wide variety of nanoparticles sizes was sequentially extruded at room temperature through polycarbonate membrane filters (Nucleopore membrane filters, VWR, Portugal) of decreasing pore sizes of 400 nm, 200 nm, 100 nm and 50 nm (10 passages each) using a 10 mL Lipex™ extruder (Northern Lipids, CDN-Burnaby) at 6-8 bar. For the sake of clarity the GQD-CB size separated by extrusion will be referred in the text as GQD-CBext.

2.2.2.4 Measurement of GQD-CB and GQD-CBext fluorescence

The steady-state fluorescence measurements were performed in a Horiba Jobin Yvon Spex Fluorolog-3 spectrofluorometer. For each pH solution the emission spectra of GQD-CB was taken for a range of λ from 460 nm to 685 nm. The excitation λ was varied from 350 nm to 450 nm in steps of 10 nm. Acquisition of the emission spectra was made using a low scanning speed and integration time of 1s. The emission spectra of GQD-CBext was made in the same way as described for the GQD-CB, but the measurements were made in aqueous suspensions of GQD-CBext at each step of extrusion.

2.2.2.5 Evaluation of surface charge and size of GQD-CB and GQD-CBext

The Malvern ZetaSizer Nano ZS particle analyser was used to evaluate the average diameter (nm) of the nanoparticles by DLS using cumulants' analysis and to evaluate the nanoparticles' surface charge by determining zeta potential (mV) by ELS. To measure the mean diameter by DLS, 1 mL of each of the GQD suspensions prepared in different pH buffered solutions was taken and placed into a 3 mL disposable polystyrene cuvette. To measure ζ-potential of the GQD-CB suspensions prepared in

different pH buffered solutions by ELS, 0.7 mL of the GQD-CB suspensions were transferred into a disposable polystyrene cuvette in which it was placed the universal dip cell. Malvern Dispersion Technology Software® (DTS) was used for a thorough analysis of the results obtained either from the determination of the average diameter (nm) of the nanoparticles (analysed in terms of intensity distribution and number distribution) or from the determination of the mean ζ-potential (mV) and associated standard deviation error.

In the case of GQD-CBext aqueous suspensions, size and surface charge evaluation procedure were the same as descripted above and were made in each step of extrusion: with no filter and after the extrusion trough each filter of different pore size (400 nm, 200 nm, 100 nm and 50 nm).

2.2.3 GQD-CVD

2.2.3.1 Synthesis of GQD-CVD

The CVD graphene used in this experiment was grown on top of 25 μm copper foils (Alfa Aesar, 99.999 % purity). The copper foil was introduced into a hot walls furnace of a thermal CVD system (EasyTube 3000EXT) and annealed at 1020°C for 20 min. in 0.5 Torr hydrogen atmosphere, in order to clean the surface from copper oxides and promote copper grain growth. After that, methane was introduced for 30 min. under a flow ratio H_2:CH_4 of 6:1 while keeping the same total pressure, to act as carbon source for the graphene growth.

Graphene was then transferred to a final substrate using the copper dissolution method. First, oxygen plasma is used to remove graphene from the bottom side of the copper foil. The other side of the copper is then spin-coated with poly (methyl-2-methylpropenoate) (PMMA, AR-P 679.04) at 1000 rpm, followed by a bake at 80 °C for 8 min. The copper foil was then dip into a $FeCl_3$ (0.5 M) solution until copper was entirely dissolved. The remaining graphene/PMMA membrane, floating in the solution, was then cleaned in an HCl (2%) solution to eliminate iron precipitates and follows to deionized water cleaning of the surface from HCl solution. At this step graphene could be transferred onto a final glass substrate. This glass substrate was previously cleaned with Acetone, isopropanol (IPA) and deionized water with Ultra sounds. After the graphene/PMMA membrane was transferred onto these substrate from the solution, the substrates were dried for 12 h at 120 °C in an oven to enhance graphene adhesion. The PMMA layer then was dissolved in acetone.

2.2.3.2 Analysis of GQD-CVD by confocal Raman microscopy

Raman scattering experiments of GQD-CVD were performed at room temperature (20 ºC) in a back scattering geometry on alpha300 R confocal Raman microscope (WITec). It was used a 1.5 mW

excitation 532 nm Nd:YAG laser, focused on the sample by a x50 lens (Zeiss). The spectra were firstly collected with a 600 groove per mm grating using 10 acquisitions with a 2 s acquisition time. In order to determine the peak positions and corresponding full-width at half-maximum (FWHM) Lorentzians were fitted to the vibrational bands in the Raman spectra. To obtain a more insightful result, it was taken a scan of a 30 µm x 30 µm area, reading 30 points per line in a total of 30 lines with an acquisition time of 1s.

2.2.3.3 SEM analysis of GQD-CVD

GQD-CVD were taken out from the glass substrate with a double-sided conductive adhesive tape and mounted on a sample stub. Analysis was made in a Phenom ProX desktop scanning electron microscope with an acceleration voltage of 5 kV, in charge reduction mode and a backscatter detection. 111 µm x 111 µm and 16 µm x 16 µm SEM images were taken in a scale of 30 µm and 5 µm respectively.

2.2.3.4 Extraction of GQD-CVD from glass substrate

A piece of glass substrate containing GQD-CVD was immersed onto 5 mL of buffer solution of pH=9.0, prepared as described previously in 2.2.6.1 in a Falcon tube. The Falcon tube was then placed into an ultrasound sonication bath (Selecta) at 42 KHz frequency for a maximum of 2 h. After 15 min of sonication time, 2.5 mL were taken out of the solution for characterization by DLS and ELS. After 2 h of sonication time the remaining solution was also characterized.

2.2.3.5 Evaluation of surface charge and size of GQD-CVD extracted from glass substrate

The procedure to measure the zeta potential and the average diameter of GQD-CVD was the same as previously described in 2.2.2.5. The analysis was made using the clean buffer solution of pH 9.0, and using the buffer solution where the glass substrate containing GQD-CVD was immersed: after 15 minutes of sonication and after 2 hours of sonication exposure. For the sake of clarity the GQD-CVD extracted from the glass substrate will be referred simply as GQD-CVD.

2.2.3.6 Measurement of GQD-CVD UV-Vis absorbance

UV/Vis spectra of GQD-CVD were characterized by a UV/Vis spectrophotometer (Shimadzu UV-Vis-NIR). Briefly, a baseline was made using buffer solution of pH 9.0 in sample and reference cells.

Absorbance spectra were obtained replacing the buffer in sample cell by the buffer solution where the glass substrate containing GQD-CVD was immersed: after 15 minutes of sonication and after 2 hours of sonication exposure. Spectra were taken from 220 nm to 700 nm, at low scan speed and a slit of 2.0.

2.2.4 Liposomes

2.2.4.1 Preparation of liposomes labelled with fluorescent probes

Liposomes and labelled liposomes were prepared as previously reported [102]. Briefly, a lipid film was prepared by evaporation to dryness of a mixture of a DMPC ethanolic solution and a fluorescent probe ethanolic solution (*n*-antroyloxy stearic acid derivatives where *n*=3 or 12, briefly designated as 3AS and 12AS). The lipid:probe ratio was kept as 100:1 to prevent changes in the structure of the liposome and labelled liposomal suspensions were protected from light in every steps of their use. The resultant dried lipid film was dispersed with ultrapure water and the mixture was vortexed at 37 ºC to yield multilamellar vesicles. Lipid suspensions were then extruded under controlled temperature (37 ºC) through polycarbonate filters with a pore diameter of 100 nm to form large unilamellar vesicles (LUVs).

2.2.4.2 Incorporation of GQD into liposomes

A final volume of 10 mL suspension of DMPC LUVs labelled with 3AS or 12AS probe were divided into four tubes each containing 2 mL of labelled liposomal suspensions. One tube was kept as reference and to the other 3 tubes were added: (i) GQD-CVD, (ii) GQD-CB and (iii) GQD-CBext. The labelled liposomes were incubated with GQD at 37 ºC during 30 minutes in the dark.

2.2.4.3 Evaluation of GQD membrane location by fluorescence quenching studies

The membrane location of GQD was assessed by fluorescence quenching measurements using two antroyloxy stearic acids derivatives as fluorescence probes incorporated in DMPC liposomes (500 µM) at different depths. 3AS probe was used as the one reporting a location close to the headgroup region, while 12AS probe was used as the one reporting a deeper membrane location. Fluorescence spectra of the labelled liposomes without or with GQD were analysed in a Perkin-elmer LS50 spectrofluorometer. The emission spectra were taken using two different excitation wavelengths: 360 nm (λexc maximum for the n-AS probes) and 450 nm (λexc maximum for GQD). Emission spectra ranged from 400 nm to 600 nm for λexc=360 nm and from 480 nm to 600 nm for λexc=450 nm. Spectra were measured at a low scan speed and with integration time of 1s.

2.2.5 DOX

2.2.5.1 *In silico* study

For the calculation of the molecular descriptors of DOX, the SMILES (Simplified Molecular Input-Input Line-Entry System) notation of the DOX molecule was first obtained in the Pubmed Compound online database (http: //pubchem.ncbi.nlm.nih.Gov/). The SMILES notation corresponds to a one-dimensional representation of the constitution and atomic organization of molecules, in which the isomeric representation includes information on the configuration of tetrahedral centers and geometry of double bonds. The SMILES notation can be translated into two-dimensional and three-dimensional representations of the corresponding molecules when specific software is used. Thus, using the SMILES notation and the Chemaxon® software with the MarvinSketch® module, we proceeded to design the chemical structure of the DOX molecule to its three-dimensional representation and the *in silico* calculation of several chemical descriptors such as ionization, pKa, electrical characteristics and surface topology.

2.2.5.2 Preparation of DOX stock solution and DOX standard calibration solutions in water

DOX stock solution of 6.21 x 10^{-4} M was prepared rigorously in a volumetric flask by dissolving 1.80 mg (weighed in a Sartorius microbalance) of DOX in 5 mL of ultrapure at room temperature. Different volumes of the stock solution (80 µL, 160 µL, 240 µL, 320 µL, 400 µL and 1200 µL) were rigorously measured with micropipette and added to Eppendorf tubes and ultrapure water was added to a final volume of 2 mL.

Final DOX standard calibration aqueous solutions presented the following concentrations: 2.48 x 10^{-5} M, 4.97 x 10^{-5} M, 7.45 x 10^{-5} M, 9.93 x 10^{-5} M, 1.24 x 10^{-4} M and 3.72 x 10^{-4} M.

2.2.5.3 Preparation of DOX stock solution and DOX standard calibration solutions in buffer of different pH values

Four DOX stock solution of 7.24 x 10^{-4} M; 5.17 x 10^{-4} M; 5.17 x 10^{-4} M and 4.83 x 10^{-4} M were prepared rigorously in a volumetric flask by dissolving 2.1 mg, 1.5 mg, 1.5 mg and 1.4 mg (weighed in a Sartorius microbalance) of DOX in 5 mL of buffer solution (respectively with pH=0.9, 4.7, 9.4 and 11.9) at room temperature. 6 dilutions were made for each pH, taking the same volume of DOX stock solution for Eppendorf tubes as previously described in 2.2.5.2, and adding each buffer solution to a final volume of 2 mL.

2.2.5.4 Measurement of DOX standard calibration solutions absorbance

UV/vis spectra of DOX standard calibration solutions were characterized by a UV/Vis spectrophotometer (Shimadzu UV-Vis-NIR). Briefly, a baseline was made using ultrapure water or each buffer solution of pH (pH=0.9, 4.7, 9.4 and 11.9) in sample and reference cells. Absorbance spectra were obtained replacing the ultrapure water or buffer in sample cell by the DOX standard calibration solutions. Spectra were taken starting with the least concentrated to the most concentrated DOX standard calibration solution with a wavelength range from 220 nm to 600 nm, at low scan speed and a slit of 2.0.

2.2.6 DOX and GQD Conjugates

2.2.6.1 Preparation of new buffer solutions

In order to limit the number of different compounds in solution, new buffer solutions were prepared to obtain 4 different pH values with the same acid and basic solutions as described by D.D. Perrin [101]. 500 mL of acid solution were obtained by mixing (50%:50%) dodecahydrated boric acid (0.2 M) and citric acid (0.05 M). 500 mL of basic solution were made by sodium phosphate (0.1 M). To obtain 100 mL of buffer solutions of pH 3, 6, 9 and 12, the Table 2 shows the respective volumes used of each acid and basic solutions.

Table 2 - Volumes of acid and basic mother-solutions to obtain 100 mL of buffer solutions.

≈ pH	Sodium phosphate (0.1 M) (mL)	Boric acid (0.2 M) + Citric acid (0.05 M) (mL)
3	12	88
6	41	59
9	65.5	34.5
11	78	22

2.2.6.2 Preparation of DOX-GQD-CB conjugates solutions at different pH values

DOX stock solution of 1.00 x 10^{-2} M was prepared rigorously in a volumetric flask by dissolving 29.20 mg (weighed in a Sartorius microbalance) of DOX in 5 mL of ultrapure at room temperature. For each pH buffer (pH 3, 6, 9 and 11) different volumes of the stock solution (100 µL, 120 µL, 140 µL, 160 µL) were rigorously measured with micropipette and added to Eppendorf tubes where the final volume of 2 mL was completed with buffer. 4 different concentrations of DOX (5x10^{-4}, 6x10^{-4}, 7x10^{-4}, 8x10^{-4} M) were obtained in each pH buffer.

16 samples of 1 mg of GQD-CB were weighed in small pieces of aluminium foil (Sartorius microbalance) and transferred to 2 mL Eppendorf tubes by washing the aluminium foil with ultrapure water. The samples of GQD-CB were then dried in a heating chamber (Memmert U40) at 100 ºC.

DOX-GQD-CB conjugates solutions were obtained by adding 1900 µL of each of the DOX solutions at 4 different concentrations ($5x10^{-4}$, $6x10^{-4}$, $7x10^{-4}$, $8x10^{-4}$ M) and at 4 different pH values (pH 3, 6, 9 and 11) to each Eppendorf tube containing 1 mg of GQD-CB (which results in 16 samples of DOX-GQD-CB conjugates). The resultant suspensions were vigorously mixed using vortex (Vórtex Genie ™ Scientific industries, Inc.) and sonicated for 5 min in ultrasound sonication bath (Selecta) at 42 KHz frequency.

2.2.6.3 Measurement of DOX-GQD-CB conjugates absorbance and fluorescence

After the preparation of 4 different concentrations of DOX ($5x10^{-4}$, $6x10^{-4}$, $7x10^{-4}$, $8x10^{-4}$ M) in each pH buffer (as described above), 100 µL of each DOX solution were diluted 20x with the respective buffer before measuring the absorbance and fluorescence spectra.

After mixing the remaining 1900 µL of DOX with the 1 mg GQD-CB samples (as described above), all the 16 conjugate DOX-GQD-CB samples were diluted 20x with the respective buffer before measuring the absorbance and fluorescence spectra.

The absorbance measurements were made as described in 2.2.3.6.

Fluorescence emission spectra were measured for samples prepared at pH 6 (expected as a pH where DOX and GQD-CB bind with great extension) at two different excitation wavelengths (λex): 450 nm (GQD-CB λex maximum) and 471 nm (DOX λex maximum). For λex = 450 nm the emission spectra were taken from 480 nm to 700 nm, and for λex = 471 nm the emission spectra were taken from 500 nm to 700 nm. All spectra were measured in a Perkin Elmer LS50 at a low scan speed and integration time of 1 s, with the maximum slit available (15.0 nm).

2.2.6.4 Analysis of DOX-GQD-CB conjugates by ATR-FTIR

The aqueous samples of DOX, GQD and DOX-GQD-CB conjugates prepared at pH 6 were placed in handmade aluminium foil pans and were dried in a heat chamber (Memmert U40) at 80 ºC to minimize the IR signal of water content. ATR FTIR absorption spectra were obtained within the wavenumber range 400–4000 cm^{-1} by means of Perkin Elmer spectrum uATR duo spectrometer in transmission mode.

The measuring signal passed the optical way with an aperture diameter of 10 µm with spectral resolution 4 cm^{-1}. For optimal signal-to-noise ratio, 64 scans were averaged per sample spectrum. The ATR technique is highly popular and yet introduces some distortions into spectra. Such distortions create

problems when comparing spectra obtained by ATR and transmission. Therefore, the Advanced ATR correction algorithm was applied to the spectra to correct for band intensity distortion, peak shifts, and non-polarization effects. Corrected spectra are highly comparable to their transmission equivalents.

3 Results and Discussion

3.1 Graphene oxide quantum dots (GQD)

3.1.1 Characterization of GQD prepared from carbon black by chemical oxidation (GQD-CB)

3.1.1.1 Optical characterization: Fluorescence of GQD-CB

The fluorescence emission of graphene oxide quantum dots (GQD) obtained from chemical oxidation of carbon black source (GQD-CB) was measured for eleven different pH values with excitation wavelengths varying between 350 nm and 450 nm in steps of 10 nm and at pH 5 (characteristic of cancer cells) with excitation wavelengths varying between 460 nm and 580 nm in steps of 20 nm. The variations of these parameters had the aim of checking the fluorescence emission behaviour of GQD-CB and its dependence on the excitation wavelength (λex) and pH.

For all the pH values assayed, the excitation wavelength that caused the highest emission intensities (λex_{max}) was 450 nm, which disagrees with the value of 320-370 nm reported for carbon dots (C-dots) and graphene dots (G-dots) [10]. However, for GQD the UV region of absorption and excitation of fluorescence has not been sufficiently well studied. There are several divergent results. This divergent results led to the suggestion of the presence of 'intrinsic' states with band levels of the carbon core groups coexisting with 'extrinsic' excited states formed by the functional groups on the surface edges with the energy levels between π and π* states of carbon core groups [103]. Furthermore, GQD prepared in a similar way as the ones presented here were reported to possess a λex_{max} of 460 nm.

At pH 5, for λex values higher than 460 nm, the maximum emission wavelength (λem_{max}) is clearly excitation dependent (Figure 19).nm [24]. In Figure 19 there is a red shift of approximately 100 nm from a λem_{max} of 535 nm to 635 nm when the λex changes from 460 to 580 nm, and the GQD-CB emit in the green region if λex is 460-520 and in the red region if λ_{ex} is 540-580 nm. This result is consistent with most reported studies of C-dots and G-dots that also describe a redshift of the λem_{max} [104] [14] [105] that has been attributed to the presence of intra-band heterogeneity. The origin of such spectral heterogeneity may result from structural variety of fluorescence emitters and of their in-particle interactions. Accordingly, shifting the excitation wavelength one can produce photoselection of species whose fluorescence is the brightest at this wavelength and such emission spectrum becomes wavelength-shifted [104] [14] [103]. Contrastingly, for most pH values, the λem_{max} is nearly excitation-independent when the λex changes in the range of [350-450] nm and GQD-CB emit in the green region (λem_{max} ≈ 523 -569 nm) with an average λem_{max} of 543 nm, which is consistent with the expected emission of carbon black dots produced by acidic oxidation [24] [105].

The only exception is the observed for pH 11.5, where a significant red shift of 40 nm occurs from a λem_{max} of 427 nm (emission in the blue region) to a λem_{max} of 527 nm (emission in the green region) when the λex changes respectively from 350 to 450 nm (Figure 20).

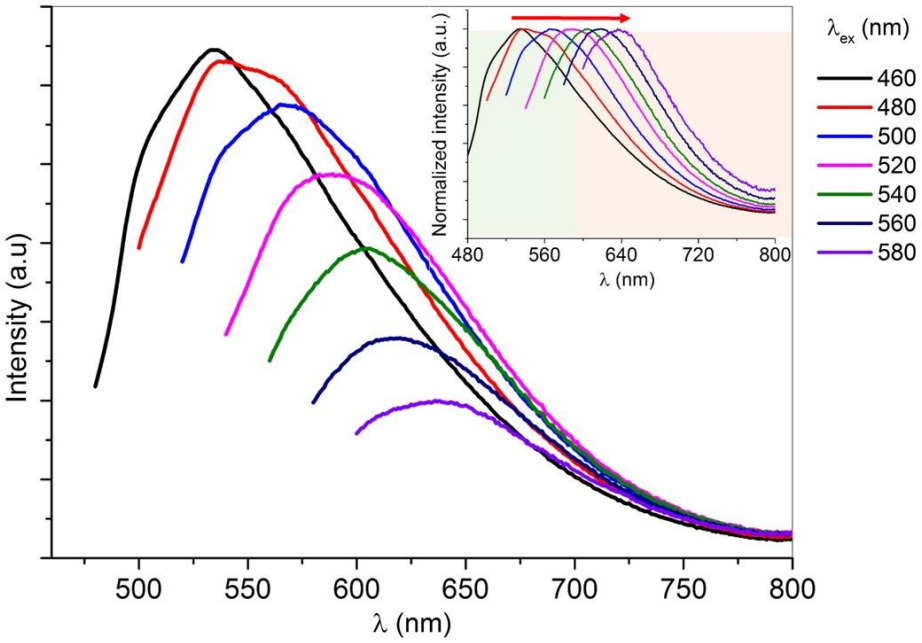

Figure 19 - Emission spectrum of GQD-CB at pH=5 for λex = [460-580] nm with increments of 20 nm. Inset: normalised spectra showing emission red shift with increment of λex. Green and red emission regions are represented by the two coloured blocks in the graphic.

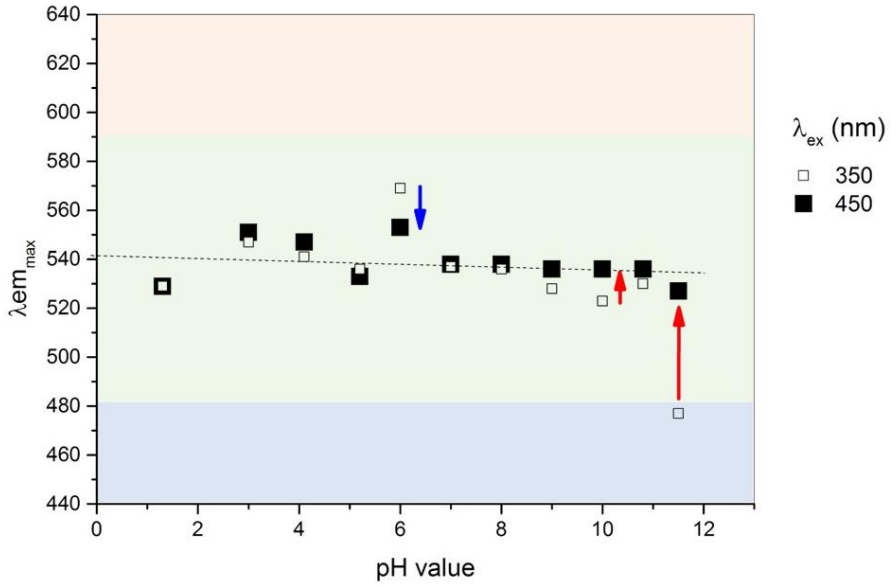

Figure 20 - Wavelength of maximum fluorescence emission (λem_{max}) of GQD-CB at different pH values (pH from 1.3 to 11.5) obtained when wavelength of fluorescence excitation (λex) was 350 or 450 nm. Blue, green and red emission regions are represented by the coloured blocks in the graphic. Arrows indicate a shift in the emission spectra with wavelength increase (red arrows= red shift and blue arrow =blue shift).

In order to see the spectra changes with pH in more detail, Figure 21 to Figure 24 show examples of the emission spectra of GQD-CB obtained at pH values of 1.3; 5.0; 6.0 and 11.5 with increasing λex from 350-450 nm.

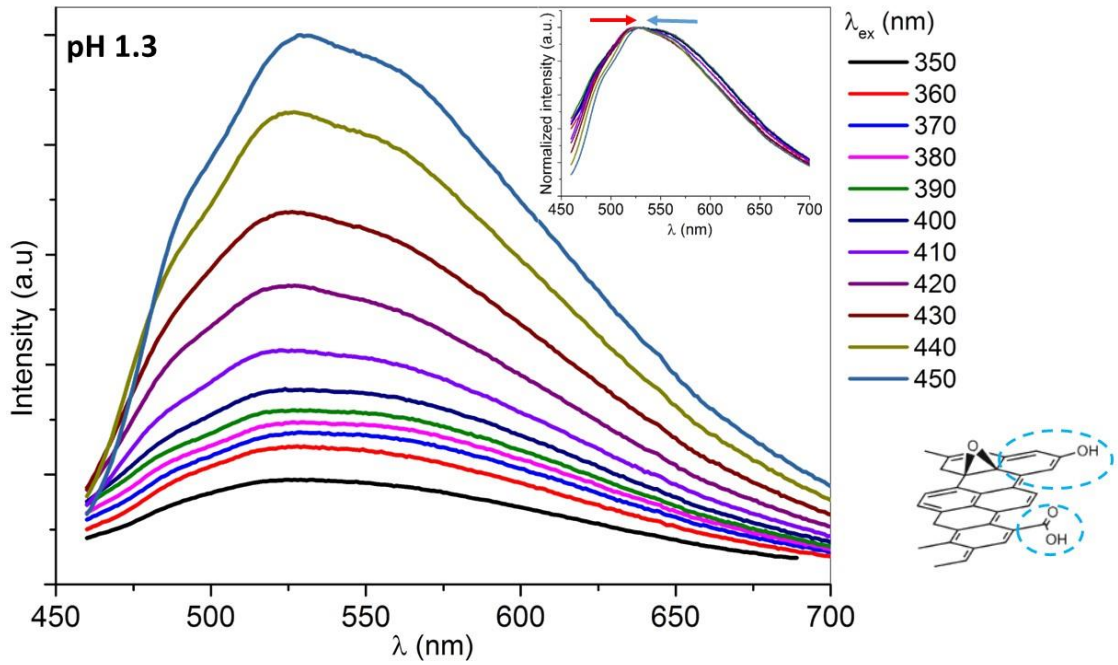

Figure 21 - Emission spectrum of GQD-CB at pH=1.3 for λex = [350-450] nm with increments of 10 nm. Inset: normalised spectra showing peak narrowing with increment of λex. On the right it is represented a structural model of GQD-CB showing its probable edge groups at this pH

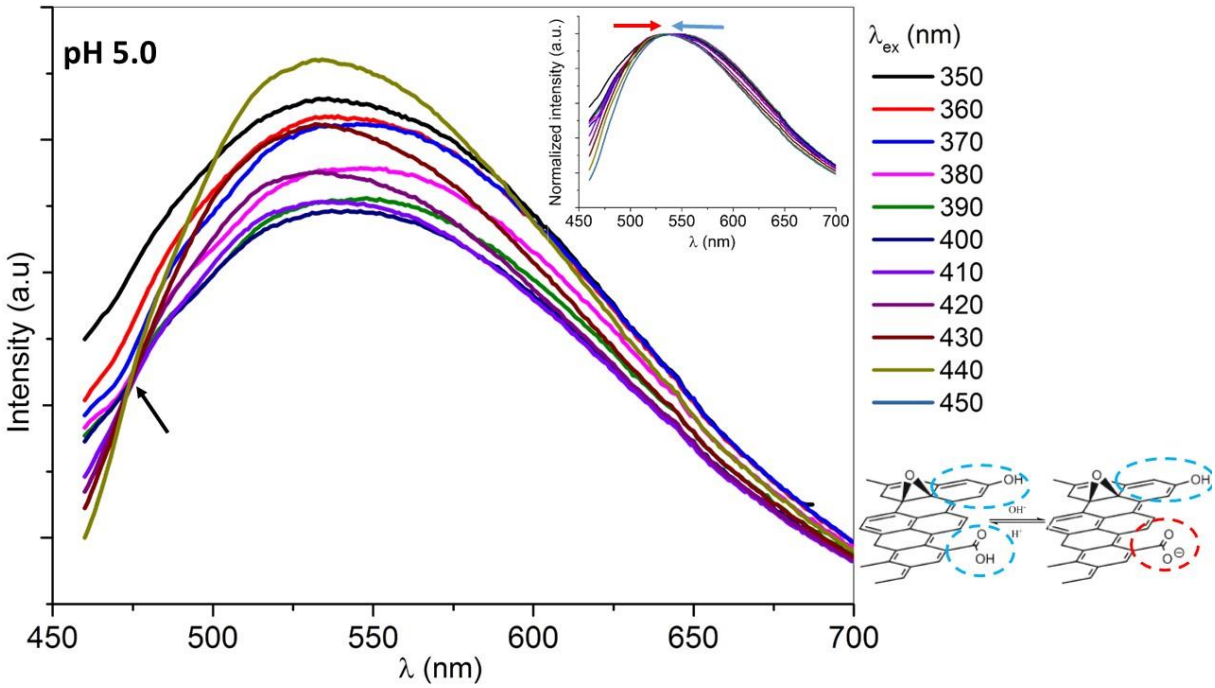

Figure 22 - Emission spectrum of GQD-CB at pH=5.0 for λex = [350-450] nm with increments of 10 nm. Inset: normalised spectra showing peak narrowing with increment of λex. Black arrow shows the existence of isosbestic point on the spectra. On the right it is represented a structural model of GQD-CB showing its probable edge groups at this pH.

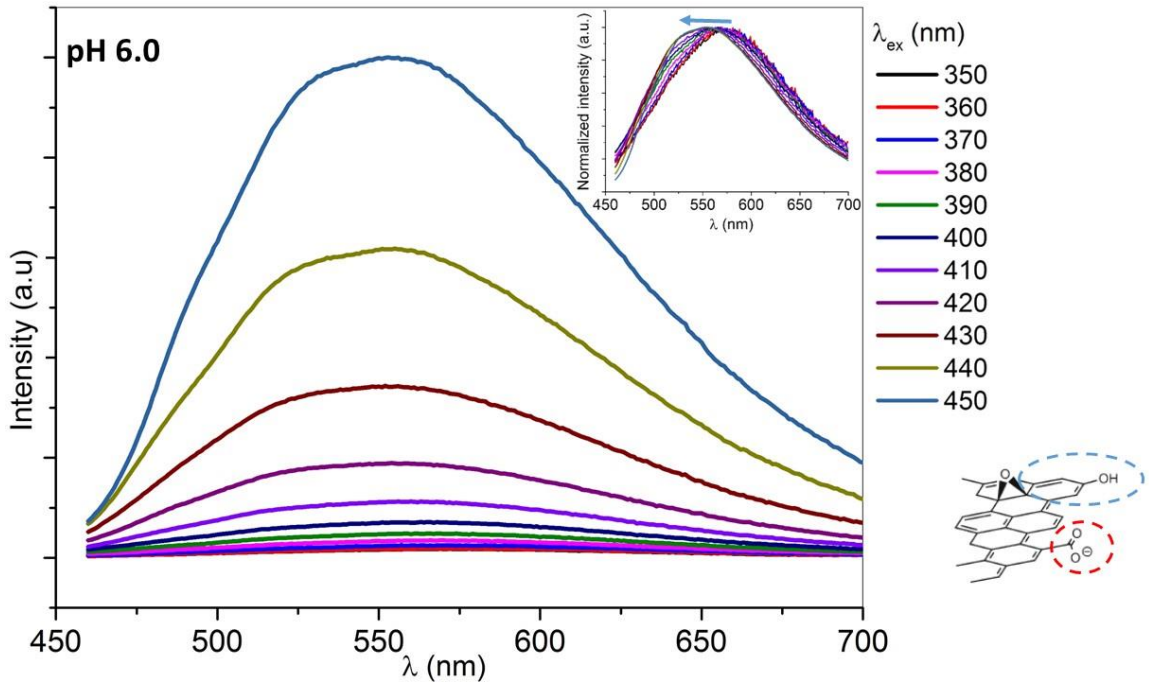

Figure 23 - Emission spectrum of GQD-CB at pH=6.0 for λex = [350-450] nm with increments of 10 nm. Inset: normalised spectra showing a blue shift of the peak with increment of λex. On the right it is represented a structural model of GQD-CB showing its probable edge groups at this pH.

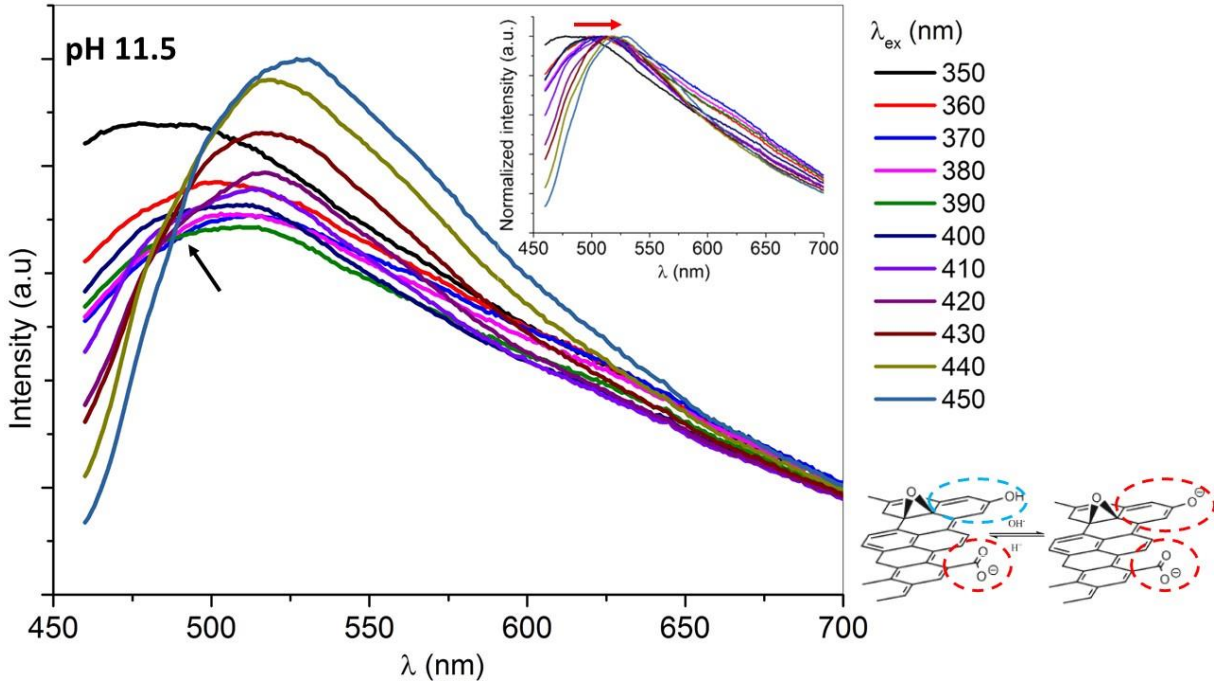

Figure 24 - Emission spectrum of GQD-CB at pH=11.5 for λex = [350-450] nm with increments of 10 nm. Inset: normalised spectra showing a red shift of the peak with increment of λex. Black arrow shows the existence of isosbestic point on the spectra. On the right it is represented a structural model of GQD-CB showing its probable edge groups at this pH.

The figures presented show that pH exerts a large effect in surface edge functional groups of GQD-CB and this is observable from their emission spectra. For pH 3 and 4 the emission spectra was similar to

the one of pH 1.3 presented in Figure 21, as an example. No isosbestic points could be observed in the spectra and the increment of λex does not translates in a significant change of λem_{max} and results only in a peak narrowing effect together with a significant emission intensity increase. Altogether these observations indicate that the GQD-CB possess their surface edge groups in a protonated neutral form of both the carboxyl and aromatic hydroxyl groups [106].

At a pH value (pH 5.0) close to the pH where carboxyl groups start to dissociate (pH > 4.5) [106], the emission spectra (Figure 22) presents an isobestic point indicating two types of emission spectra (one type obtained with excitations of 350-400 and the other type obtained with excitations 410-450) correspondent to two possible ionization states of GQD-CB. Nevertheless, the increment of λex does not translates in a significant change of λem_{max} and results only in a peak narrowing effect and changes in peak shape together with a emission intensity increase (less significant than the observed in the region of pH<5). Altogether these observations indicate that the GQD-CB possess a co-existence of a protonated neutral form (carboxyl and aromatic hydroxyl groups) and a negative form resultant from the dissociation of the carboxyl groups.

For pH 7.0, 8.0 and 9.0 the emission spectra was similar to the one of pH 6.0 presented in Figure 23, as an example. No isobestic points could be observed in the spectra and the increment of λex does not translates in a significant change of λem_{max} (results only in small blue shift in the case of pH 6), but the emission intensity increases significantly. Altogether these observations indicate that the GQD-CB possess their surface edge groups in only one form, and according to the pH values it must be the negative form resultant from the dissociation of the carboxyl groups [106].

For the more extreme basic pH values the emission spectra was similar to the one of pH 11.5 presented in Figure 24, as an example. The emission spectra (Figure 24) presents an isobestic point indicating two types of emission spectra (one type obtained with excitations of 350-400 and the other type obtained with excitations 410-450) correspondent to two possible ionization states of GQD-CB. The increment of λex translates in a red shift of λem_{max} (more significant to pH 11.5) and in peak shapes' change together with an emission intensity increase (less significant than the observed in the acid region, pH< 5 and in the neutral/basic region, 6<pH<9). Altogether these observations indicate that the GQD-CB possess at their surface edge groups with different ionizations: a co-existence of a negative form resultant from the dissociation of the carboxyl groups and a negative form resultant from the dissociation of the aromatic hydroxyl groups (that starts occurring at pH>8.8) [106].

3.1.1.2 Surface charge characterization: Zeta potential of GQD-CB

The variation of the zeta potentials of GQD-CB according to the pH values of the solvent media is shown in Figure 25 where it is observable a clear decrease on zeta potential with the increase of pH. Furthermore, the decrease of potential zeta values can be divided in three regions: (A) for pH values < 5.0 where the GQD-CB present constant and less negative values of zeta potential (<-10 mV) probably correspondent to the non-dissociated carboxyl groups and aromatic hydroxyl groups that are protonated

at this pH values; (B) for pH values between 5.0 and 8.0 where the GQD-CB present more negative values of zeta potential (between -10 mV and -20 mV) probably correspondent to the negative charge of carboxyl groups that start dissociating at pH 4.5; and (C) for pH values > 8.0 where the GQD-CB zeta potential values become steeply more negative (between -20 mV and -50 mV) probably correspondent to two negatively charged groups resultant from: (i) dissociation of carboxyl groups that starts at pH 4.5 and (ii) dissociation of aromatic hydroxyl groups that starts at pH 8.8. These results are in agreement with the reported pH dependence of graphite oxide studied by fluorescence [106]. Another conclusion that can be obtained by the variation of GQD-CB zeta potential values with pH is that GQD-CB are highly negatively charged at pH 7.4 characteristic of blood circulation and less negatively charged at acidic pH characteristic of cancer tissues and the differences between these two pH values are important in our desired triggering effect of GQD-CB – DOX complexes in acidic environments.

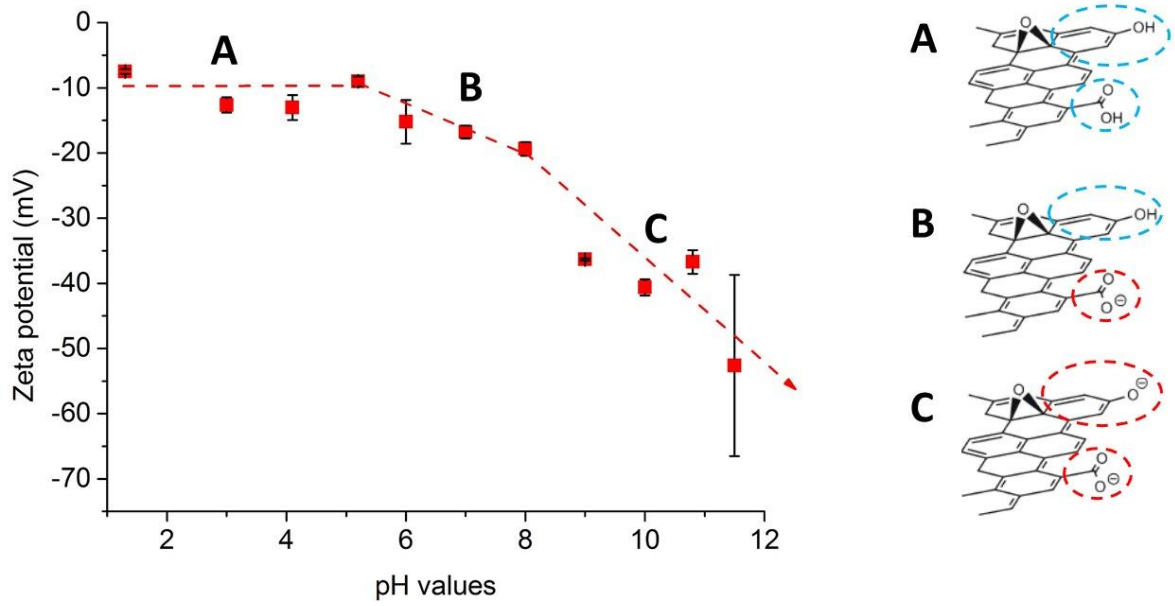

Figure 25 - Variation of zeta potential values (mV) of GQD-CB with pH. Regions A, B and C are defined according to the variation of zeta potential: (A) zeta-potential is almost constant; (B) zeta potential decreases, and (C) zeta-potential decreases more steeply. On the right are represented a structural model of GQD-CB showing its probable edge groups ionization at each pH.

3.1.1.3 Characterization of GQDext obtained after extrusion of GQD-CB

As previously stated in the optical characterization by fluorescent emission studies GQD-CB possess spectral heterogeneity that may result from structural variety of fluorescence emitters and of their in-particle interactions. Existing methods of preparation of carbonic nanostructures do not allow exclusion of this type of heterogeneity [103]. However, in order to produce well characterized DOX-GQD-CB conjugates, we should be able to control the size of such conjugates starting by regulating the GQD-CB size. A few methods were available in literature to propose the separation of CQD by sizes, e.g. using dialysis processes [106] [105], centrifugation and washing, [7] ultracentrifugation processes trough centrifugal filter devices [24] and filtration [107].

Herein we propose a different method to separate the CQD-CB by sizes based on pressure-extrusion (6-8 bar) through polycarbonate membrane filters of decreasing pore sizes of 400 nm, 200 nm, 100 nm and 50 nm (2 passages at first, and 1 for each of the others). At each step of the extrusion process a sample was taken and its optical properties were characterized by measuring its fluorescence emission spectra while its size and surface charge properties were characterized by DLS and ELS to determine their average diameter (nm) and zeta potential (mV) (Figure 26).

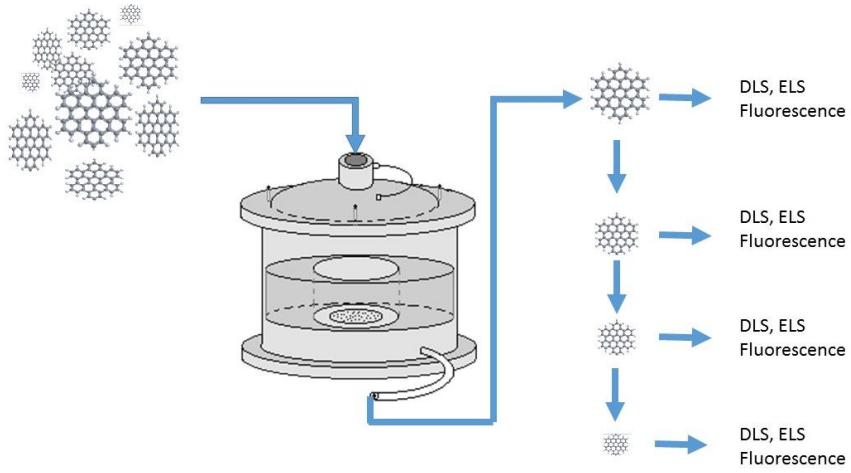

Figure 26 - Extrusion procedure for the separation of GQD-CB by sizes, using consecutively reduced pore filters of 400 nm, 200 nm 100 nm and 50 nm.

As it is possible to see in Figure 27 (A) there was a decrease on the size of the GQD-CBext gradually obtained by the decrease of the filter pores. The average sizes obtained are not exactly the filter pore sizes used as a certain pore size only allows the passage of CQD-CB that have sizes inferior to the pore. In Figure 27 it is also possible to observe that there was no change on zeta potential values during the extrusion process (A) and no change on the fluorescence emission spectra of the GQDext (B).

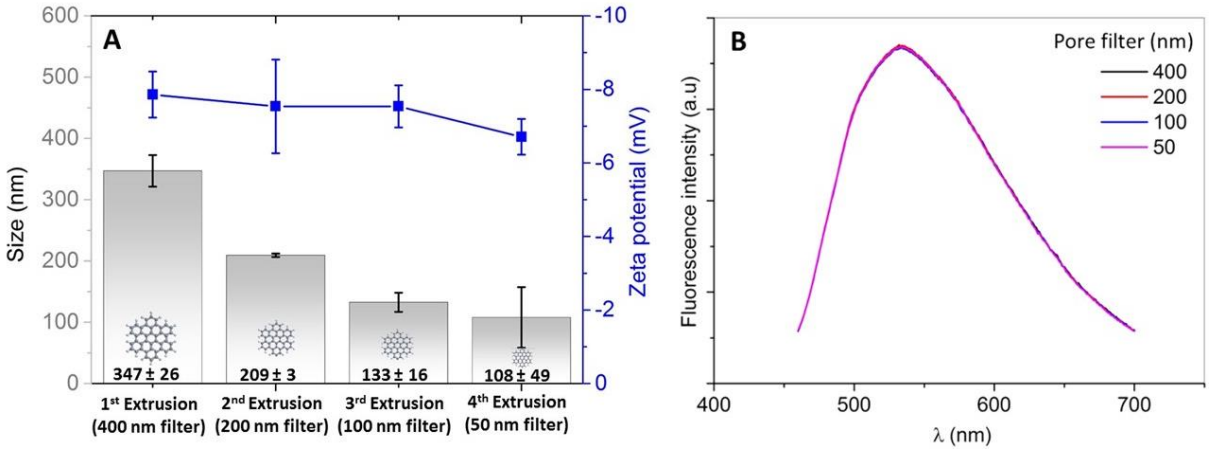

Figure 27 - (A) DLS and ELS characterization of GQDext. Size(nm) and zeta-potential (mV) measured for GQD-CBext obtained by extrusion, using consecutively filters of 400 nm, 200 nm 100 nm and 50 nm pores. Error bars correspond to STD of three measurements. (B) Fluorescence characterization of GQDext.

According to the above shown results, this method seems to be efficient and the closest to an accurate process for us to obtain size-controlled GQDext. However, we should make more assays to confirm the efficiency of the method and Atomic force microscopy (AFM) measurements are planned for a more thorough characterization of GQDext sizes.

3.1.2 Characterization of GQD prepared from chemical vapour deposition (GQD-CVD)

Since chemical vapour deposition is one of the most efficient methods to obtain graphene sheets with high purity we have tried to obtain graphene quantum dots using this method. The deposition occurred at the two faces of a Cu sheet, being one of them coated by a graphene monolayer and the other covered with imperfect graphene clusters. We retained the last one is a glass final substrate after graphene transfer.

To check if there was actually graphene on the glass substrate, two microscopy based characterization techniques were applied: confocal microscopy Raman and SEM. In a first approach we checked in the optical microscope the transparency of our sample (Figure 28) and then we swept an area of 30 µm x 30 µm with a confocal Raman microscope.

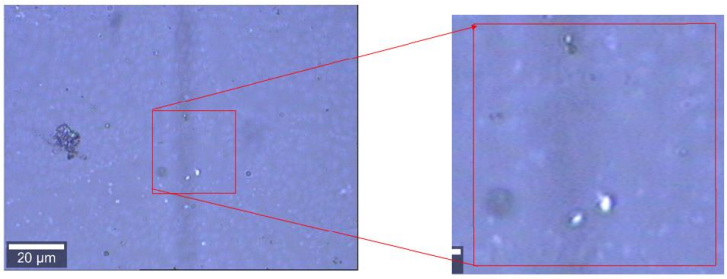

Figure 28 - Optical image of graphene clusters on glass substrate. Graphene was obtained by CVD at INL.

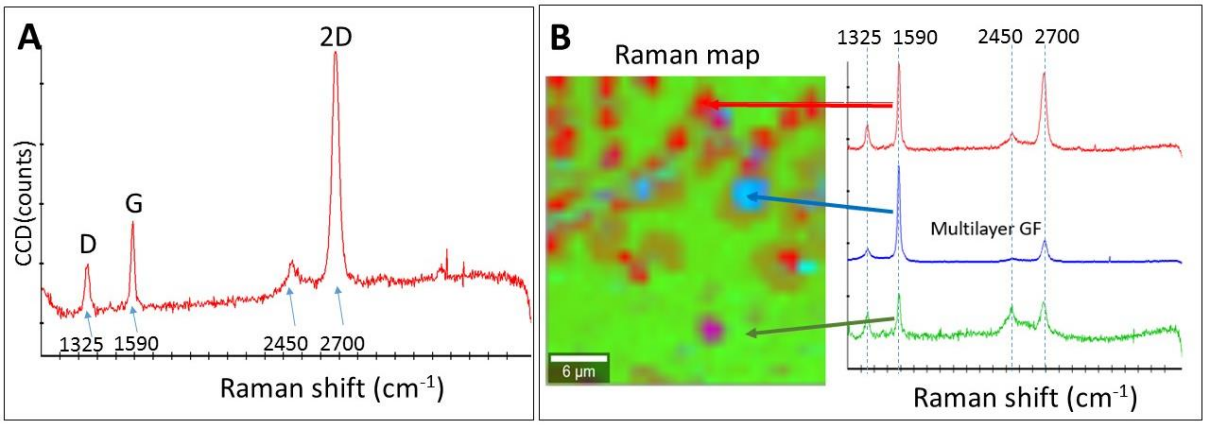

Figure 29 - (A) Typical Raman spectrum of graphene sheets. (B) Raman map and spectra of graphene clusters and GQD-CVD in glass substrate. Spectra: red – monolayer graphene spots; blue – multilayer graphene clusters; green – noise, no signal.

Figure 29 (A) shows the typical Raman spectrum of graphene sheets and Figure 29 (B) shows the Raman map of the GQD-CVD and the Raman spectra obtained for three sample spots.

On Figure 29 (A), the 2D band represents the number of carbon layers. The biggest the peak, the less the number of layers. Graphene monolayer samples should have great 2D peaks. The D band represents the presence of sp3 carbon defects as dangling carbon bonds in the termination plane. G band is due to the in-plane vibration of sp2-bonded carbon. Comparing to graphite, the intensity ratio of D and G bands (I_D/I_G) of graphene dots should be higher, since they are more defective and have greater contributions of the edge states and peripheral effects.

Considering our sample, the colour map and respective spectra on Figure 29 (B), allow us to observe the presence of single and multilayer graphene as it was expected. The blue graph almost does not have the 2D peak, which means it refers to graphene agglomerates or multilayers, whereas the red spectrum has the 2D peak at ≈2700 cm^{-1} showing a one layer structure. In both cases the typical G and D band of carbon bonds are seen at 1590 cm^{-1} and 1325 cm^{-1} respectively.

To confirm the results from Raman SEM images were taken on Figure 30. Once again it is possible to see a wide and random distribution of carbon clusters, with sizes from a few µm to nanometric sizes.

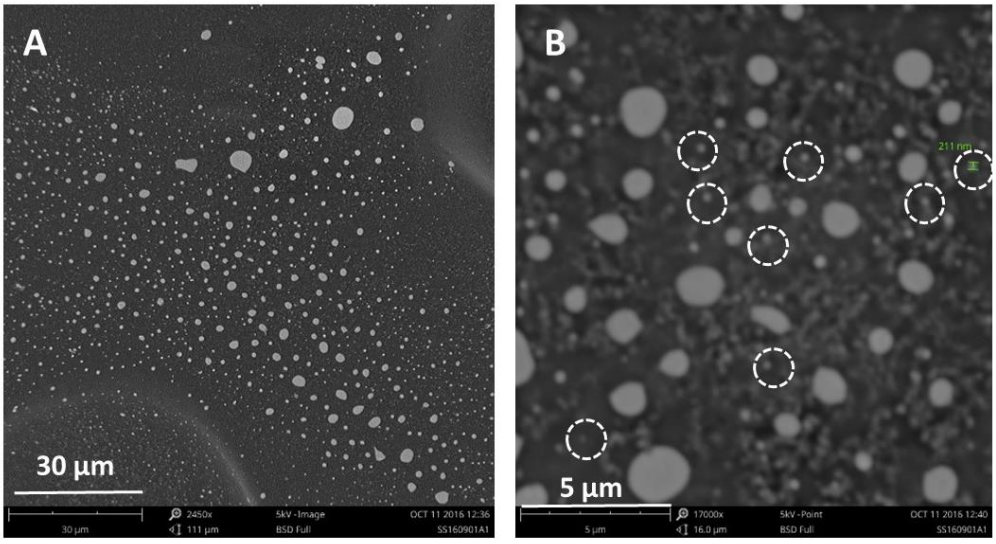

Figure 30 - A) SEM image of 111 µm x 111 µm with a 30 µm scale of GQD-CVD sample where micrometre clusters of graphene are visible. (B) SEM image of 16 µm x 16 µm with a 5 µm scale of GQD-CVD sample where micrometre clusters and GQD-CVD are observed. Dotted circles show GQD-CVD with about 200 nm size.

3.1.2. Extraction of GQD-CVD from glass substrate

After producing GQD-CVD in a glass substrate the next challenge was finding a procedure to extract it from the substrate to a solvent so at the end we have a suspension of GQD-CVD that we could use in further assays. This challenge was even bigger considering the fact that there are no reported methods in the literature to achieve graphene substrate desorption. Therefore, we propose an extraction method

based on pH adjustment and sonication. Briefly, a piece of glass substrate containing GQD-CVD was immersed in a buffer solution of basic pH (pH =9.0). The aim of this pH control was to dissociate surface groups of graphene (COOH, and Phe-OH) in basic media, to reach a negatively charged surface. This will possibly increase graphene aqueous solubility and favour repulsion between clusters of graphene, ultimately favouring its dispersion on the buffer media. To further improve graphene and GQD-CVD desorption from glass substrate, ultrasound sonication was also used.

To understand if this method was effective in extracting GQD-CVD from the glass substrate, we measured the zeta potential, size (Table 3) and the absorbance of the buffer solution at the beginning (sample 1 containing only buffer without glass substrate), and after immersing the glass substrate and performing 15 minutes of sonication (sample 2) and after 2 hours of sonication (sample 3). An important aspect observed is that with increasing time of sonication, the suspension kept translucent but became cloudier with an appearance characteristic of nanoparticles suspensions that are able to scatter light.

Table 3 - Zeta potential (mV) and average size (nm) of GQD-CVD extracted from glass substrate. Samples: 1) only buffer with pH=9; 2) Buffer solution after contact with glass substrate during 15 min and under sonication; 3) Buffer solution after contact with glass substrate during 2h and under sonication. Values correspond to Mean ± STD of at least 3 assays.

Sample	Zeta potential (mV)	Size (nm)
1 (Buffer pH 9)	-3.51 ± 0.24	170.03 ± 122.18
2 (Buffer pH 9 that was in contact with glass substrate after 15 min sonication)	-20.63 ± 1.54	225.40 ± 52.22
3 (Buffer pH 9 that was in contact with glass substrate after 2 h sonication)	-22.40 ± 1.12	433.10 ± 81.69

From Table 3 we see that there was an increase of the particles' size and a decrease on their zeta potential. This let to the conclusion that there were some particles being released from the glass surface that acquired negative charge on the basic pH. The buffer itself had some suspended particles that can be due to unsolubilized salts from buffer composition or to micro impurities. As the count rate of particles in buffer was very low and the error of the determination is high (in the same magnitude of the value of the size), we did not consider the values presented in buffer as being relevant or meaningful. Moreover for sample 2 and sample 3 there is significant increase of particles' size in the medium, which proves that particles are being released from the glass substrate. The zeta potential measurements confirm the GQD-CVD release, once that in comparison with the buffer (practically neutral) there is a great reduction in zeta potential to values close to the ones found for GQD-CB at pH 8.0.

The UV-Vis spectrum of the three samples was also measured. It has been reported that GQDs' UV absorption spectrum exhibits one broad band with a maximum at 228 nm and a shoulder at 300 nm which is typical for species where numerous transitions occur in parallel [106]. The shoulder at around 300 nm is typical for the n-π* transitions which invariably occur at about this wavelength, are rather weak in intensity, and result from the various kinds of carbonyl groups present. They easily undergo intersystem crossing to a triplet state and do not cause strong fluorescence in general. The maximum of 228 nm is assigned to the π-π* transitions [106]. These absorption bands are considered as typical

fingerprints of GQD and thus can be used to identify the presence of GQD in samples 2 and 3. Indeed, if we observe Figure 31 carefully, we can actually identify a 300 nm shoulder on both samples (at 303 nm on sample 2 and at 297 nm on sample 3) and a UV peak at 224 nm on sample 3.

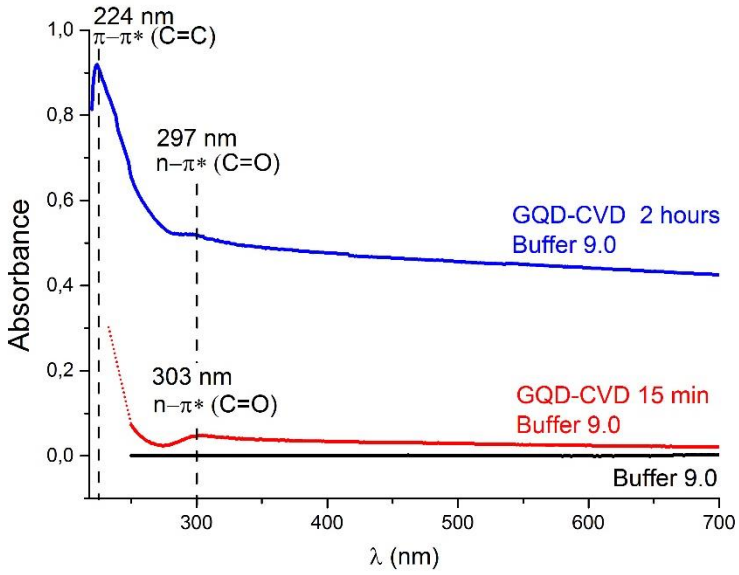

Figure 31 - UV-Vis Absorbance spectra of GQD-CVD extracted from glass substrate. Buffer 9.0 is the extraction solvent; GQD-CVD 15 min is the extracted suspension after 15 min in contact with glass substrate under sonication; GQD-CVD 2 hours is the extracted suspension after 2 h in contact with glass substrate under sonication. The absorption peaks characteristic of GQD and the respective electronic transitions are identified.

To guarantee the efficiency of this method to extract graphene clusters and GQD-CVD from glass substrate several complementary characterization techniques would be required (e.g. analysis by TEM, AFM, FTIR and Raman). It would be essential to repeat this procedure with different glass pieces and control extraction times. However, this could have been a first good step towards the development of an extraction procedure of GQD-CVD from glass substrates.

3.1.3 GQD incorporation on liposomes

In order to study liposomes as drug delivery systems that may be able to carry GQDs-DOX conjugates we started to analyse the incorporation of carbon dots on this system. To do so, liposomes were labelled with two extrinsic probes that report for different localizations on lipidic bilayer of liposomes (Figure 32) and the membrane location of GQD was inferred by the quenching effect caused on the fluorescence of the probes in the presence of carbon dots. The probes used were two labelled phospholipids: 3AS and 12AS, where the fluorophore group is linked respectively to the third and twelfth carbon of the phospholipid hydrophobic tail. Therefore, after being inserted in the liposomal membrane, 3AS probe provides information about the peripheral region of liposomal membrane, whereas the 12AS probe provides information about deeper penetrations (Figure 32).

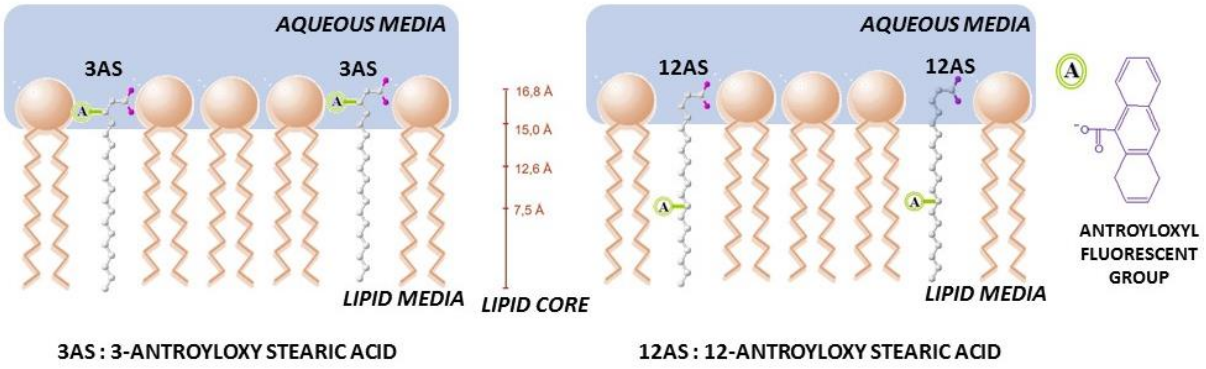

Figure 32 - Schematic representation of half of lipid bilayer and the location of the fluorescent group of 3AS probe and 12AS probe.

To analyse the quenching effect caused by the GQD we have prepared for each probe: (i) reference sample constituted by the liposomal model labelled with the probe; (ii) sample with the labelled liposomes incubated with GQD-CB, (iii) sample with the labelled liposomes incubated with GQDext (GQD filtered by extrusion); (iv) sample with the labelled liposomes incubated with GQD-CVD extracted from glass.

Ultimately, the idea behind this work is exciting the probes in their maximum excitation (λex of the probes = 360 nm) so they can exhibit a maximum emission at λem_{max} = 450 nm, which in turn is the λex of the GQD (Figure 33 A and Figure 34 A). Therefore if GQD and probes are close enough, exciting the probe at 360 nm, will cause energy transfer to the GQD and this will be visible in a quenching effect of the probe emission. i.e. the intensity of fluorescence emission is reduced (since part of the energy provided for excitation of the probe was transferred to GQDs and not all converted in emission) (Figure 33 B and Figure 34 B).

Figure 33 B and Figure 34 B evidence a maximum fluorescence of the probe intensity when it was excited at λex 360 nm as well as a clear emission quenching effect when in presence of GQD. The GQD-CVD extracted from glass substrate almost did not affect the probes intensity and the fluorescence emission spectrum of labelled liposome system containing GQD-CVD nearly overlapped the one of the labelled liposome system without dots. Therefore, even if there are GQD-CVD in the extracts they might not be in a sufficient concentration that perturbs the global probes' emission.

The extruded dots (GQD-CBext) clearly quenched the probe emission. As this was valid for both probes, it means that GQD-CBext were able to penetrate in the lipid membrane until the inner core, however there is a higher quenching of 3AS probe indicating a clear preference for a membrane location more close to the polar headgroup regions of the phospholipids. (Figure 33 B and Figure 34 B).

Non-filtered GQD-CB had the strongest quenching effect on the fluorescence of the probe and caused a significant redshift of about 15 nm from the maximum emission wavelength of the probe. These results confirm the energy transfer that occurs and indicate that CQD-CB are well incorporated at the lipid membrane level. The higher quenching efficiency by these unprocessed dots might be explained by

the fact that their concentration must be higher as the extrusion process retains some dots at the filters. Furthermore, the high density of dots from a wide variety of size may facilitate interaction with membranes and lipid membrane penetration.

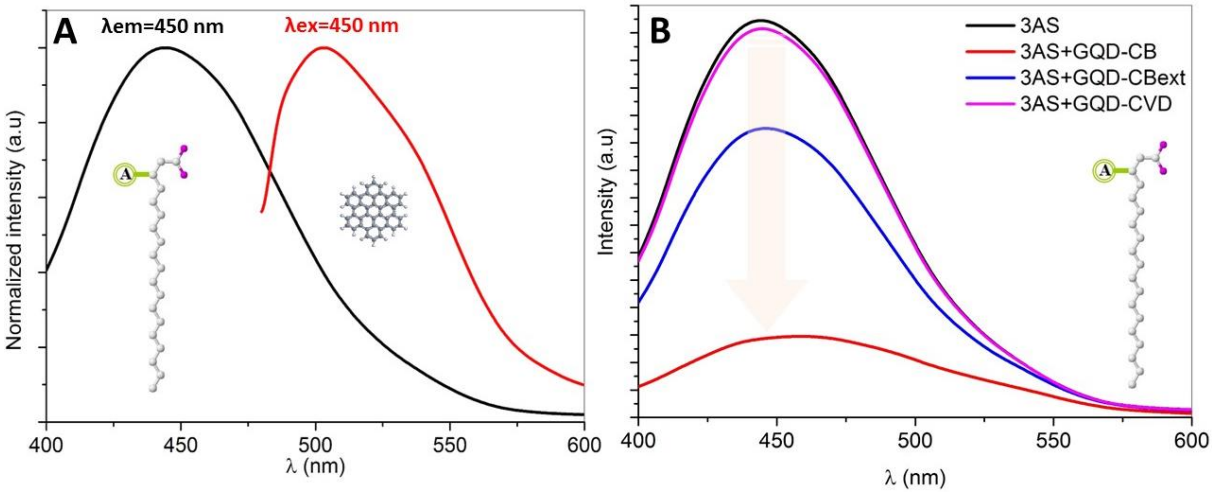

Figure 33 - (A) Normalized fluorescence emission spectra of 3AS probe obtained with λex of 360 nm and emission spectra of GQD obtained with λex of 450 nm. Since 3AS probe has a maximum emission at GQD excitation, if GQD and 3AS probe are close, energy is transferred from the probe emission to excite the dots resulting in probe fluorescence quenching. (B) Fluorescence quenching effect on the emission of 3AS probe (black spectrum) induced by GQD-CVD (pink spectrum); GQD-CBext (blue spectrum) and GQD-CB (red spectrum).

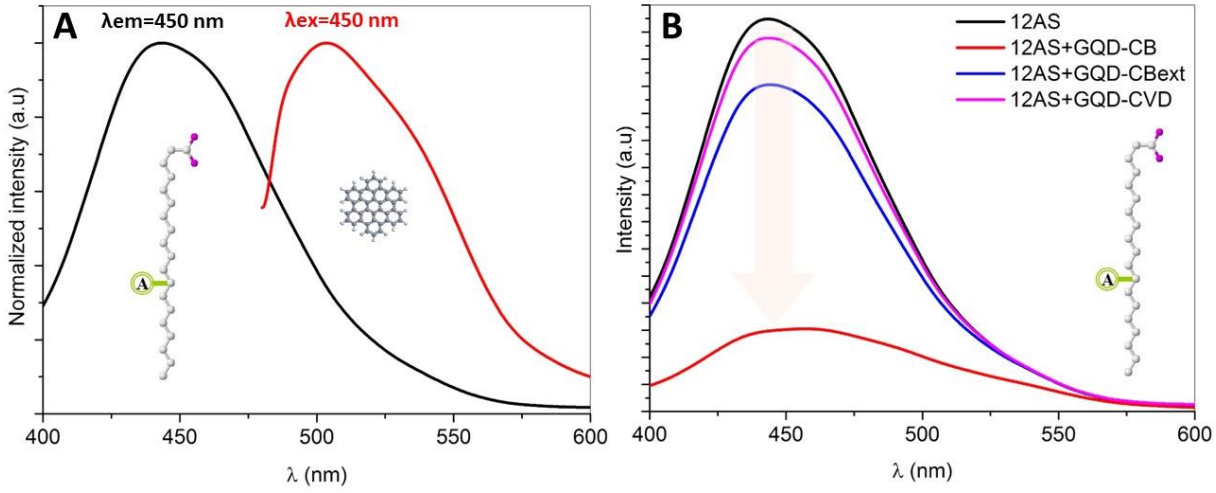

Figure 34 - (A) Normalized fluorescence emission spectra of 12AS probe obtained with λex of 360 nm and emission spectra of GQD obtained with λex of 450 nm. Since 12AS probe has a maximum emission at GQD excitation, if GQD and 12AS probe are close, energy is transferred from the probe emission to excite the dots resulting in probe fluorescence quenching. (B) Fluorescence quenching effect on the emission of 12AS probe (black spectrum) induced by GQD-CVD (pink spectrum); GQD-CBext (blue spectrum) and GQD-CB (red spectrum).

The comparison of the quenching effect of the different GQD incorporated in the lipid membranes is shown in Figure 35 for both 3AS and 12AS probes. To sum up, GQD-CVD were not very effective quenching the fluorescence of the probes, meaning that the particles were too big to penetrate into the

membrane, or that the extraction procedure was not effective to remove high concentration of GQD-CVD from the substrate. Unprocessed GQD-CB were the most effective quenching both probes with no apparent distinction meaning that they are able to penetrate the lipid membranes. Extruded GQD-CBext had a visible quenching effect and apparently with higher effect at the membrane headgroup regions.

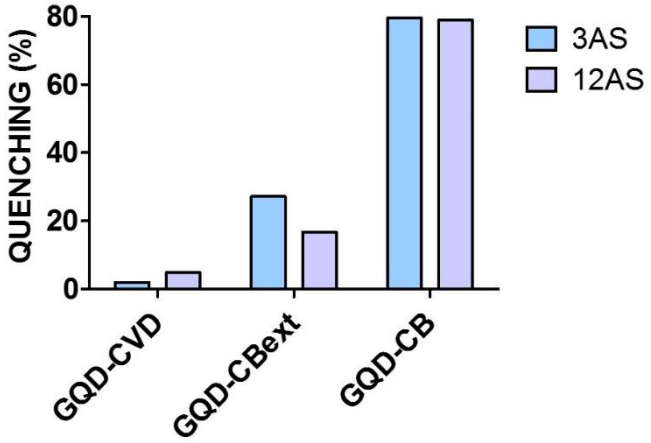

Figure 35 - Quenching of fluorescence emission (%) of the probes 3AS and 12AS (λex=360 nm) induced by the incorporation of GQD-CVD, GQD-CB and GQD-CBext in labelled lipid membranes.

3.2 Doxorrubicin (DOX)

3.2.1 *In silico* studies: DOX ionization and pH dependency

Using the software *Malvern Sketch*® it was possible to calculate DOX pKa values and predict DOX microspecies prevalent at different pH values. The hydroquinone and sugar groups of DOX are the most reactive, and easily ionisable with pH changes (Figure 36 and Figure 37).

The OH groups suffer deprotonation in alkaline pH values (becoming negatively charged: $R\text{-}O^-$), whereas NH_2 groups may suffer protonation in acid pH values (becoming positively charged: NH_3^+).

In alkaline and acid pH values NH_2 and OH groups, respectively, are not ionized. Figure 37 shows the detailed steps of DOX ionization with pH variation, being the represented species the most abundant at the mentioned pH ranges.

pKa values were calculated as the pH value where it was observed 50% coexistence of each of the two main species. This *in silico* study has revealed four values of pKa instead of the three reported experimental pKa values, which is understandable as the last theoretical pKa appears at an alkaline extreme of pH (≈14), being therefore difficult to determine it experimentally. The other theoretical pKa values predicted are in fair agreement with the ones reported and experimentally determined [51].

Figure 37 reveals the complexiy of DOX ionization process. This drug presents at least six species (A to F of Figure 37) that can occur depending on the pH of the meddium, and in some cases there is the

cohesistence of more than two species for the same pH range (e.g. at pH 8-9 and above 11) which turns the analysis of DOX interactions with other reactants much more complex.

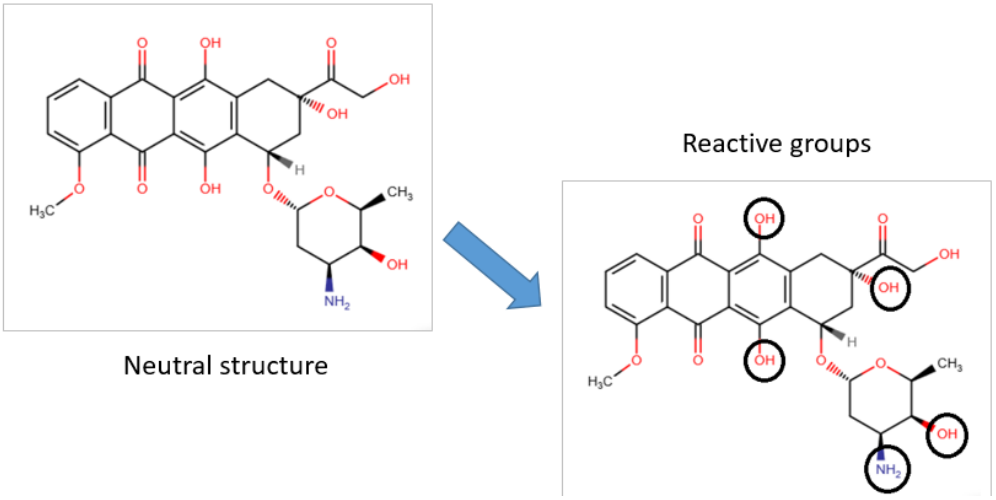

Figure 36 - Marvin Sketch® study of DOX properties. Representation of the neutral structure and main reactive groups of DOX.

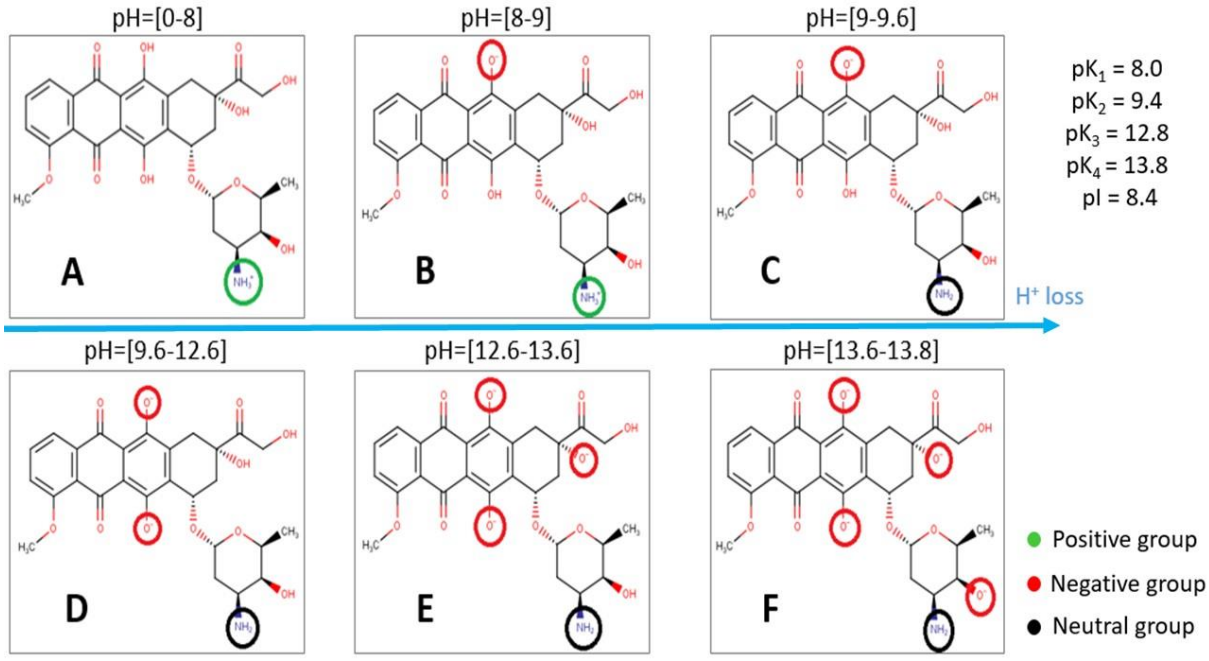

Figure 37 - Marvin Sketch® study of ionization of DOX reactive groups with pH.

3.2.2 DOX optical characterization: UV-vis absorbance

DOX absorption maxima occur at λ = 233 nm, 253 nm, 290 nm, 481 nm, 495 nm and 530 nm. The UV spectra shows characteristic peaks of extended conjugation of an aromatic nucleus. The broad peak starting at 420 nm is indicative of the highly conjugated anthraquinone moiety. This gives the compound

its red colour (Figure 38). On adding alkali (pH >9), the UV-Vis spectrum shifts towards longer wavelength due to the characteristic indicator-like properties of quinones. The colour change associated with this spectral shift is from orange-red to violet-blue (Figure 38).

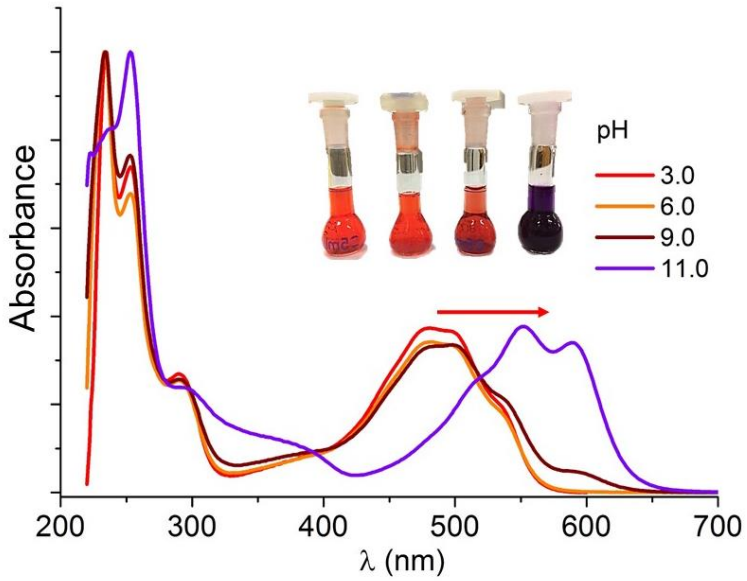

Figure 38 - DOX absorbance spectra at pH 3.0; 6.0; 9.0 and 11.0.
Photo: DOX coloured solution at the mentioned pH values under visible light. Red arrow indicates spectra red shift with pH increase.

Given the absorbance dependence of DOX with the pH several DOX standards with rigorous concentrations were prepared in buffer at different pH values: 3.0, 4.7, 6.0, 9.0 and 11.0. The UV-Vis absorbance spectra of the DOX standards was measured and the Molar extinction coefficient or Molar absorptivity (***ε*** in $Lmol^{-1}cm^{-1}$) was calculated.

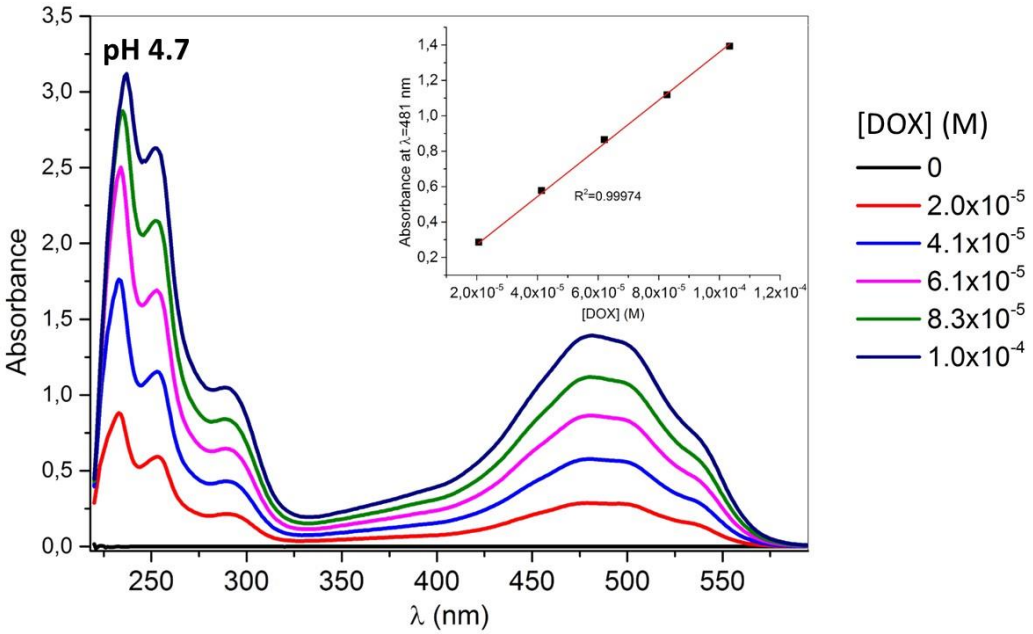

Figure 39 - DOX absorbance spectra of 5 standard solutions ($2x10^{-5}$ to $1x10^{-4}$ M) prepared in a buffered solution of pH 4.7. Inset: Beer Law linear plot for λ=481nm to obtain the molar absorptivity.

Figure 39 shows an example of DOX absorbance spectra and Beer Law linear plot used for the calculation of ε in $Lmol^{-1}cm^{-1}$ (slope of the linear plot presented). This process was repeated for the others pH values and Table 4 summarizes the values of ε and λ_{max} for all the pH values.

Regarding the stability of DOX solutions at different pH values, it was observed that all suffer a decrease on ε with time, showing the acidic solutions more stability than alkaline solutions, which are extremely unstable. In example: standard DOX solutions prepared at pH 4.7 were analysed 8 days later and a small reduction of 1% occurred in the recalculated ε; contrastingly, the pH 9.0 solutions were analysed after 6 days and a clear reduction of 19.71% occurred in the recalculated ε; in the case of pH 11.0, the solutions' instability occurs within hours after the preparation of the standard DOX solutions and the purple-coloured samples (Figure 38) lose their colour and become transparent.

Despite the differences observed in the ε with time, the wavelength of maximum absorbance does not change.

Table 4 - Molar absorptivity (ε in $Lmol^{-1}cm^{-1}$) and wavelengths where they were calculated for DOX at pH = 3.0, 4.7, 6.0, 9.0 and 11.0.

pH	ε_{DOX} ($Lmol^{-1}cm^{-1}$)	λ_{max} (nm)
3.0	10396	481
4.7	11450	482
6.0	10430	482
9.0	9426	498
11.0	7780	589

The accentuated instability effect of alkaline pH in DOX may be justified by the increasing protonation of the dihydroxyanthraquinone at alkaline solutions, fact that is referred to affect hugely the absorption spectrum [108]. In acidic solutions, the protonation occurs on the sugar moiety of DOX, being the dihydroxyanthraquinone neutral for most of the acidic pH range (Figure 37).

3.3 Conjugates of Graphene oxide quantum dots and doxorubicin (DOX-GQD-CB)

3.3.1 *In silico* studies of pH values where DOX-GQD-CB conjugates formation is favoured

Based on the *in silico* study of DOX and on the GQD-CB surface charge evaluation by measurement of zeta potential, Figure 40 shows a prediction of DOX-GQD-CB interaction according to pH variation. The experimental proof of this prediction has a paramount importance to conclude about DOX-GQD-CB adsorption and desorption conditions. In turn, this will be crucial for the effect of self-triggering and drug delivery by pH changes. Since the cancer cells are more acidic than the normal ones the drug release may occur due to that pH variation.

Analysis of Figure 40 indicates that in acid pH until 4.5-5.0, DOX is positively charged and GQD-CB are neutral, and thus an interaction between both is not expected. From pH 5.0 and 8.0, GQD-CB start to be more negative and DOX is still positive, promoting an adsorption between them. Within pH 8.0 and 9.0, GQD-CB increase their negative charge and DOX simultaneously has positive charges in $-NH_3^+$ group and $-O^-$ negative charges. Above pH 9, both DOX and GQD-CB are negatively charged through the deprotonation of OH groups and neutralization of $-NH_3^+$ group (DOX) and the appearance of more ionized edge groups, such as COO^- and Phe-O^- in the case of GQD-CB.

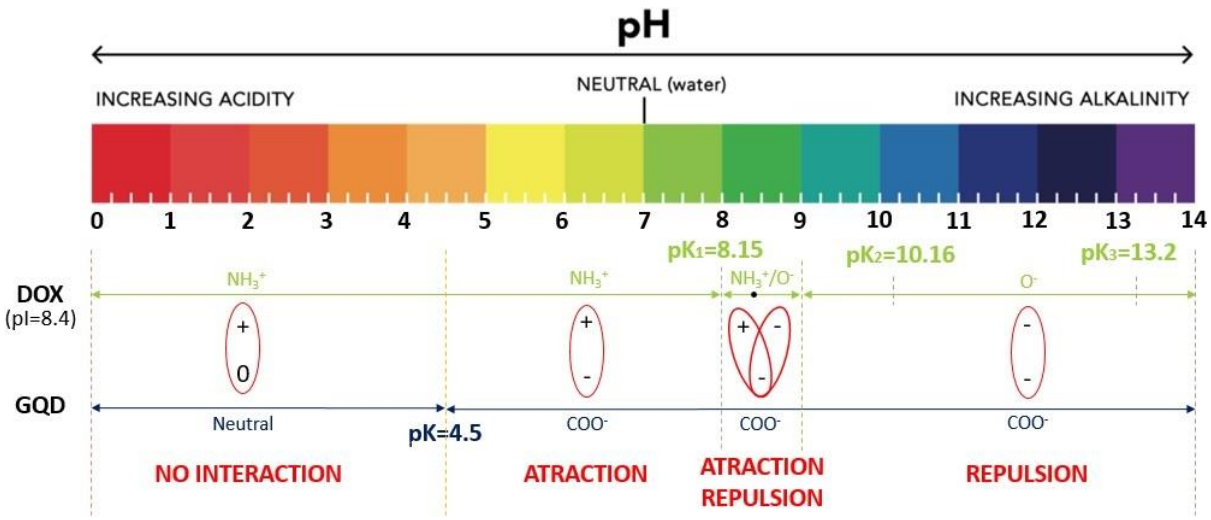

Figure 40 - Prediction of probable interaction between DOX and GQD-CB over pH variation.

In order to test the conjugates characteristics, four samples were prepared for each of the following pH values: 3.0, 6.0, 9.0 and 11.0. For each pH, 4 DOX concentrations were tested from 5 x 10^{-4} M to 8 x 10^{-4} M. Characterization of the conjugates formed was made by fluorescence and UV-Vis absorption studies and also by Raman and FTIR analysis.

3.3.2 Fluorescence characterization of DOX-GQD-CB conjugates

DOX adsorption by GQD-CB was assessed by fluorescence spectroscopy. The pH of the studies herein presented was pH 6.0, chosen as a pH value where DOX and GQD-CB conjugation is favoured. The analysed samples were free GQD-CB, free DOX at four different concentrations (2.5x10^{-5}-4x10^{-5} M) and conjugates of DOX and GQD (DOX-GQD-CB) prepared for all DOX concentrations. The measurements were taken at two excitation wavelengths: of GQD-CB (450 nm) and DOX (471 nm). This method afforded confirmation of the conjugates formation by the existence of energy transfer between the GQD-CB and DOX proving their close proximity. Figure 40 shows, as an example, what happened to the fluorescence emission of GQD-CB, DOX (at the maximum concentration tested 4.0 x 10^{-5} M) and the

correspondent DOX-GQD-CB when excited at λex = 450 nm (Figure 40 A) and when excited at λex = 471 nm (Figure 41 B).

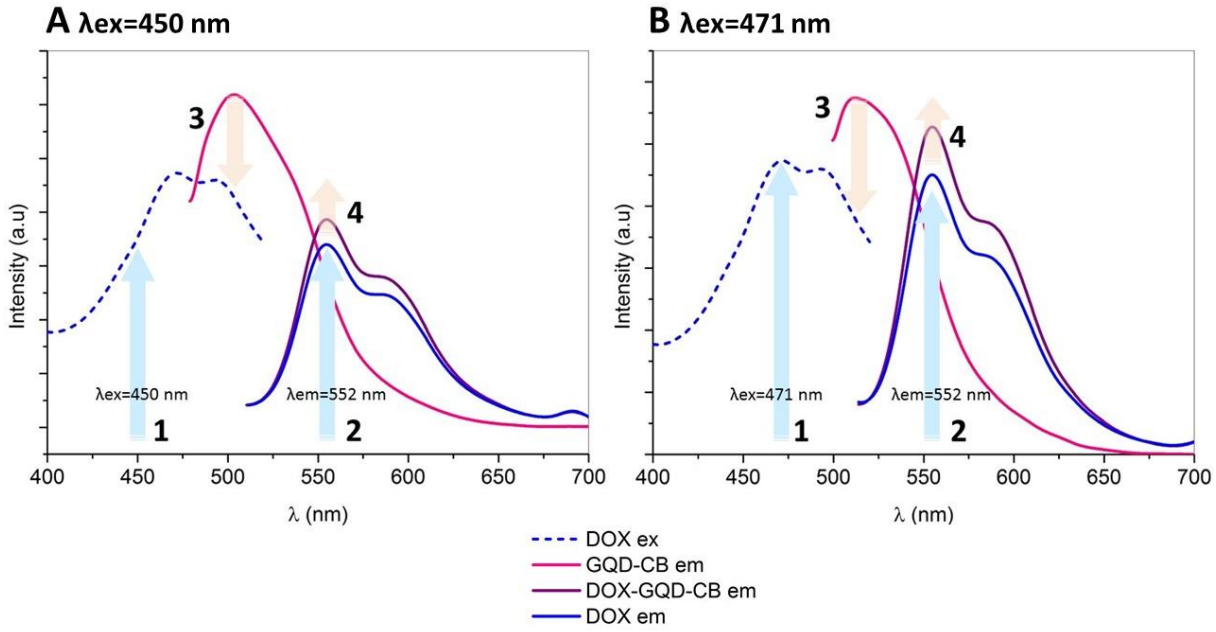

Figure 41 – Evaluation of fluorescence emission of DOX conjugates containing 4.0x10^{-5} M of DOX at pH 6.0 when λex = 450 nm (A) and λex = 471 nm (B). Figures represent steps of energy transfer process in conjugate formation: when excitation energy is provided, DOX and GQD-CB are both excited (1), and if they are close together, QGD-CB emission is transferred to DOX. As a result the emission spectra of QGD-CB-CB disappears (3) and the emission spectra of DOX (2) present in DOX-GQD-CB increases (4).

As it is possible to observe in Figure 41, there was a total energy transfer from GQD-CB to DOX, for both excitation wavelengths. When GQD-CB and DOX are close located in the conjugate, the spectrum of GQD-CB disappears, which means that the dots' emission energy was transferred to and absorbed by DOX and enhanced its final emission, as seen by the increase on the emitted fluorescence of the conjugates compared with DOX. The same process occurs for λex = 471 nm (Figure 41 B), but the emission intensity of DOX and conjugate samples (Figure 41 B) is higher than their emission intensity obtained at λex = 450 nm (Figure 41 A). This was expected since 471 nm is the maximum λex found for DOX. All the other three concentrations of DOX free samples and DOX-GQD-CB samples have similar behaviour as the described in Figure 41. There were no significant changes on fluorescence emission peaks and intensities due to DOX concentration variation. The fluorescence of GQD-CB totally disappeared in all samples. Besides, the excitation wavelength dependency always occurred as described above.

Regarding the emission bands of DOX and DOX-GQD-CB conjugates, no peak deviation was noticed and two maximums are presented at λem_{max} = 555 nm and 590 nm. However, the intensity ratio of these peaks has been used as a parameter probing the environment of DOX hydroxyanthraquinone-centered emitting state. Therefore from a ratio of 0.75 found for DOX free in water, the ratio slightly diminishes to 0.73 In DOX-GQD-CB conjugates and this decrease is another evidence of conjugate formation in agreement to what has been found upon conjugates formation between DOX and cyclodextrines [53].

Qiu, Jichuan et. al [107] also studied GQD and DOX conjugates by analysis of fluorescence emission spectra. In their case, upon excitation of GQDs-DOX conjugates at 400 nm and 499 nm they obtained respectively a spectrum with GQDs characteristic peaks (λem_{max} = 510 nm) and a spectrum with DOX characteristic peaks (λem_{max} = 550 nm and 590 nm). They also verified the energy transfer between DOX and GQD. Therefore, since we have tried to excite the DOX-GQD-CB conjugates both in the maximum excitation λ of DOX and in the maximum excitation λ of GQD-CB and in both cases the DOX-GQD-CB emission spectra was very similar to free DOX emission with no sign of GQD-CB emission this may imply that DOX is in excess towards GQD-CB.

3.3.3 Characterization of DOX-GQD-CB conjugates by UV-Vis absorbance

Similarly to what was done in fluorescence studies, the formation of conjugates DOX-GQD-CB resultant from DOX adsorption by GQD-CB was assessed by UV-Vis spectroscopy. Four pH values were considered (3, 6, 9 and 11) to understand if DOX and GQD-CB conjugation is affected by pH changes. The analysed samples were free GQD-CB, free DOX at four different concentrations (2.5×10^{-5} to 4×10^{-5} M) and conjugates of DOX and GQD (DOX-GQD-CB) prepared for all DOX concentrations.

Figure 42 shows the example of the absorbance spectra of all the samples at pH 6. For the other pH values the spectra obtained were very similar. DOX spectrum is consistent with the previously obtained presenting absorption bands in the visible region at 481 nm for pH 3, 482 nm for pH 6 and 498 nm and 589 nm for pH 9 and 11, respectively. The UV absorption bands of DOX are the same for all pH values: at 230 nm, 250 nm and 300 nm. All the DOX-GQD-CB conjugates at different pH values present a strong absorption band at 235 nm due to the contribution of both DOX (that presents an absorption band at 230 nm) and GQD-CB (that present an absorption band at the UV region at 228 nm [106]), this band is however red-shifted relatively to these contributions. This band has been assigned to π-π* transition and is bathochromically shifted (red-shifted) with the increase of solvent polarity and hydrogen-bonding [109] [110]. Therefore it is reasonable to assume that such shift can be attributed to hydrogen-bonding between DOX and GQD-CB. Also at 300 nm DOX-GQD-CB conjugates present an absorption band that must result from the contribution of DOX (that presents an absorption band at 300 nm) and GQD-CB (that present an absorption shoulder at this wavelength nm [106]). The absorption bands of DOX-GQD-CB conjugates at the visible region were apparently at the same position of the absorption bands of free DOX and became broader for all the conjugates spectra comparatively to the free DOX spectra measured at the same conditions.

To put in evidence the differences of absorption spectra obtained for GQD-CB, free DOX and conjugates DOX-CQD-CB in Figure 43 are presented the absorbance spectra obtained for pH 6 where the conjugate formation was expected to be favoured (Figure 43 A) and for pH 11 where the conjugate formation is hindered by surface charge repulsion between DOX and GQD-CB (Figure 43 B).

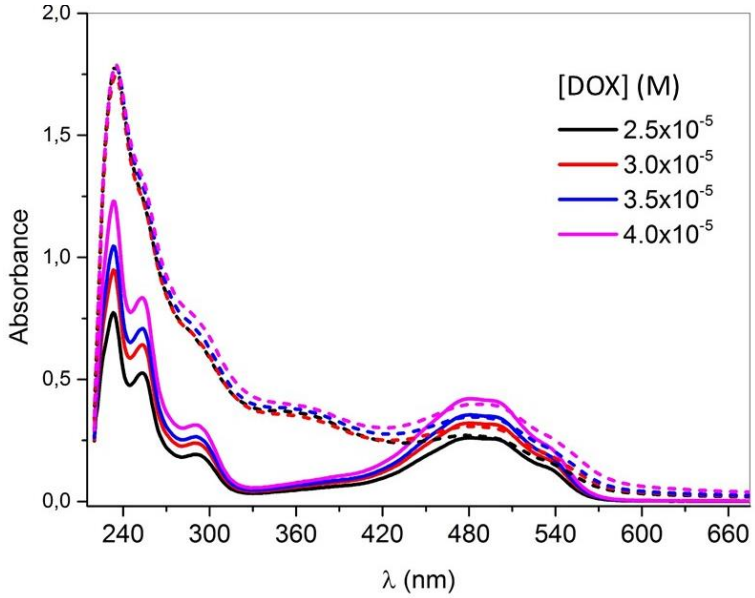

Figure 42 - Absorption spectra of free DOX (lines) and DOX-GQD-CB conjugates (dashes) at pH 6.

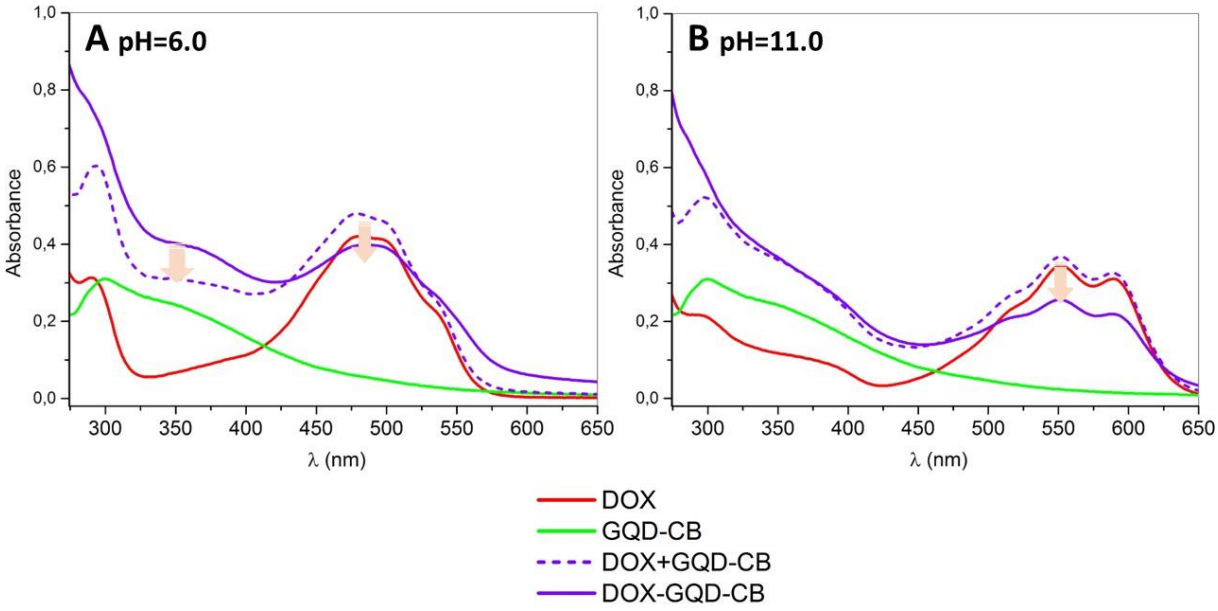

Figure 43 - Absorption spectra measured for free DOX, GQD-CB, DOX-GQD-CB (solid lines) and absorption spectra calculated by the sum of spectrum of DOX and GQD-CB (dashed lines) at pH 6.0 (A) and 11.0 (B) with a DOX concentration of 4.0x10^{-5} M.

It is known in absorbance spectroscopy that when the presence of one species in a sample does not influence the measurement of another species in the same sample; i.e., they do not interfere, thus, the absorption of light by the components of the sample solution is additive; that is, the total absorption of light at any given wavelength is just the sum of the absorbance that the two substances would show if measured individually under the same conditions [111]. In view to this, if DOX and GQD-CB were not conjugated, one would expect that the measured absorbance spectra of their mixture (represented in

Figure 43 as violet solid line DOX-GQD-CB) would be equal to their calculated additive absorbance spectra (represented in Figure 43 as violet dashed line DOX+GQD-CB). As it is possible to see, the DOX-GQD-CB and DOX+GQD-CB spectra are not coincident, meaning that there are conjugates in both pH values. However, two regions in DOX spectra can be distinguished. At pH 6.0, DOX-GQD-CB and DOX+GQD-CB spectra are not coincident neither in the UV region nor in the visible region, whereas at the pH 11.0, DOX-GQD-CB and DOX+GQD-CB spectra are coincident in the UV region and differ in the visible region. Probably what happens at pH 11.0 is that no hydrogen bonds and electrostatic interaction are established between DOX and GQD-CB (as they possess the same charge), but some π-π stacking interactions still occur, as these are not dependent on groups ionization. The stacking interaction influences the absorption spectrum of binding molecules, the absorption intensity of which decreases due to changes in electronic interactions between compounds. In literature this effect is known as hypochromism [112] [113] and is considered as a result of weak dipole–dipole interactions between stacking chromophores modified by the light wave.

The same comparative analysis was made for pH 3 and 9, and the differences between DOX-GQD-CB and DOX+GQD-CB spectra are higher at pH 9 than at pH 3, but smaller at pH 9 than at pH 6.0, meaning that the pH values that favour the conjugate's formation are the pH 6.0 and 9.0 confirming the theoretical interaction proposed by *in silico* studies.

By a detailed evaluation of the absorption bands at the visible region at all the pH values and for all the DOX concentrations, it was possible to gather the information presented in Table 5.

Table 5 - Maximum emission wavelength for free DOX and DOX-GQD-CB at pH from 3 to 11 with increasing DOX concentration. Red arrows show the red shift observed in absorbance spectra with the DOX concentration increase and blue arrows show the blue shift observed in absorbance spectra with addition of GQD-CB to DOX.

[DOX] (M)	λ_{max} (nm)							
	pH 3		pH 6		pH 9		pH 11	
	DOX	DOX-GQD-CB	DOX	DOX-GQD-CB	DOX	DOX-GQD-CB	DOX	DOX-GQD-CB
$2.5x10^{-5}$	481 (3 →)	478	482 (5 →)	477	498 (19 →)	479	589 (1 →)	588
$3.0x10^{-5}$		479 (2 ↓)		480 (7 ↓)		481 (7 ↓)		588
$3.5x10^{-5}$		480		482		482		588
$4.0x10^{-5}$		480		484		486		588

As mentioned above, DOX absorption bands did not suffer any shift within the same pH, despite of the increase of the concentration. However, the mixtures of GQD-CB with DOX (DOX-GQD-CB) were sensitive to the variation of concentration, suffering a red shift with the increase of the DOX concentration especially for pH 6 and 9. At the pH 11 this concentration-dependent shift was not observed. This could be another evidence of the DOX-GQD-CB conjugates formation by electrostatic interaction at pH 6 and 9, where there is supposed to be attraction between positive and negative charges from DOX and GQD-CB, respectively. At pH 3, the GQD-CB are supposed to be neutral and the DOX is positively charged, but there can be some GQD-CB ionized that justified the 2 nm redshift and a possible formation of conjugates. Finally, for pH 11 both the DOX and the GQD-CB are strongly

negative and thus there is no interaction and formation of DOX-GQD-CB complexes, which may justify the absence of redshift at this pH. On the other hand, at DOX smallest concentration, comparing DOX absorption band with the absorption band of the conjugates DOX-GQD-CB it is possible to conclude that the formation of conjugates occurs with a blue shift of the spectra. This is an indication of conjugate formation consistently observed in several reported studies between DOX and GQD [107] or DOX and ciclodextrins [53] or even in other conjugates [114] [115].

3.3.4 FTIR characterization of DOX-GQD-CB conjugates

FTIR spectra were normalized for the HO band (3365 cm^{-1}) for an easier comparison between spectra. As shown in Figure 44, DOX and GQD-CB have structural resemblance, with many common groups. Therefore, FTIR spectra of DOX, GQD-CB and conjugates DOX-GQD-CB are very similar. The FTIR spectra also shows that the edges of GQD-CB have many oxygen-containing groups that make GQD-CB more suitable for the adsorption of drugs like DOX through the role of hydrogen bonding. Therefore the weaker intensity bands found by conjugates of DOX-GQD-CB for 1715 and 1350 (-COOH), 1251, and 1065 (aromatic $–O^-$) and 1143 (aliphatic $–O^-$) cm^{-1} are indicative of hydrogen bonding to HO or $–NH_2$ groups of DOX (that appear both in DOX spectrum at 1574 cm^{-1} and in conjugates spectrum at 1575 cm^{-1}). Besides hydrogen bonding, the conjugates are established by π-π stacking interactions which is also visible by the reduction of the bands at 1580 cm^{-1} (attributed to aromatic C=C) of GQD-CB upon conjugation with DOX.

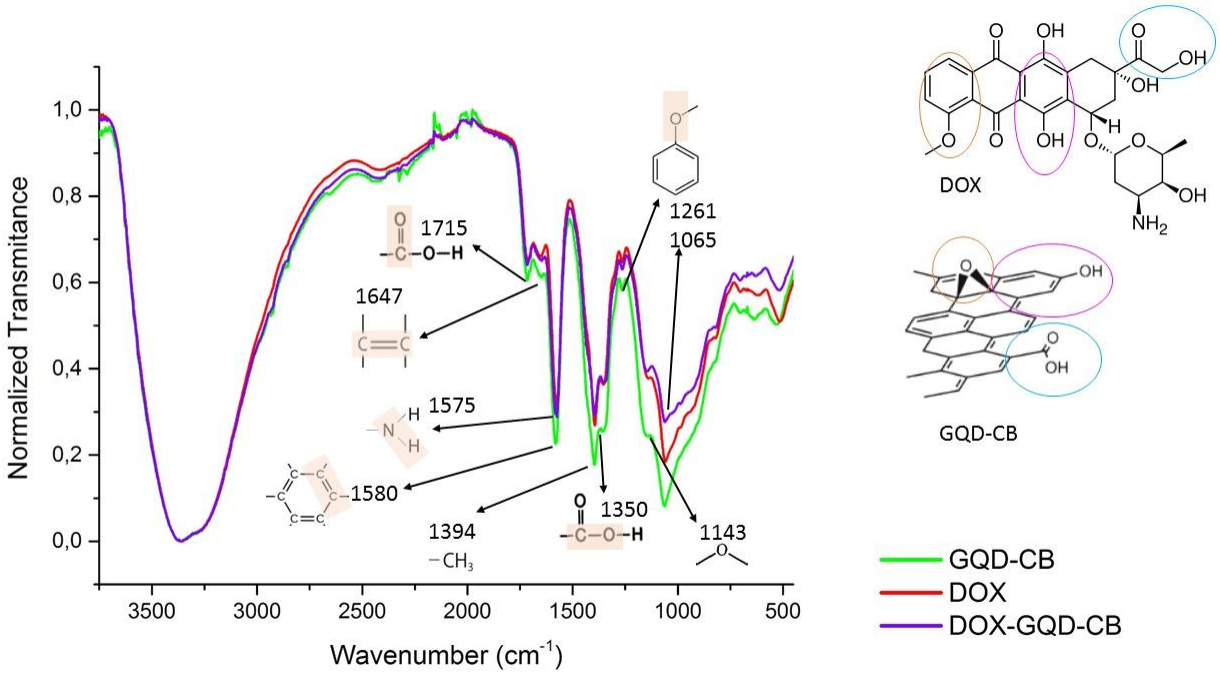

Figure 44 – Fourier transformed infrared spectra of GQD-CB, DOX and DOX-GQD-CB samples.

3.3.5 Confocal Raman

Raman spectroscopy was used to elucidate the chemical state of the graphene network of the GQD-CB, the chemical spectral fingerprint of DOX and finally the chemical structure of the conjugates DOX-GQD-CB and their Raman spectra in the range of 1000–2000 cm^{-1} are shown in Figure 45.

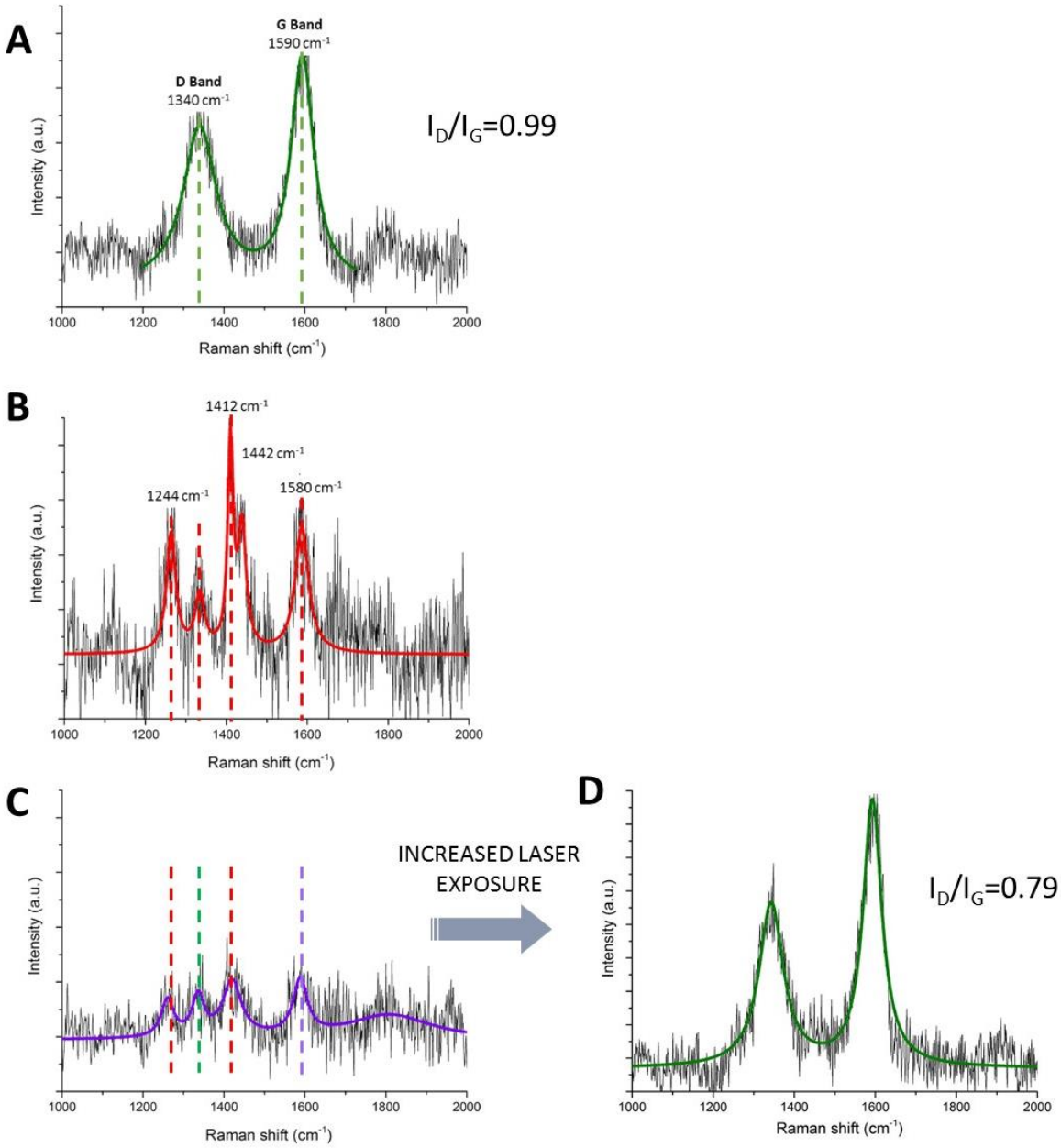

Figure 45 – Raman spectra of GQD-CB (A), DOX (B) and conjugates DOX-GQD-CB (C) at pH 6. (D) is the Raman spectrum obtained after exposing (C) to increased laser voltage. Peaks where fitted by Lorentzian function and fittings are displayed as green lines (A and D), red line (B) and violet line (C). In Figure C assignments of vibrational modes of DOX, GQD-CB or both are respectively identified by the red, green and violet dashed lines.

In good agreement with the literature [116] [117] [106] [105] Raman studies of GQD-CB show contributions from both the G band at 1590 cm^{-1}, related to in-plane vibration of sp2 bonded carbon atoms in a two-dimensional (2D) hexagonal lattice, and the D band at 1340 cm^{-1}, related to the presence of sp3 defects associated with the vibrations of carbon atoms with dangling bonds in the termination plane of disordered carbons (Figure 45A). The ~2700 cm^{-1} peak corresponding to 2D harmonic band could not be found in any of the samples meaning that probably they are composed of multi-layered GO sheets.

DOX spectrum presented in Figure 45 B shows some noise and small band resolution as it has been described that the band intensity and spectral profile of DOX is explicitly dependent of the laser of Raman spectrum and its intensity. Therefore in future measurements this could be improved using excitation with two different laser lines (one within DOX resonance area and other with out of the resonance region). Nevertheless, peaks of the spectral fingerprint of DOX are visible in Figure 45 B at 1244, 1412, 1442 and 1580 cm^{-1} similar to the DOX Raman spectra of other published works [118] [119]. The most intense band within the DOX Raman spectrum is found at approximately 1412 cm^{-1} which may be attributed to the phenyl ring vibration, and it is also in agreement with what has been described in the literature [118].

The spectral comparison of the Raman spectrum obtained for DOX-GQD-CB conjugates with the Raman spectrum obtained for GQD-CB (Figure 45 A) and for DOX (Figure 45 B) is illustrated in (Figure 45 C) where the assignments of vibrational modes of DOX are identified by the red dashed lines and the assignment of vibrational D band of GQD-CB is identified by the green dashed line and the assignment of vibrational band coming either from GQD-CB or from DOX (1580-1590 cm^{-1}) is identified as violet dashed line. In conclusion the conjugates possess bands from both DOX and GQD-CB, but conjugation has led to diminishing intensity of the vibrational modes in agreement to what has been observed for other conjugated systems [120] [121].

Interestingly, it was also found that with the exposure of the conjugates to an increase of Laser potency has led to a totally disappearance of the bands associated with DOX and to a clear enhancement of the bands D and G characteristic of GQD. This is probably due to the release of DOX from the conjugates upon a photothermic effect that promoted the disturbance of the π-π stacking interaction. Indeed, a similar release effect with increasing exposure time to laser showed the control release of DOX from gold nanocages due to photothermic effect followed by Raman spectroscopy [122].

The ratio of the intensities (I_D/I_G) of the characteristic D and G bands can be used to correlate the structural properties of the carbon and this intensity ratio is known to be inversely proportional to the crystalline grains in samples [123]. The I_D/I_G of GQD-CB Raman spectrum (Figure 45 A) was 0.99, while for instance the I_D/I_G of graphite was described to be 0.823 [116] This suggests that GQD-CB are more defective than graphite sheets, possibly due to the dominant contributions from the edge states at the periphery of GQDs. Furthermore, upon DOX release of conjugates (Figure 45 D), I_D/I_G of GQD-CB was 0.79 indicating that surface edge defective groups were probably lost by the highly energetic photothermic effect.

4 Conclusions and future perspectives

This work has succeeded in the production of GQDs that are able to immobilize an anticancer drug and to trigger the drug according to the pH value of the external media. The first step of the work involved the development, optimization and comparison of two different methods to produce GQD, as well as their chemical, optical and surface charge characterization at different pH values. Both GQD-CB and GQD-CVD have shown interesting optical properties, including a characteristic absorption spectra with a broad band with a maximum assigned to π-π* transition and a shoulder at 300 nm assigned to n-π* transition of the carbonyl groups. Concerning the CDV synthesis as a method to obtain GQD-CVD, the major problems associated are the wide variety of size distribution that is obtained in the glass substrate and the need to extract GQD-CVD from a glass substrate. Confocal Raman has confirmed the presence of single and multi-layered graphene with the carbon (D, 1590 cm^{-1} and G, 1325 cm^{-1}) and graphene (2D, 2700 cm^{-1}) characteristic bands and SEM provided microscopic images where was clearly possible to see clusters from few µm to <200 nm sized particles. An extraction method of GQD-CVD based on pH adjustment and sonication allowed the extraction of particles from the glass substrate, but both the extraction method and the production method need further development. In view to this, the chemical synthesis to obtain GQD was chosen as a preferred method for this work purposes and the conclusions of this work are focused on GQD-CB.

GQD-CB have shown to be fluorescent for all the pH values tested with an average λem_{max} of 543 nm (green emission) and λex_{max} = 450 nm. The λem_{max} of GQD-CB seemed to be dependent of the pH at which the samples were irradiated, which can be entirely related with the large effect of pH in the surface edge functional groups of GQD-CB. The presence of isobestic points in the emission spectra and the zeta potential analysis were coherent with that pH-dependency of the GQD-CB functional groups. These facts provided a description of GQD-CB surface groups and surface charge and led us to the conclusion that GQD-CB are almost neutral until pH 4.5 whereas for higher pH values GQD-CB become more negatively charged due to surface carboxyl negatively charged groups and negatively charged aromatic hydroxyl groups.

As a final goal of this work was to reach conjugates of GQD and DOX that are encapsulated in NLC for drug delivery purposes, it was developed a method to control the size of GQDs and their incorporation into a lipid membrane was also accessed. The proposed pressure-extrusion process showed to be efficient and the closest to an accurate process of separating GQD-CB by sizes (GQD-CBext), without changing their surface charge and optical properties. The incorporation of GQDs into 3AS and 12AS probe-labelled lipid membranes was studied for non-filtered GQD-CB and GQD-CBext. GQD-CBext quenched both probes, being preferentially located near the polar head groups but also achieving deeper locations. Non-filtered GQD-CB were the strongest quenchers and located almost in the same percentage (≈80%) in superficial and deep regions, causing a ≈15 nm red shift on the probe's emission signal.

To understand the formation of DOX and GQDs conjugates it was necessary to study thoroughly the optical properties of the free drug and its pH dependency. DOX showed its typical optical properties, with an almost constant molar extinction coefficient at the acid and neutral pH region (10396 $Lmol^{-1}cm^{-1}$, pH 3.0), that gradually decreased at the alkaline region (9426 $Lmol^{-1}cm^{-1}$, pH 9.0; 7780 $Lmol^{-1}cm^{-1}$, pH 11.0). Studies of drug stability were also performed and revealed small decreases of ε in acid (about 1%) but significant ε decrease at higher pH values (19.71%, pH 9.0) which can be interpreted as a marked drug instability at alkaline pH. Along with pH increase, there is a red shift on maximum absorption wavelength of DOX, from 481 nm (acid buffers) to 589 nm (alkaline), visible through a change on the samples colour.

According to the in silico DOX characteristics and to the measured GQD-CB features, it was predicted that DOX-GQD-CB would interact in the following manner: (i) no interaction until pH 4.5-5.0 (GQD-CB are neutral and DOX is protonated), (ii) electrostatic interaction by opposite charge attraction between pH 5.0 and 8.0 (GQD-CB are negatively charged and DOX protonated), (iii) electrostatic interaction by opposite charge attraction but also charge repulsion between pH 8.0 and 9.0 (GQD-CB negatively charged and DOX is protonated but also negatively charged) and finally (iv) no interaction due to charge repulsion in pH>9 (GQD-CB are negatively charged and DOX is also negatively charged).

Optical analysis to either free drug or GQD-CB or a mixture of both at different drug concentrations and pH values were performed to confirm the interaction behaviour described above. When conjugates are formed between GQD-CB and DOX, their absorption spectra is different from the additive spectra of the isolated components. Also, there is a blue shift on λ_{max} from the free DOX spectra (that show a constant λ_{max} despite the concentration) to the DOX-GQD-CB spectra, and a red shift within the DOX-GQD-CB spectra at the same pH with the increase of DOX concentration. This happened the most for pH 6 and 9, was slightly visible at pH 3 and almost negligible for pH 11, confirming the in silico interaction prediction and conjugate formation. The DOX-GQD-CB conjugates formation at pH 6 was further confirmed by fluorescence, where energy transfer occurred from GQD-CB to DOX and the DOX-GQD-CB spectrum had shown the characteristic peaks of free DOX, for all the concentrations of DOX studied. This predominance of DOX-shaped spectra demonstrated that DOX was in excess of comparison to GQD-CB. The ratio between emission bands of the conjugate samples was smaller than the ratio found for free DOX at aqueous solutions, which also indicates conjugates formation.

Raman analysis has also confirmed the conjugate formation at pH 6, showing a decrease on the ID/IG ratio from 0.99 (free GQD-CB) to 0.76 (DOX-GQD-CB), which is common when there is a decrease on carbon edge defects associated to bonding formation. The characteristic Raman peaks from DOX were shown at the free DOX sample and two of these peaks, 1412 cm^{-1} and 1244 cm^{-1}, also appeared at the DOX-GQD-CB spectrum. However, with the increase of laser intensity, these two DOX peaks disappeared by photothermic effect release of the drug, remaining only the GQD-CB peaks (D band, 1340 cm^{-1}; G band, 1590 cm^{-1}) with stronger intensity.

Finally, FTIR analysis showed the many oxygen-containing groups present at the edges of GQD-CB that make GQD-CB suitable to adsorb DOX through hydrogen bonding. It was also seen the reduction

of the 1580 cm^{-1} bands (attributed to aromatic C=C) of GQD-CB upon conjugation with DOX, confirming also the π-π stacking interactions between both.

As a final conclusion it is possible to summarize that GQD-CB and DOX conjugates were successfully produced and the conditions for higher conjugation were studied. The possible adsorption mechanism of DOX and GQD-CB are probably due to electrostatic interaction, hydrogen bonding and π- π stacking interaction. The conjugates were size tuned, and successfully incorporated in lipid nanocarriers. Therefore this project provides fundamental understanding of the adsorption conditions between DOX and GQD-CB and benefits the development of a hybrid pH triggering nanosystem for drug delivery.

4.1 Future work

As a very recent study area, there is a lot of knowledge lines that can be interestingly explored. As relevant future work, we suggest:

- Repetition of pressure-extrusion separation of GQD-CB, with the same FL, DLS and ELS characterization techniques but also with complementary ones as Transmission electron microscopy (TEM) and AFM, in order to confirm the differences in GQD-CB topography and size;
- Application of the pressure-extrusion separation procedure to the GQD-CVD extracted from substrate and use the same characterization techniques to explore their properties in suspension;
- Repetition of the extraction procedure for GQD-CVD from glass, with the same characterization techniques described above;
- Complementary studies of the surface groups of GQDs and GQD-DOX conjugates with different characterization techniques (ex: XPS e EDXS);
- Functionalization of GQDs surface with groups that promote a stronger bonding between DOX and dots (ex: promote an amide bonding between DOX and dots);
- FTIR, confocal Raman and fluorescent analysis of free DOX, free GQD-CB and DOX-GQD-CB for the other pH studied (pH 3, 9 and 11) in order to compare the results and confirm the *in silico* interaction prediction through this characterization techniques in addition to the obtained UV-Vis spectroscopy;
- Make a titration of a DOX-GQD-CB suspension and characterize the samples for different pH values in order to observe and prove the adsorption and desorption behaviour with the pH variation and thus to confirm GQD triggering effect;
- Isolation of the conjugates from the surplus free DOX and GQD-CB on the suspensions in order to obtain only the DOX-GQD-CB and study their incorporation into labelled liposomes. Analyse the zeta potential of the conjugates comparing to the free GQD-CB and try an electrodynamic approach;
- Use the GQDs with the same NLC strategy with complementary therapies (example: complexation of nucleic acids such as siRNA to silence genes involved in cancer cells resistance to anti-cancer drugs).

References

[1] Infarmed - National Version , “Doxorrubicina Medicamento,” SPC (PT), Lisboa, 2014.

[2] M. Lúcio, “GraphLightCancer Graphene Quantum Dots for a Theranostic Approach to Cancer Treatment,” Universidade do Minho, Braga, Portugal, 2016.

[3] DrugBank, Canada, “DrugBank Drugs,” DrugBank, [Online]. Available: https://www.drugbank.ca/drugs/DB00997. [Accessed 06 2016].

[4] K. S. Novoselov, S. V. Morozov, T. M. G. Mohinddin, L. A. Ponomarenko, D. C. Elias, R. Yang, I. I. Barbolina, P. Blake, T. J. Booth, D. Jiang, J. Giesbers, E. W. Hill and A. K. Geim, “Electronic properties of graphene,” *Physica Status Solid b,* Vols. 244, No.11, pp. 4106-4111, 2007.

[5] L. Li, G. Wu, G. Yang, J. Peng, J. Zhao and J.-J. Zhu, “Focusing on luminescent graphene quantum dots: current status and future perspectives,” *Nanoscale,* vol. 5, pp. 4015-4039, 2013.

[6] J. Usberco and E. Salvador, Quimica 3 Quimica Orgânica, São PAulo, Brasil: Saraiva, 2002.

[7] S. Wu, X. Zhao, Y. Li, Q. Du, J. Sun, Y. Wang, X. Wang, Y. Xia, Z. Wang and L. Xia, “Adsorption Properties of Doxorubicin Hydrochloride onto Graphene Oxide: Equilibrium, Kinetic and Thermodynamic Studies,” *Materials,* vol. 6, pp. 2026-2042, 2013.

[8] J. d. L. Fuente, “Graphenea,” [Online]. Available: https://www.graphenea.com/pages/cvd-graphene#.WQyI7eXyvIU. [Accessed 06 2016].

[9] Y. Dong, J. Lin, Y. Chen, F. Fu, Y. Chi and G. Chen, “Graphene quantum dots, graphene oxide, carbon quantum dots and graphite nanocrystals in coals,” *Nanoscale,* vol. 6, pp. 7410-7415, 2014.

[10] Y. Wang, L. Polavarapu and L. M. Liz-Marzán, “Reduced Graphene Oxide-Supported Gold Nanostars for Improved SERS Sensing and Drug Delivery,” *Applied Materials & Interfaces,* vol. 6, pp. 21798-21805, 2014.

[11] A. S. Hassanien, R. A. Shedeed and N. K. Allam, “Graphene Quantum Sheets with Multiband Emission: Unravelling the Molecular Origin of Graphene Quantum Dots,” *The Journal of Physical Chemistry C,* vol. 120, pp. 21678-21684, 08 2016.

[12] S. Dey, A. Govindaraj, K. Biswas and C. Rao, “Luminescent properties of boron and nitrogen doped graphene quatum dots prepared from arc-discharged-generated ddoped graphene samples,” *Chemical Physics Letters,* Vols. 595-596, pp. 203-208, 2014.

[13] Q. Wang, X. Huang, Y. Long, X. Wang, H. Zhang, R. Zhu, L. Liang, P. Teng and H. Zheng, “Hollow luminescent carbon dots for drug delivery,” *Carbon,* vol. 59, pp. 192-199, 2013.

[14] S. Zhu, Y. Song, X. Zhao, J. Shao, J. Zhang and B. Yang, “The photoluminescence mechanism in carbon dots (graphene quantum dots, carbon nanodots, and polymer dots): Current state and future perspective,” *Nano Research,* vol. 8(2), pp. 355-381, 2015.

[15] J. Shen, Y. Zhu, X. Yang and C. Li, “Graphene quantum dots: emergent nanolights for bioimaging, sensors, catalysis and photovoltaic devices,” *Chem. Commun.,* vol. 48, p. 3686–3699, 2012.

[16] P. Silvestrov and K. Efetov, “Quantum Dots in Graphene,” *Physical Reviwe Letters,* vol. 98, p. 016802, 2007.

[17] H. Zhu, A. Liu, F. Shan, W. Yang, W. Zhang, D. Li and J. Liu, “One-step synthesis of graphene quantum dots from defective CVD graphene and their application in IGZO UV thin film phototransistor,” *Carbon,* vol. 100, pp. 201-207, 2016.

[18] H. Tetsuka, R. Asahi, A. Nagoya, K. Okamoto, I. Tajima, R. Ohta and A. Okamoto, “Optically Tunable Amino-Functionalized Graphene Quantum Dots,” *Advanced Materials,* vol. 24, pp. 5333-5338, 2012.

[19] J. Wang, C. Cheng, Y. Huang, B. Zheng, H. Yuan, L. Bo, M.-W. Zheng, S.-Y. Yang, Y. Guo and D. Xiao, “A facile large-scale microwave synthesis of highly fluorescent carbon dots from benzenediol isomers,” *J. Mater. Chem. C,* vol. 2, pp. 5028-5035, 2014.

[20] S. Chen, J.-W. Liu, M.-L. Chen, X.-W. Chen and J.-H. Wang, “Unusual emission transformation of graphene quantum dots induced by self-assembled aggregation,” *Chem. Commun.,* vol. 48, pp. 7637-7639, 2012.

[21] Q. Lu, C. Wu, D. Liu, H. Wang, W. Su, H. Li, Y. Zhang and S. Yao, “A facile and simple method for synthesis of graphene oxide quantum dots from black carbon,” *Green Chemistry,* vol. 19, pp. 900-904, 2017.

[22] F. Yang, M. Zhao, B. Zheng, D. Xiao, L. Wu and Y. Guo, “Influence of pH on the fluorescence properties of graphene quantum dots using ozonation pre-oxide hydrothermal synthesis,” *Journal of Materials Chemistry,* vol. 22, pp. 25471-25479, 2012.

[23] S. Zhu, J. Zhang, C. Qiao, S. Tang, Y. Li, W. Yuan, B. Li, L. Tian, F. Liu, R. Hu, H. Gao, H. Wei, H. Zhang, H. Sun and B. Yang, “Strongly green-photoluminescent graphene quantum dots for bioimaging applications,” *Chem. Commun.,* vol. 47, p. 6858–6860, 2011.

[24] Y. Dong, C. Chen, X. Zheng, L. Gao, Z. Cui, H. Yang, C. Guo, Y. Chi and C. M. Li, “One-step and high yield simultaneous preparation of single- and multi-layer graphene quantum dots from CX-72 carbon black,” *Journal of Materials Chemistry,* vol. 22, pp. 8764-8766, 2012.

[25] S. Zhuo, M. Shao and S.-T. Lee, “Upconversion and Downconversion Fluorescent Graphene Quantum Dots: Ultrasonic Preparation and Photocatalysis,” *ACS Nano,* Vols. 6, No.2, pp. 1059-1064, 2012.

[26] M. Zhang, L. Bai, W. Shang, W. Xie, H. Ma, Y. Fu, D. Fang, H. Sun, L. Fan, M. Han, C. Liub and S. Yang, “Facile synthesis of water-soluble, highly fluorescent graphene quantum dots as a robust biological label for stem cells,” *Journal of Materials Chemistry,* vol. 22, pp. 7461-7467, 2012.

[27] B. Han, M. Yu, T. Pen, Y. Li, X. Hu, R. Xiang, X. Hou and G. He, “One-step extracting high fluorescent carbon quantum dots by physical method from carbon black,” *New Journal of Chemistry,* 2017.

[28] X. Zhou, Y. Zhang, C. Wang, X. Wu, Y. Yang, B. Zheng, H. Wu, S. Guo and J. Zhang, “Photo-Fenton Reaction of Graphene Oxide: A New Strategy to Prepare Graphene Quantum Dots for DNA Cleavage,” ACS Nano, China, 2012.

[29] J. Lu, P. S. E. Yeo, C. K. Gan, P. Wu and K. P. Loh, “Transforming C60 molecules into graphene quantum dots,” *Nature Nanotechnology,* vol. 6, pp. 247-252, 2011.

[30] M. L. Mueller, X. Yan, J. A. McGuire and L.-s. Li, “Triplet States and Electronic Relaxation in Photoexcited Graphene Quantum Dots,” *Nano Letters,* vol. 10, pp. 2679-2682, 2010.

[31] X. Wu, F. Tian, W. Wang, J. Chen, M. Wub and J. X. Zhao, “Fabrication of highly fluorescent graphene quantum dots using L-glutamic acid for in vitro/in vivo imaging and sensing,” *Journal of Materials Chemistry C,* 2013.

[32] R. Liu, D. Wu, X. Feng and K. Müllen, “Bottom-Up Fabrication of Photoluminescent Graphene Quantum Dots with Uniform Morphology,” *J. Am. Chem. Soc.,* vol. 133, p. 15221–15223, 2011.

[33] Y. R. Chen, C. L. Chung and G. C. a. Y. Tzeng, “Independently Controlled Etching and Growth of Graphene Quantum Dots and Their SERS Applications,” in *Proceedings of the 16th International Conference on Nanotechnology*, Sendai, Japan, 2016.

[34] P. M. Carrasco, S. Montes, I. García, M. Borghei, H. Jiang, I. Odriozola, G. Cabañero and V. Ruiz, “High-concentration aqueous dispersions of graphene produced by exfoliation of graphite using cellulose nanocrystals,” *Carbon,* vol. 70, pp. 157-163, 2014.

[35] M. Bottini, C. Balasubramanian, M. I. Dawson, A. Bergamaschi, S. Bellucci and T. Mustelin, “Isolation and Characterization of Fluorescent Nanoparticles from Pristine and Oxidized Electric Arc-Produced Single-Walled Carbon Nanotubes,” *J. Phys. Chem. B,* vol. 110, pp. 831-836, 2006.

[36] Y.-P. Sun, B. Zhou, Y. Lin, W. Wang, K. A. S. Fernando, P. Pathak, M. J. Meziani, B. A. Harruff, X. Wang, H. Wang, P. G. Luo, H. Yang, M. E. Kose, B. Chen, L. M. Veca and S.-Y. X, “Quantum-Sized Carbon Dots for Bright and Colorful Photoluminescence,” Journal of the American Chemical Society, 2006.

[37] J. Lee, K. Kim, W. I. Park, B.-H. Kim, J. H. Park, T.-H. Kim, S. Bong, Chul-Hong Kim, G. Chae, M. Jun, Y. Hwang, Y. S. Jung and S. Jeon, “Uniform Graphene Quantum Dots Patterned from Self-Assembled Silica Nanodots,” *Nano Letters,* 2012.

[38] S. C. Freitas, *Thin films,* Lisboa, 2014/2015.

[39] J. R. Prekodravac, Z. M. Markovi´c, S. P. Jovanovi´c, I. D. Holclajtner-Antunovi´c, D. P. Kepi´c, M. D. Budimir and B. M. Todorovi´c-Markovi´c, “Graphene quantum dots and fullerenol as new carbon sources for single–layer and bi–layer graphene synthesis by rapid thermal annealing method,” *Materials Research Bulletim,* vol. 88, pp. 114-120, 12 2017.

[40] L. Fan, M. Zhu, X. Lee, R. Zhang, K. Wang, J. Wei, M. Zhong, D. Wu and H. Zhu, “Direct Synthesis of Graphene Quantum Dots by Chemical Vapor Deposition,” *Particle & Particle Systems Characterization,* 2013.

[41] Z. Fan, Y. Li, X. Li, L. Fan, S. Zhou, D. Fang and S. Yang, “Surrounding media sensitive photoluminscence of boron-doped graphene quantum dots for higly fluorescent dyed crystals, chemical sensing and bioimaging,” *Carbon,* vol. 70, pp. 149-156, 2014.

[42] Y. He, L. Zhang, Z. Chen, Y. Liang, Y. Zhang, Y. Bai, J. Zhang and Y. Li, “Enhanced chemotherapy efficacy by co-delivery of shABCG2 and doxorubicin with a pH-responsive charge-reversible layered graphene oxide nanocomplex,” *Journal of Materials Chemistry B,* vol. 3, pp. 6462-6472, 2015.

[43] L. Zhou, Z. Li, Z. Liu, J. Ren and X. Qu, “Luminescent Carbon Dot-Gated Nanovehicles for pH-Triggered Intracellular Controlled Release and Imaging,” *Langmuir,* vol. 29, pp. 6396-6403, 2013.

[44] X. Zhao, L. Liu, X. Li, J. Zeng, X. Jia and P. Liu, “Biocompatible Graphene Oxide Nanoparticle-Based Drug Delivery Platform for Tumor Microenvironment-Responsive Triggered Release of Doxorubicin,” *Langmuir,* vol. 30, pp. 10419-10429, 2014.

[45] Z. Liu, J. T. Robinson, X. Sun and H. Dai, “PEGylated Nano-Graphene Oxide for Delivery of Water Insoluble Cancer Drugs,” *J. AM. CHEM. SOC.,* vol. 130, p. 10876–10877, 2008.

[46] C. Wang, C. Wu, X. Zhou, T. Han, X. Xin, J. Wu, J. Zhang and S. Guo, “Enhancing Cell Nucleus Accumulation and DNA Cleavage Activity of Anti-Cancer Drug via Graphene Quantum Dots,” *SCIENTIFIC REPORTS,* vol. 3, p. 2852, 2013.

[47] J. Peng, W. Gao, B. K. Gupta, Z. Liu, R. Romero-Aburto, L. Ge, L. Song, L. B. Alemany, X. Zhan, G. Gao, S. A. Vithayathil, B. A. Kaipparettu, A. A. Marti, T. Hayashi, J.-J. Zhu and Ajayan, "Graphene Quantum Dots Derived from Carbon Fibers," *NanoLetters,* vol. 12, p. 844−849, 2012.

[48] S. Zhu, J. Zhang, S. Tang, C. Qiao, L. Wang, H. Wang, X. Liu, B. Li, Y. Li, W. Yu, X. Wang, H. Sun and B. Yang, "Surface Chemistry Routes to Modulate the Photoluminescence of Graphene Quantum Dots: From Fluorescence Mechanism to Up-Conversion Bioimaging Applications," Advanced Functional Materials, China, 2012.

[49] Infarmed, "Doxorrubicina Teva - Folheto Informativo: Informação para o utilizador," Infarmed, Lisboa, 2009.

[50] PubChem - Open Chemistry Database, "Compound Summary for CID 31703 Doxorubicin," [Online]. Available: https://pubchem.ncbi.nlm.nih.gov/compound/doxorubicin. [Accessed 05 2016].

[51] R. J. Sturgeon and S. G. Schulman, "Electronic Absorption Spectra and Protolytic Equilibria of Doxorubicin: Direct Spectrophotometric Determination of Microconstants," *Journal of Pharmaceutical Sciences,* Vols. 66, No.7, pp. 958-961, July 1977.

[52] Y. (. Barenholz, "Doxil® — The first FDA-approved nano-drug: Lessons learned," *Journal of Controlled Release,* vol. 160, pp. 117-134, 2012.

[53] R. Anand, S. Ottani, F. Manoli, I. Manet and S. Monti, "A close-up on doxorubicin binding to c-cyclodextrin: an elucidating spectroscopic, photophysical and conformational study," *RSC Advances,* vol. 2, pp. 2346-2357, 2012.

[54] G. Raval, "Thermodynamic and Spectroscopic Studies on the Molecular Interaction of Doxorubicin (DOX) with negatively charged Polymeric Nanoparticles," Department of Pharmaceutical Sciences, University of Toronto, Canada, 2012.

[55] P. Yousefpour, F. Atyabi, E. V. Farahani, R. Sakhtianchi and R. Dinarvand, "Polyanionic carbohydrate doxorubicin–dextran nanocomplex as a delivery system for anticancer drugs: in vitro analysis and evaluations," *International Journal of Nanomedicine,* vol. 6, pp. 1487-1496, 2011.

[56] N. Yabbarov, G. Posypanova, E. Vorontsov, O. Popova and E. S. Severin, "Targeted Delivery of Doxorubicin: Drug Delivery System Based on PAMAM Dendrimers," *Biochemistry,* Vols. 78, No.8, pp. 884-894, 2013.

[57] P. Changenet-Barret, T. Gustavsson, D. Markovitsi, I. Manet and S. Monti, "Unravelling molecular mechanisms in the fluorescence spectra of doxorubicin in aqueous solution by femtosecond fluorescence spectroscopy," *Phys.Chem. Chem. Phys.,* vol. 15, pp. 2937-2944, 2013.

[58] N. Raghunand, X. He, R. v. Sluis, B. Mahoney, B. Baggett, C. Taylor, G. Paine-Murrieta, D. Roe, Z. Bhujwalla and R. Gillies, "Enhancement of chemotherapy by manipulation of tumour pH," *British Journal of Cancer,* vol. 80(7), pp. 1005-1011, 1999.

[59] K. K. Karukstis, E. H. Thompson, J. A. Whiles and R. J. Rosenfeld, "Deciphering the fluorescence signature of daunomycin and doxorubicin," *Biophysical Chemistry,* vol. 73, pp. 249-263, 1998.

[60] A. Carvalho, I. Lopes, O. Gonçalves, E. Bárbara, M. E. C. R. Oliveira and M. Lúcio, Polymeric Versus Lipid Nanoparticles: Comparative Study of Nanoparticulate Systems as Indomethacin Carriers, Journal of Applied Solution Chemistry and Modeling, 2015.

[61] A. C. Oliveira, K. Raemdonck, T. Martens, K. Rombouts, R. Simón-Vázquez, C. Botelho, I. Lopes, M. Lúcio, Á. González-Fernández, M. E. C. R. Oliveira, A. C. Gomes and K. Braeckmans, "Stealth monoolein-based nanocarriers for delivery of siRNA to cancer cells," *Acta Biomaterialia,* 2015.

[62] J. Silva, A. Oliveira, M. Lúcio, A. Gomes, P. Coutinho and M. Oliveira, “Tunable pDNA/DODAB:MO lipoplexes: the effect of incubation temperature on pDNA/DODAB:MO lipoplexes structure and transfection efficiency.,” Colloids and Surfaces B Biointerfaces, Portugal, 2013.

[63] J. N. Silva, I. Oliveira, A. Oliveira, M. Lúcio, A. Gomes, P. Coutinho and M. R. Oliveira, “Structural dynamics and physicochemical properties of pDNA/DODAB:MO lipoplexes: Effect of pH and anionic lipids in inverted non-lamellar,” *Biochimica et Biophysica Acta ,* vol. 1838 , p. 2555–2567, 2014.

[64] A. Neves, M. Lúcio, S. Martins, J. Lima and S. Reis, “Novel resveratrol nanodelivery systems based on lipid nanoparticles to enhance its oral bioavailability,” Portugal, 2012.

[65] D. Needhamf and E. Evans, “Structure and Mechanical Properties of Giant Lipid (DMPC) Vesicle Bilayers from 20 "C below to 10 "C above the Liquid Crystal-Crystalline Phase Transition at 24 "C,” *Biochemistry,* vol. 27, pp. 8261-8269, 1988.

[66] M. Salim, H. Minanikawa, A. Sugimura and R. Hashima, “Amphiphilic designer nano-carriers for controlled release, from drug delivery to diagnostics,” *Medical Chemistry Communications,* 2014.

[67] R. O. Ryan, “Nanobiotechnology applications of reconstituted high density lipoprotein,” *Journal of Nanobiotechnology,* vol. 8, p. 28, 2010.

[68] Y. P. Patil and S. Jadhav, “Novel methods for liposome preparation,” Chemistry and Physics of Lipids , 2014.

[69] D. W. Deamer, R. Leonard, A. Tardieu and D. Branton, “LAMELLAR AND HEXAGONAL LIPID PHASES VISUALIZED BY FREEZE-ETCHING,” *Biochimica et Biophysica Acta,* vol. 219, pp. 47-60, 1970.

[70] V. Luzzati and A. Tardieu, “Lipid phases: structure and structural transitions,” *Annual Reviews,* vol. 25, no. Physic Chemistry, pp. 79-94, 1974.

[71] E. E. D. Needhamf, “Structure and Mechanical Properties of Giant Lipid (DMPC) Vesicle Bilayers from 20 "C below to 10 "C above the Liquid Crystal-Crystalline Phase Transition at 24 "C,” American Chemical Society, Vancouver and Canada, 1988.

[72] Universidade Federal do Rio de Janeiro, “Aula II Membranas Algumas propriedades físico-químicas,” 2017.

[73] H. M. A Khajeh, “Effect of cholesterol on behavior of 5-fluorouracil (5-FU) in a DMPC lipid bilayer, a molecular dynamics study,” Elsevier - Biophysical chemistry, 2014.

[74] Y. L. P. X. X. L. C. Z. L. Hujun Shen, “An anisotropic coarse-grained model based on Gay–Berne and electric multipole potentials and its application to simulate a DMPC bilayer in an implicit solvent model,” Journal of Computational Chemistry, 2015.

[75] Y. T. ,. Q. P. ,. N. L. a. S. Y. Heng-Liang Wu, “Phase transition behaviors of the supported DPPC bilayer investigated by sum frequency generation (SFG) vibrational spectroscopy and atomic force microscopy (AFM),” Royal Society of Chemestry - Physical Chemistry Chemical Physics, Hokkaido University, Japan, 2015.

[76] M. Wanga, T. Zanderc, X. Liua, C. Liua, A. Raja, D. F. Wielandc, V. M. Garamusc, R. Willumeit-Römerc, P. M. Claessona and A. Dėdinaitėa, “The effect of temperature on supported dipalmitoylphosphatidylcholine (DPPC) bilayers: Structure and lubrification performance,” Elsevier - Journal of Colloid and Interface Science, 2015.

[77] H. I. Petrache, S. Tristram-Nagle and J. F. Nagle, “Fluid phase structure of EPC and DMPC bilayers,” *Chemistry and Physics of Lipids,* vol. 95, pp. 83-94, 1998.

[78] T. M. Allena and P. R. Cullis, “Liposomal drug delivery systems: From concept to clinical applications,” 2013.

[79] P. Atkins and d. P. Julio, Físico-Química Biológica, LTC - Livros Técnicos e Científicos Editora S.A., 2006.

[80] FCT, TÉCNICAS DE CARACTERIZAÇÃO DE CARACTERIZAÇÃO DE CARACTERIZAÇÃO DE MATERIAIS, Microscopia de Visível, Portugal, 2016-2017.

[81] Maxwell, PUC, Rio de Janeiro, Brasil, "Introdução à Fluorescência," [Online]. Available: https://www.maxwell.vrac.puc-rio.br/15676/15676_3.PDF. [Accessed 06 2016].

[82] D. A. Skoog, D. M. West and F. J. Holler, Fundamentos de química analítica, Volume 2, Reverte, 1997.

[83] M. Lúcio, "Fluorescence and anisotropy studies as a toolbox for pharmacokinetic evaluation of drug-delivery systems," University of Minho, CFUM, Department of Physics, Braga, Portugal, 2016.

[84] M. Hof and R. Machán, "Quenching of Fluorescence," Institute of Physical Chemistry, Faculty of Biomedical Engineering, Czech Technical University, Prague, Czech Republic, 2017.

[85] J. Lakowicz, Principles of Fluorescence Spectroscopy 3rd ed. ed.,, New York: Springer, 2006.

[86] Washington University in St Louis, "Nano Research Facility - Dynamic Light Scattering (DLS)," [Online]. Available: https://wustl.edu/. [Accessed 07 2016].

[87] PSS Particle Sizing Systems, "ELS Electrophoretic light scattering," PSS, USA, [Online]. Available: http://pssnicomp.com/glossary/els/. [Accessed 05 2016].

[88] R. Shaw, "DLS Dynamic Light Scattering Training," [Online]. Available: https://www.atascientific.com.au/. [Accessed 05 2016].

[89] Brookhaven Instruments Corporation, "Zeta Potential Analytical Instruments," Brookhaven, [Online]. Available: https://brookhaveninstruments.com/zeta-potential-analytical-instruments?gclid=CjwKEAjw5_vHBRCBtt2NqqCDjiESJABD5rCJrSuFL6GG0BuAe5DPmgX5K-pOzOfwHqZgVI-_tmOwbxoCW4Dw_wcB. [Accessed 07 2016].

[90] Princeton Instruments, "Confocal Raman Microscopy General Overview," [Online]. Available: www.piacton.com. [Accessed 07 2016].

[91] In Photonics, "What is Raman Spectroscopy?," [Online]. Available: http://www.inphotonics.com/raman.htm. [Accessed 06 2016].

[92] University of Cambridge, UK, "https://www.doitpoms.ac.uk/tlplib/raman/," [Online]. Available: https://www.doitpoms.ac.uk/tlplib/raman/comparison.php. [Accessed 05 2016].

[93] Craic Thecnologies, "Micro-raman-spectroscopy," [Online]. Available: http://www.microspectra.com/support/technical-support/raman-science/35-technical-support/126-science-of-micro-raman-spectroscopy. [Accessed 07 2016].

[94] M. d. C. Paiva, *Espectroscopia de Infravermelhos,* Universidade do Minho, Portugal, 2016.

[95] FCT, *TÉCNICAS DE CARACTERIZAÇÃO DE CARACTERIZAÇÃO DE CARACTERIZAÇÃO DE MATERIAIS, Microscopia de Infravermelho e Raman,* Portugal, 2016-2017.

[96] M. C. Evora, O. L. Gonçalez, R. C.L.Dutra, M. F. Diniz, H. Wiebeck and L. G. d. A. e. Silva, "Comparação de Técnicas FTIR de Transmissão, Reflexão e Fotoacústica na Análise de Poliamida-6, Reciclada e Irradiada," *Polímeros: Ciência e Tecnologia,* Vols. 12, No. 1, pp. 60-68, 2002.

[97] PerkinElmer, *FT-IR Spectroscopy: Attenuated Total Reflectance (ATR).*

[98] D. E. N. P. E. By Joseph Goldstein, D. C. Joy, A. D. R. Jr., C. E. Lyman, C. Fiori and E. Lifshin, Scanning Electron Microscopy and X-Ray Microanalysis: A Text for Biologists, Materials Scientists and Geologists. 2nd Edition, Springer, 1992.

[99] J. I. Goldstein, D. E. Newbury, J. W. Colby, H. Yakowitz, E. Lifshin and J. R. Coleman, Practical Scanning Electron Microscopy: Electron and Ion Microprobe Analysis, New York: Springer, 1975.

[100] R. Silva, "A miscroscopia eletrónica de varrimento no estudo dos materiais," DCM, FCT, UNL, Lisboa, 2016.

[101] B. D. D.D. Perrin, "Buffers for pH and Metal Ion Control," Chapman and Hall, London, 1974.

[102] M. Lúcio, C. Nunes, D. Gaspar, K. Gołe¸bska, M. Wisniewski, J. Lima, G. Brezesinski and S. Reis, "Effect of anti-inflammatory drugs in phosphatidylcholine membranes: A fluorescence and calorimetric study," Elsevier, Portugal, Germany, 2008.

[103] A. P. Demchenko and M. O. Dekaliuk, "Novel fluorescent carbonic nanomaterials for sensing and imaging," IOP PUBLISHING , Kiev-01601, Ukraine, 2013.

[104] S. N. Baker and G. A. Baker, "Luminescent Carbon Nanodots: Emergent Nanolights," *Angewandte Chemie,* vol. 49, pp. 6726-6744, 2010.

[105] D. Pan, J. Zhang, Z. Li and M. Wu, "Hydrothermal Route for Cutting Graphene Sheets into Blue-Luminescent Graphene Quantum Dots," *Advanced Materials,* vol. 22, pp. 734-738, 2010.

[106] S. Kochmann, T. Hirsch and O. S. Wolfbeis, "The pH Dependence of the Total Fluorescence of Graphite Oxide," © Springer Science+Business Media, Germany, 2011.

[107] J. Qiu, R. Zhang, J. Li, Y. Sang, W. Tang, P. R. Gil and H. Liu, "Fluorescent graphene quantum dots as traceable, pH-sensitive drug delivery systems," International Journal of Nanomedicine, 2015.

[108] D. Kaushik and G. Bansal, "Four new degradation products of doxorubicin: An application of forced degradation study and hyphenated chromatographic techniques," *Journal of Pharmaceutical Analysis,* 2015.

[109] A. Dias, A. P. Varela, M. d. G. Miguel, A. L. Macanita and R. S. Becker, ".beta.-Carboline photosensitizers. 1. Photophysics, kinetics and excited-state equilibria in organic solvents, and theoretical calculations," *J. Phys. Chem,* vol. 96, pp. 10290-10296, 1992.

[110] M. Balón, P. G. M. A. Muñoz, J. Hidalgo and C. Carmona, "Photophysics and photochemistry of betacarbolines; Trends in Photochemistry and Photobiology, Vol. 3, pp. 117–138," Council of Scientific Information, 1994.

[111] H.-H. Perkampus, UV-VIS Spectroscopy and Its Applications, Springer, 1992.

[112] V. Karachevtsev, A. Plokhotnichenko, M. Karachevtsev and V. Leontiev, "Decrease of carbon nanotube UV light absorption induced by p–p-stacking interaction with nucleotide bases," *C A R B ON ,* vol. 4 8 , p. 3 6 8 2 –3 6 9 1, 2010.

[113] M. Balón, P. Guardado, M. A. Munõz and C. Carmona, "A Spectroscopic Study of the Hydrogen Bonding and p– p Stacking Interactions of Harmane with Quinoline," *Biospectroscopy,* vol. 4, p. 185–195, 1997.

[114] K. Pal, S. Mallick and A. L. Koner, "Complexation induced fluorescence and acid–base properties of dapoxyl dye with c-cyclodextrin: a drug-binding application using displacement assays," *Phys.Chem.Chem.Phys.,* vol. 17, pp. 16015-16022, 2015.

[115] Y. J. Wang, Z. Li, J. Tong, X. Y. Shen, A. Qin, J. Z. Sun and B. Z. Tang, “Fluorescence Property and Aggregation Behavior of Tetraphenylethene-Perylenebisimide Dyads,” *Journal of Materials Chemistry C,* 2015.

[116] Y. Qin, Z.-W. Zhou, S.-T. Pan, Z.-X. He, X. Zhang, J.-X. Qiu, W. Duan, T. Yang and S.-F. Zhou, “Graphene quantum dots induce apoptosis, autophagy, and inflammatory response via p38 mitogen-activated protein kinase and nuclear factor-kB mediated signaling pathways in activated THP-1 macrophages,” *Toxicology,* vol. 327, pp. 62-76, 2015.

[117] N. Suzuki, Y. Wang, P. Elvati, Z.-b. Qu, K. Kim, S. Jiang, E. Baumeister, J. Lee, B. Yeom, J. H. Bahng, J. Lee, A. Violi and N. A. Kotov, “Chiral Graphene Quantum Dots,” *ACS Nano,* pp. 1-38, 2016.

[118] G. DAS, A. NICASTRI, M. L. COLUCCIO, F. GENTILE, P. CANDELORO, G. COJOC, C. LIBERALE, F. D. ANGELIS and E. D. FABRIZIO, “FT-IR, Raman, RRS Measurements and DFT Calculation for Doxorubicin,” *MICROSCOPY RESEARCH AND TECHNIQUE,* vol. 73, pp. 991-995, 2010.

[119] N. Strekal, A. German, G. Gachko, A. Maskevich and S. Maskevich, “The study of the doxorubicin adsorbed onto chemically modified silver films by surface-enhanced spectroscopy,” *Journal of Molecular Structure,* Vols. 563-564, pp. 183-191, 2001.

[120] M. Mbarek, M. Chemek, J. Wery, J. Duvail and K. Alimi, “The effect of conjugation length distribution on the properties of modified PPV,” *Journal of Physics and Chemistry of Solids,* vol. 75, pp. 752-758, 2014.

[121] E. D. Schmid and R. D. Topsom, “Raman intensity and conjugation. 5. A quantitative relationship between Raman intensity and the length of conjugation and an analysis of the Raman intensities of some substituted benzenes and biphenyls,” Journal of the American Chemical Society, Australia, 1981.

[122] L. Tian, N. Gandra and S. Singamaneni, “Monitoring Controlled Release of Payload from Gold Nanocages Using Surface Enhanced Raman Scattering,” *ACS Nano,* p. p6, 2013.

[123] K. Kim, Z. Lee, W. Regan, C. Kisielowski, M. F. Crommie and A. Zettl, “Grain Boundary Mapping in Polycrystalline Graphene,” ACS Nano, USA, 2011.

[124] X. Zhuang, T. Ha, H. D. Kim, T. Centner, S. Labeit and S. Chu, “Fluorescence quenching: A tool for single-molecule protein-folding study,” *PNAS Organization,* Vols. 97, no. 26, p. 14241–14244, 2000.